POLITECNICO DI MILANO

DIPARTIMENTO DI ELETTRONICA, INFORMAZIONE E BIOINGEGNERIA (DEIB)

DOCTORAL PROGRAMME IN BIOENGINEERING

MODEL-BASED ANALYSIS OF DIFFUSION MAGNETIC RESONANCE:

STUDY OF MICROSTRUCTURAL DAMAGE

IN WHITE MATTER AND GRAY MATTER DISEASES

Doctoral Dissertation of:

Matteo Figini

Supervisors:

Prof. Giuseppe Baselli, Dr. Alberto Bizzi

Prof. Daniel Alexander, Dr. Hui Zhang

Tutor:

Prof. Alberto Redaelli

The Chair of the Doctoral Programme:

Prof. Maria Gabriella Signorini

2011-2014 – XXVI Cycle

Se davvero si sentono fratelli gli uomini non cantano all'unisono, ma in armonia

Wystan Hugh Auden

Finché si è inquieti, si può stare tranquilli.

Julien Green

Contents

ABSTRACT

Diffusion MRI (dMRI) is a technique for the non-invasive characterization of the microstructural properties of biological tissues. Conventional dMRI methods, such as Diffusion Tensor Imaging (DTI), rely on rather simple hypotheses relevant to hindered anisotropic diffusion homogeneous within each voxel, which limit their sensitivity and specificity.

To overcome these limits, several advanced dMRI techniques have been developed; in particular multi-compartment models disentangle hindered and restricted, isotropic and anisotropic diffusion.

The aim of this work is to investigate the feasibility and the potential benefits of multi-compartment dMRI models in clinical studies on neurological disease involving gray matter (GM) or white matter (WM), with a translational approach.

Three applications were tested: the study of gray matter alterations in Creutzfeldt-Jakob Disease (CJD), the microstructural characterization of brain tumors and the reconstruction of the trajectory of WM tracts (tractography) in patients with peritumoral edema.

In the first case, two possible neuropathological mechanisms were investigated and novel biomarkers for CJD were provided, likely more sensitive and specific to this pathology than usual DTI-derived measures. In the second application, the parameters derived from a multi-compartment model allowed the characterization of different lesion component and the differentiation of tumor grades better than DTI parameters. Finally, the use of a multi-compartment model allowed the robust reconstruction of WM tracts through areas of peritumoral vasogenic edema, which is usually not possible with DTI-based tractography.

In conclusion, the application of dMRI multi-compartment models in clinical research is feasible and can provide more accurate information about brain microstructure than traditional dMRI methods.

SUMMARY

Background

Diffusion MRI (dMRI) is an MRI technique sensitive to the diffusive motions of water molecules. In biological tissues, the presence of structures such as cells, fibers, membranes or macromolecules reduces water mobility by specific directionality and dispersion statistics. Thus dMRI can convey indirect information about tissue microstructure, which has demonstrated good sensitivity to pathological changes in many diseases. A related application of dMRI is tractography, which provides the virtual reconstruction of fiber trajectories, based on the identified local orientations, and also information on fiber integrity.

Conventional dMRI methods such as Diffusion Tensor Imaging (DTI) rely on the hypothesis of free or hindered diffusion, which implies a Gaussian distribution of displacements. This is generally a good approximation at low diffusion weightings (i.e., b-values), but it does not allow a good fitting of the dMRI signal in many cases at higher diffusion weightings. In particular, a deviation from Gaussianity can be caused by diffusion restriction or by the presence of multiple compartments with different diffusion characteristics in the same voxels (for example, crossing fiber bundles or partial volume between different tissues).

To provide a better characterization of diffusion in these cases, many advanced dMRI methods have been proposed. Two main trends in the development of advanced dMRI methods can be identified: a first class of techniques focuses on the orientation of white matter fibers in complex configurations, while a second one focuses on the microstructural characterization of tissues.

In particular, the latter group includes multi-compartment models describing hindered and restricted diffusion in compartments with known geometry. If the studied tissue is accurately modeled, this approach can provide estimations of specific microstructural parameters, such as the volume fraction occupied by each compartment or the size and orientation of the structures restricting water diffusion.

The increased mathematical complexity of the models implies more complex acquisition schemes and processing procedures than usual, so a compromise between complexity and accuracy is needed for the application of these model-based advanced dMRI methods in clinical studies.

The aim of this thesis is to assess the feasibility of model-based dMRI techniques in clinical research, and to investigate their utility in the characterization of microstructural changes caused by gray matter (GM) and white matter (WM) diseases.

Model-based analysis of dMRI signal in CJD patients

In the first application, mathematical models were developed and applied for the study of microstructural changes in Creutzfeldt-Jakob Disease (CJD).

CJD is the most common human type of prion disease, a class of neurodegenerative diseases with a peculiar transmission mechanism involving a misfolded isoform (PrP^{Sc}) of the cellular prion protein. The main neuropathological features of CJD are astrocytosis, neuronal loss, intracellular spongiform degeneration and PrP^{Sc} accumulation in extracellular space. The presence of hyperintense regions (i.e., with reduced diffusion) on dMRI, with asymmetric distribution on the two hemispheres, is a common marker for the diagnosis of CJD, but the origin of this signal abnormality is currently unknown.

In this work, two hypotheses were formulated for the main neuropathological cause of dMRI hyperintensity in CJD: reduced diffusivity due to the accumulation of PrP^{Sc} in the

extracellular space and diffusion restriction in the vacuoles. Two isotropic bi-compartment models of diffusion were developed to test these hypotheses: 1) a biexponential model to describe intra- and extra-cellular hindered diffusion (an exponential signal intensity decay with b corresponds to a hindered compartment); 2) a model with restricted diffusion in a spherical compartment (i.e., vacuoles) and hindered diffusion in the other. If PrP^{Sc} deposition were the main cause of hyperintensity, a decrease of extracellular diffusivity would be expected in CJD patients, while if the main cause were restriction in vacuoles an increase of the volume fraction of the restricted compartment and a better fit of the latter model would be expected.

dMRI data with a wide range of echo times (TE), diffusion weightings (b-values) and diffusion times were acquired from 15 patients with suspected diagnosis of prion disease and in 4 healthy age-matched subjects. 10 of the patients were diagnosed with CJD, 2 with Gerstmann–Sträussler–Scheinker disease, a prion disease without dMRI hyperintensities (GSS group) and 3 with Rapidly Progressive Encephalopathy, sharing similar neurological signs but without the MRI and histologic alterations of CJD (RPE group).

The two proposed models, plus a mono-exponential model considered as a conventional reference, were fitted to the data. Multiple regions of interest (ROIs) were delineated in gray matter; in CJD patients, hyperintense areas on dMRI were classified as "affected" (CJD+ group), while areas without hyperintensity were classified as "apparently unaffected" (CJD- group).

In a first step, the dMRI raw signal was compared between CJD+, CJD- and control regions. As expected, the signal in CJD+ regions was significantly higher than in the other areas with all the combinations of TE and b-values. The finding of maximum contrast at TE = 103 ms and b = 3000 s/mm^2, from this preliminary analysis indicated this as optimal operating point for the detection of CJD by dMRI.

In a subsequent step, the fitting performance of the models was evaluated. Both the bi-compartment models performed significantly better than the mono-exponential model. In the affected areas the advantage of the bi-compartment over the mono-exponential models was higher, even if the fitting performance itself was worse in all the models. Hence, the proposed models were able to better characterize the brain tissue than the traditional one, especially in pathological conditions. However no difference was found between the two bi-compartment models in terms of fitting performance, so it was not possible to draw conclusions about the most likely microstructural alteration responsible for dMRI hyperintensity.

Finally, the parameters estimated by the three models were compared between all the pathological groups (CJD+, CJD-, RPE and GSS) and the healthy controls. The results of the statistical analysis are shown in table 1.

In the CJD+ group, the main results were an increase of T_2 in all the models, a decrease of both the extracellular and intracellular diffusivities and of the mono-exponential ADC, and an increase of the volume fraction of the restricted compartment in the vacuole model. The estimated radius of the spherical compartment with restricted diffusion was compatible with the size of vacuoles estimated by histology studies in literature.

In the CJD- group, an increase of T_2 and of the fraction of the restricted compartment were found, while in the RPE and GSS groups no consistent significant difference was observed. Basing on these results, both the proposed pathological mechanisms can contribute to the observed dMRI hyperintensity, even though a combination of the hypotheses does not fully explain the results; for example in the restricted-diffusion model the diffusivity out of the spherical compartment is not reduced as would be expected if diffusion was hindered by PrP^{Sc} accumulation.

Table 1. Results of the group analysis in the study on CJD.
Mean relative difference in each parameter between each group (CJD+, CJD-, RPE or GSS respectively) and the healthy controls. Not statistically significant differences are marked as "n.s."

		CJD+	CJD-	RPE	GSS
Biexponential	M_0	n.s.	n.s.	n.s.	n.s.
	T_2	+26%	+10%	n.s.	n.s.
	d_F	-14%	n.s.	n.s.	n.s.
	d_S	-37%	n.s.	-20%	n.s.
	f	+4%	n.s.	+9%	n.s.
Restricted	M_0	n.s.	n.s.	n.s.	n.s.
	T_2	+18%	+8%	n.s.	n.s.
	d_H	n.s.	+8%	+10%	n.s.
	f	+46%	+19%	n.s.	n.s.
Monoexp	M_0	-8%	n.s.	n.s.	n.s.
	T_2	+31%	+12%	+5%	n.s.
	ADC	-20%	n.s.	+5%	n.s.

In conclusion, this study may represent an important step towards the characterization of microstructural changes in CJD. Even though the precise pathological mechanism responsible for dMRI hyperintensity could not be definitely determined, this study provided tools to design an optimized dMRI acquisition protocol and new promising biomarkers for sensitive and specific CJD diagnosis. In particular, the estimation of vacuole size could be used to non-invasively discriminate CJD subtypes, which have quite different prognosis.

Microstructural features of brain tumors by NODDI

In the second application, dMRI data from patients with brain gliomas were analyzed with NODDI (Neurite Orientation Dispersion and Density Imaging). The characterization and staging of brain tumors is very important to plan surgery and/or radio- and chemo-therapy. In particular, the malignancy scale defined by the World Health Organization (WHO) associates each lesion with a tumor grade between I and IV and is widely applied. It is based on neuropathological features and an early non-invasive proxy by neuroimaging would be useful.

Many studies investigated the possibility of tumor grading by DTI, with contradictory results, probably due to the low specificity of DTI-based parameters. Multi-compartment models are expected to provide more specific microstructural information; in this study NODDI was chosen for this purpose because its relatively low complexity makes it feasible in a clinical setting.

NODDI is a three-compartment model describing diffusion in the intracellular compartment as restricted in a set of sticks with orientations distributed around the principal direction, diffusion in the extracellular compartment as hindered (modeled by a diffusion tensor) and diffusion in the Cerebro-Spinal Fluid (CSF) compartment as free and isotropic. Although restriction geometry was proposed to describe fibers in the WM, NODDI parameterization of stick directional dispersion allows applications in tumoral tissue where directionality is virtually lost.

dMRI data from 71 patients with brain gliomas were acquired with a two-shell protocol (b = 700 and b = 2000 s/mm^2) and both NODDI and DTI parameters were estimated.

In a subset of 20 patients, an additional three-compartment model describing isotropic restricted, hindered and free diffusion was fitted for comparison to the intrinsically anisotropic modeling of restriction by NODDI. The results of this preliminary analysis

showed a good performance of NODDI and a very good correlation between the intracellular volume fraction estimated by NODDI (f_{ICV}) and the fraction of restricted diffusion estimated by the isotropic model. Even though NODDI tends to overestimate the restricted fraction, this result validated f_{ICV} as a relative index of restricted diffusion even in isotropic conditions.

The comparison between tumors of different grades showed different patterns of NODDI parameters. Specifically, grade II lesions displayed high volume fractions of the extracellular compartment (f_{ECV}), interpreted as high extracellular water content as expected in low grade gliomas. In grade III gliomas regions with an increased fraction of the intracellular compartment (f_{ICV}), interpreted as high cellularity, were detected in addition to those with high extracellular water content. Grade IV gliomas were usually heterogeneous: they included presumably necrotic areas with a high fraction of CSF (f_{ISO}), areas of enhancement with increased f_{ECV} and f_{ISO}, highly cellular areas, and peritumoral edemas.

These results, though requiring a neuropathological validation (not available), are compatible with known features of the different grades, and thus candidate NODDI as a promising tool for tumor characterization. By contrast DTI parameters, namely FA, were not specific to the different features of the various studied lesions.

Statistical contrasts between lesions grouped by their grade were performed considering maximal values within ROI of f_{ICV} and f_{ISO} and mean f_{ECV}. All the three NODDI volume fractions allowed a statistically significant discrimination between grade IV and both grade II and grade III lesions (figure 1), since a higher maximum f_{ICV} and f_{ISO} and a lower mean f_{ECV} was evident in grade IV gliomas.
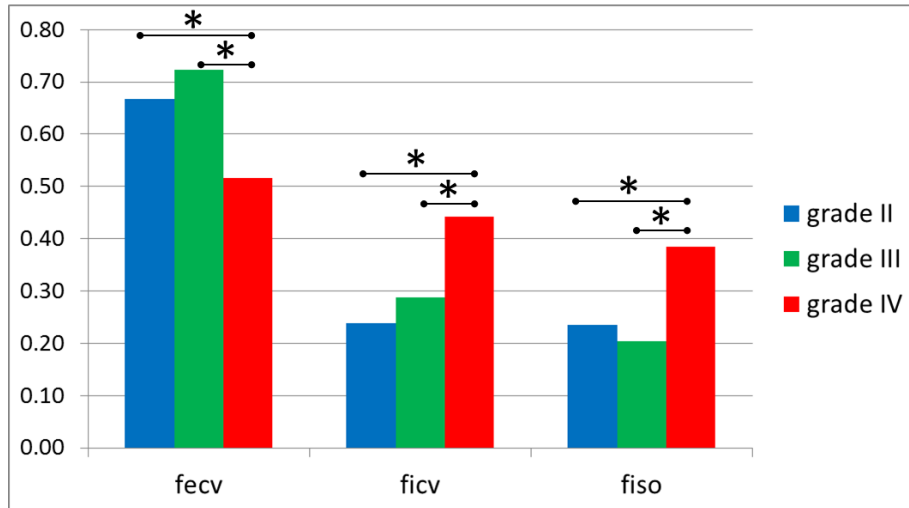
Figure 1. Bar graph showing the mean f_{ECV}, maximum f_{ICV} and maximum f_{ISO} averaged among the patients with grade II, grade III and grade IV gliomas, respectively. The significant differences are marked with stars.

In conclusion, these preliminary results show that non-invasive tumor characterization and grading by NODDI is feasible in a clinical context. If validated by a more extensive and localized correlation with neuropathological measures, they can have an important impact on the preoperative evaluation of brain tumors, and on neuro-oncology therapy in general.

NODDI-based tractography in peritumoral edema

In a last application, an algorithm for tractography based on NODDI parameters (NODDIT) was developed and applied in patients with glioblastoma multiforme (GBM) to test the possibility of a better reconstruction through areas of vasogenic edema than allowed by DTI-based tractography (DTT).

In presurgical neuro-oncological mapping, it is important to define the boundaries of the lesion and to understand if the surrounding tissue contains functional areas and/or

14

undamaged WM bundles, in order to resect all the affected tissue (if possible) and at the same time minimize the neurological deficits induced by the surgical operation.

For this purpose, functional MRI and tractography are now commonly applied together with intraoperative electrical stimulation. However DTT, which is the most widely applied technique for tractography, has some limitations; in particular, it usually does not allow the reconstruction of WM tracts through areas of peritumoral vasogenic edema, where intact fibers are known to be present. This is mainly due to the termination criteria commonly used in tractography, which is based on an FA threshold to exclude regions where the estimation of the principal diffusion direction is unreliable; unfortunately this criterion excludes also regions with partial volume between WM structures and extracellular water, as in the case of edema. The use of parameters derived from a multi-compartment model for tractography is expected to allow more specific termination criteria to exclude only regions with high fiber orientation dispersion, and not those with partial volume from extracellular water but coherently oriented fibers. Considering NODDI, the orientation dispersion index (ODI) is a specific index of fiber orientation dispersion, assumed that a sufficient amount of brain tissue is present in the voxel. Thus, in the proposed NODDIT algorithm the termination criterion was based on two thresholds: an upper threshold on ODI to track only through regions with coherently oriented fibers, and an upper threshold on f_{ISO} to assure that the brain tissue content is sufficient for a reliable estimation of ODI.

In this study, dMRI data from 10 patients with GBM surrounded by vasogenic edema were selected from the database considered in the previous section. Also, 10 patients with tumors far from the main WM tracts and an hemisphere free from apparent lesions were selected to provide control hemisphere and control bilateral tracts.

In a preliminary phase, the termination criteria for NODDIT were optimized to allow a fair comparison with DTT. Specifically, in the control hemispheres, tractography reconstructions were performed by DTT with the well-established FA upper threshold of

0.2 and by NODDIT with several ODI thresholds, fixing an f_{ISO} upper threshold of 0.8. The voxel-by-voxel correlation of the number of streamlines obtained and the overlap between the volume of specific tracts reconstructed by the two methods were evaluated. An optimal ODI threshold of 0.49 was finally selected, allowing the most similar results to DTT in the healthy regions.

Hence, this NODDIT setting was applied to the 10 GBM patients. The mean streamline density obtained by NODDIT and DTT was evaluated in 3 ROIs per patient: the tumor core, the peritumoral edema and the contralateral WM.
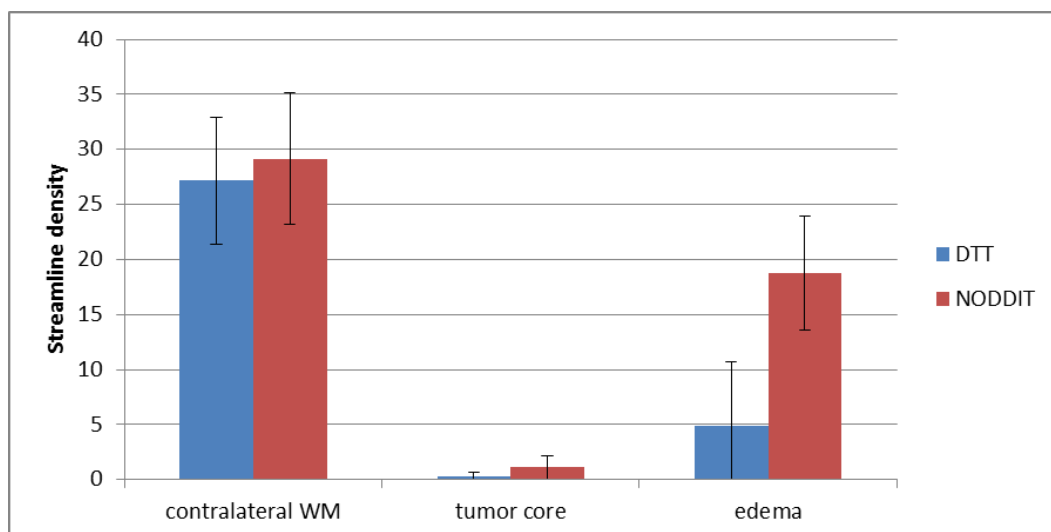
Figure 2. Mean streamline density found by DTT and NODDIT in contralateral healthy WM, tumor core and vasogenic edema.

The results are shown in figure 2. In contralateral normally appearing WM the streamline densities provided by NODDI and DTT were similar, as expected since the calibration step. In the tumor core, where little structure should be present, very low streamline densities were found by both the methods as expected. By contrast, in areas of edema NODDIT provided significantly higher streamline densities, about two thirds of the values found in the contralateral WM.

The robustness of this finding was confirmed by evaluating its low sensitivity to the fixed ODI threshold. Conversely, the dependence on the FA threshold was also investigated,

showing that rising DTT sensitivity by lowering FA threshold to about 0.1 can provide similar results to NODDIT in the edemas; however, an unacceptable specificity loss was highlighted, with a high number false positives, as verified even in the ventricles.

The visual inspection of the tractographic reconstruction of specific tracts further confirmed the outperformance of NODDIT versus DTT: in all the considered cases NODDIT showed more streamlines passing through the edemas, or even allowed reconstructing tracts completely missed by DTT (figure 3).
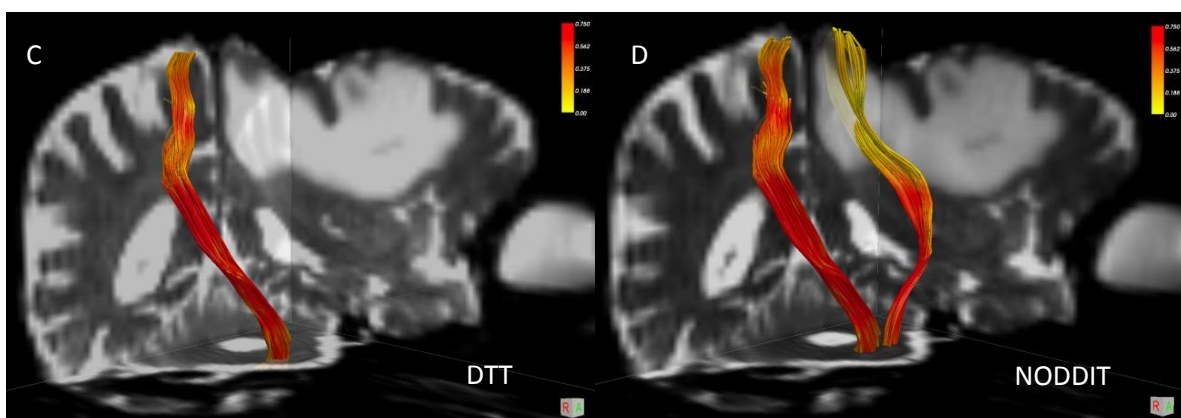
Figure 3. Example of tractographic reconstruction in a representative GBM patient.
The cortico-spinal tract was reconstructed from the same ROIs with DTT (A) and NODDIT (B). DTT did not allow the reconstruction of any streamline on the side of the edema, while NODDIT provided a realistic reconstruction of the CST. The streamlines are color-encoded according to FA.

In conclusion, this preliminary study on NODDI-based tractography in brain tumor patients showed the feasibility of the proposed approach in a clinical setting and its superiority to DTT in the robust reconstruction of tracts passing through regions of vasogenic edema.

NODDIT could find important applications in the preoperative mapping of patients with brain gliomas.

Conclusions

In all the proposed applications, the use of multi-compartment models was clinically feasible and advantageous when compared to traditional methods. Even though these preliminary studies have to be confirmed on larger samples and carefully validated, the parameters provided by the multi-compartment models seem more specific to the underlying tissue microstructure and its pathological changes.

The use of advanced dMRI methods involves a non-trivial work for the choice of suitable models, with a complexity chosen as a trade-off between the desired amount of information on the studied tissue and the feasibility of needed acquisition and fitting procedures. Furthermore, the biological or medical interpretation of the results, even though apparently obvious from the definition of the model, can be challenging in some situations.

Nonetheless, the promising results presented here in different clinical research studies demonstrate the advantage of this kind of analysis for the microstructural characterization of the changes induced by neurological diseases in GM and WM.

1. INTRODUCTION

*Nothing has such power to broaden the mind
as the ability to investigate systematically and truly
all that comes under thy observation in life.*

Marcus Aurelius

This PhD thesis addresses the study of microstructural properties (i.e. features below voxel-size, even though averaged in the voxel volume) by means of diffusion MRI (dMRI) in clinical studies of both gray matter (GM) and white matter (WM) of the human brain. A brief review of physical principles, models and methods is presented in this chapter, aiming at a critical evaluation of the necessary compromises between precision and feasibility in the clinical environment. Some of the advanced methods presented here will be applied in chapters 2-4 to the analysis of microstructural changes induced by GM and WM pathologies.

Information from dMRI is basically drawn by studying MRI signal attenuation with acquisition parameters sensitizing it to water diffusion. A major distinction is between isotropic (e.g. GM, at least approximately) and anisotropic (e.g., WM) conditions, where the latter is due to fiber orientation and requires the exploration of numerous directions. A second distinction involves homogeneity with diffusion length, which leads to Gaussian distribution of diffusion dispersion, as in the basic diffusion tensor imaging (DTI), largely applied so far. Deviation from this hypothesis provides more information about diffusion, which can be modeled as hindered or restricted in multiple microstructural compartments within the same voxel.

This more detailed exploration requires data with different enhancements of diffusion (i.e., various b-shells, see below) and adequate modeling of dMRI attenuation.

1.1. Diffusion MRI

Brownian motion is the apparently random motion of molecules caused by their internal kinetic energy and by their interactions (figure 1.1), first described by Robert Brown [Brown 1828]. These motions happen in any fluid due to thermal agitation, without need of external driving forces.
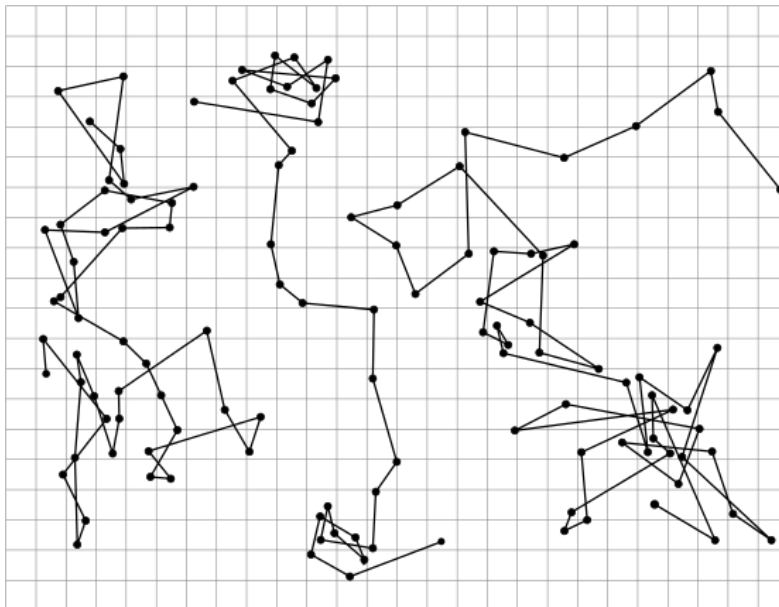
Figure 1.1. Examples of brownian motion. Three tracings of the motion of colloidal particles of radius 0.53 μm, as seen under the microscope, are displayed. Successive positions every 30 seconds are joined by straight line segments (the mesh size is 3.2 μm) Reproduced from the book of Jean Baptiste Perrin, Les Atomes,

Diffusion is defined upon the macroscopical effect of Brownian motion by the diffusion coefficient D [$L^2 T^{-1}$] providing the ratio between a volumetric concentration gradient [$M L^{-4}$] divided by diffusion flux [$M L^{-2} T^{-1}$].

According to Einstein [Einstein 1905], considering the statistical distribution of the motions of a population of freely diffusing molecules, the displacements from their initial positions

after a diffusion time T_{diff} follow a Gaussian distribution with null mean and the following variance:

$$\langle (r_1 - r_0)^2 \rangle = 2nDT_{diff} \tag{1.1}$$

where D is the diffusion coefficient and n is the number of dimensions of the problem (n = 1 when considering the projections of displacements along a line, n = 2 in a plane and n = 3 in the space). Figure 1.2 illustrates the evolution of the displacements distribution with the diffusion time.
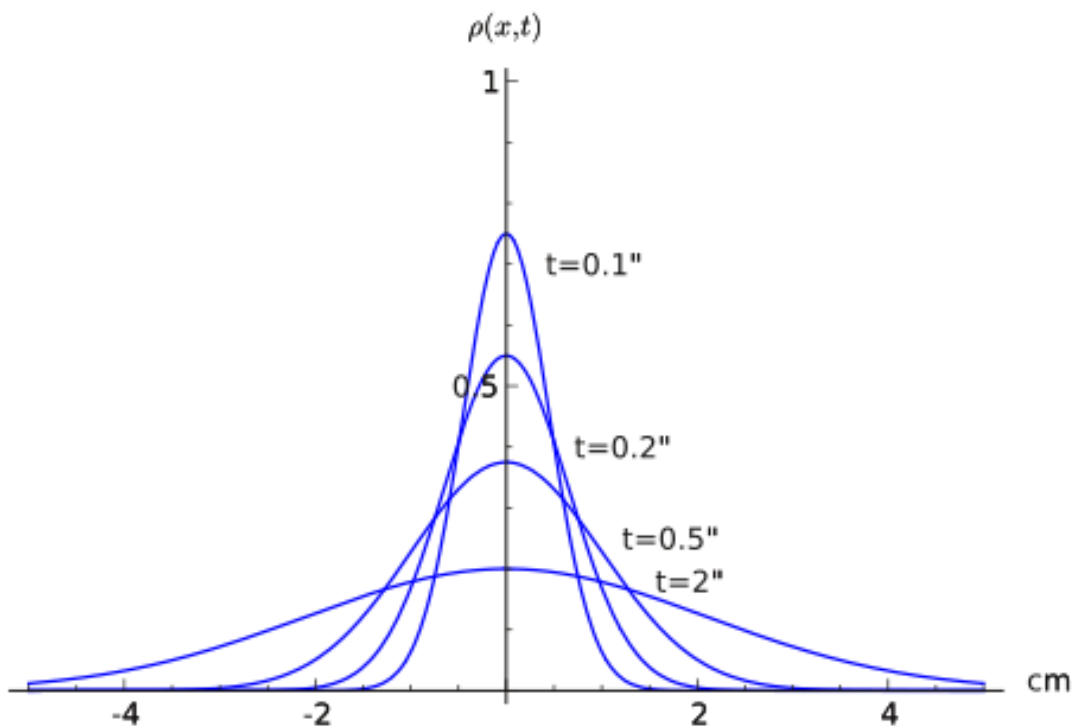
Figure 1.2. Characteristic displacement distributions for free diffusion with increasing diffusion times (t). Reproduced from "Bernard H. Lavenda - Nonequilibrium Statistical Thermodyamics - John Wiley & Sons Inc"

According to the Bloch-Torrey equations, diffusion in the presence of gradients does always blur spin phase coherence, thus attenuating the signal and limiting MRI resolution. This effect, though normally negligible at clinical resolution scales, can be greatly enhanced by Diffusion Magnetic Resonance Imaging (dMRI), which is an MRI technique specifically sensitive to diffusive motions of molecules in fluids [Le Bihan 1988, Mori 1999].

The addition of gradient pulses (diffusion-sensitizing gradient pulses, [Stejskal 1965]) to an imaging sequence causes a position dependent dephasing/rephasing of spins, and hence a signal loss dependent on the displacement of molecules along the spatial direction of the diffusion gradients in the time interval between the pulses (figure 1.3).
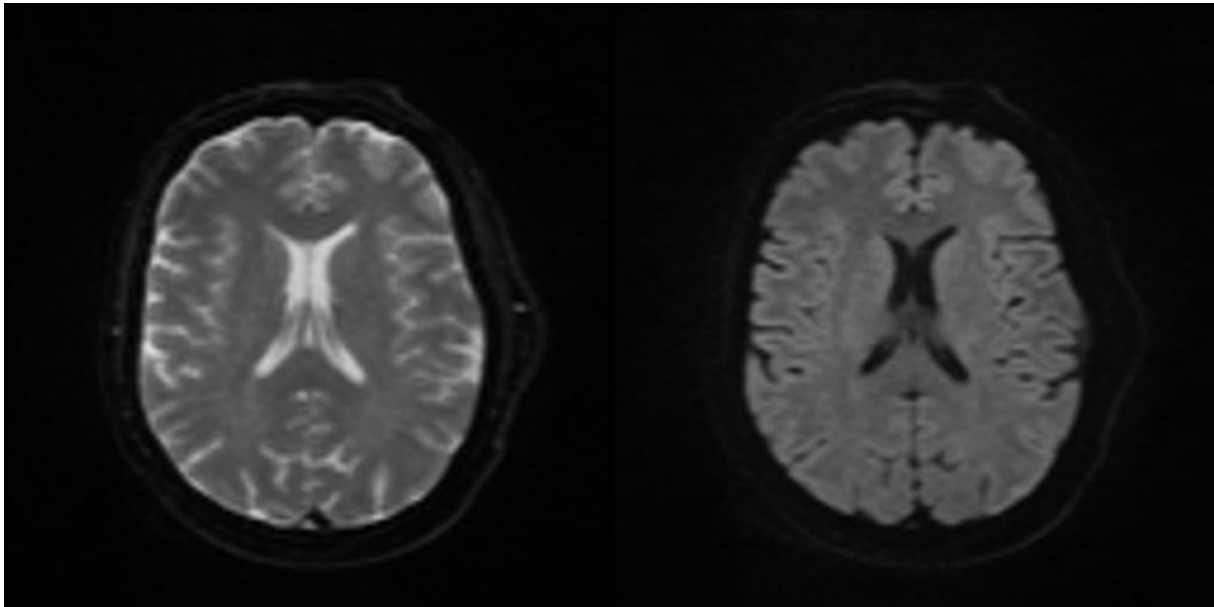
Figure 1.3. Examples of MRI images without (left) and with (right) diffusion weighting

In almost all the cases the target molecule of dMRI, as of MRI in general, is water, the most common ^{1}H compound, in biological tissues. So in the great majority of applications dMRI is sensitive to the displacements of water molecules in biological tissues.

Equation (1.1) is valid only in the case of free diffusion i.e. diffusion in an infinite space without barriers. In this condition, the distribution of displacements depends only on T_{diff}, on temperature and on the characteristics of the molecule. Since the molecule is usually water, the temperature is usually that of human body (36-37 °C) and T_{diff} depends on the acquisition sequence, dMRI would not be very informative, in this case. The reason why dMRI founds wide application in clinics and in biomedical research is that diffusion is seldom free in biological tissues, even in the short scale of tens of µm, which is the order of magnitude of displacements in a typical dMRI experiment. Many obstacles as cells, macromolecules, membranes and fibers slow down diffusive motions (hindered diffusion,

figure 1.4, left) or even prevent them along some directions (restricted diffusion, figure 1.4, right).
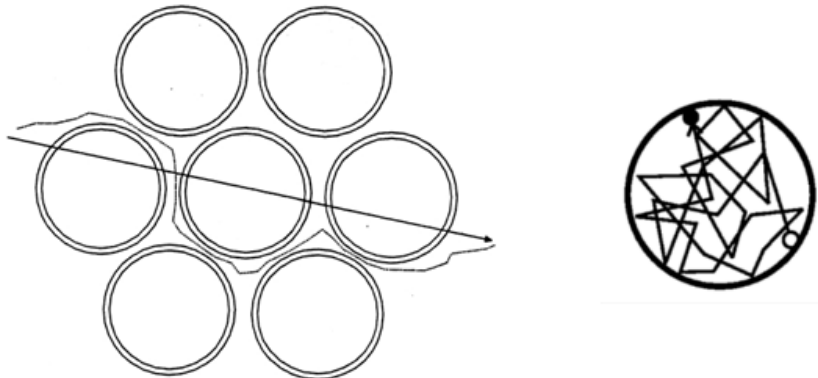
Figure 1.4. Schematic representation of hindered (left) and restricted (right) diffusion. Reproduced from [Price 1996]

Therefore equation (1.1) is not directly valid in most cases and it has to be corrected according to the effect of biological structures on water diffusion, as will be explained in the next paragraphs. The simplest way of accounting for the effect of obstacles on diffusion is to consider equation (1.1) as still valid, but with a reduced diffusion coefficient (the so-called Apparent Diffusion Coefficient, ADC). This approach can be extended to non-isotropic tissues describing the orientation dependence of the ADC by the so-called Diffusion Tensor. In these two cases the displacement distribution is still Gaussian, but conditions such as restriction may lead to non-Gaussian distributions, described by advanced models such those considered in this thesis work.

In conclusion, the parameters estimated by dMRI methods depend mainly on the microstructure of the examined tissue, and may be very useful for its characterization. Proper modeling of both hindered and restricted diffusion can provide further information compared to the basic Gaussian description of hindered diffusion.

1.2. Apparent diffusion Coefficient and Diffusion Tensor Imaging: hindered diffusion

As already mentioned, the simplest way to extract information from dMRI is to consider equation (1.1) as valid even though diffusion is not free. Indeed, in most cases the main effect of obstacles to diffusive motions is to reduce the extent of displacements, but their statistical distribution can be still considered approximately Gaussian; this condition is defined as hindered diffusion.

With the hypothesis of hindered diffusion, it can be demonstrated [Stejskal 1965] that the ratio between the signal of a diffusion-weighted image and that of an equivalent image without diffusion weighting is:

$$E = \frac{S(b)}{S(0)} = e^{-b \cdot ADC} \tag{1.2}$$

where ADC is the Apparent Diffusion Coefficient in the considered voxel, and b is the so-called b-value, which reflects the amount of diffusion weighting and depends on the acquisition parameters according to the following formula in the case of rectangular diffusion gradient pulses:

$$b = \gamma^2 g^2 \delta^2 \left(\Delta - \frac{\delta}{3} \right) \tag{1.3}$$

where γ is the gyromagnetic ratio of the ^{1}H atom ($267.51 \cdot 10^{-6}$ rad$\cdot$s$^{-1}\cdot$T^{-1}), g is the intensity of the gradient pulses, δ is their duration and Δ is the time interval between them. In clinical routine, b-values of about 1000 s/mm^2 are usually applied.

Then the ADC can be estimated as follows:

$$ADC = -\frac{1}{b} ln \frac{S(b)}{S(0)} \tag{1.4}$$

The ADC is an indirect index of microstructure, as it reflects the presence of obstacles to water diffusive motions in the direction of the diffusion gradient, averaged over the

considered voxel. For example, it has found application in the early detection of ischemic stroke, associated with a low ADC in the acute phase.

In some cases the biological tissues contain ordered structures aligned along the same direction, for example axons in cerebral and spinal white matter or muscle fibers. In these tissues the estimated ADC depends strongly on the gradient direction: for example water molecules can diffuse much more freely along the direction of fibers than orthogonally.
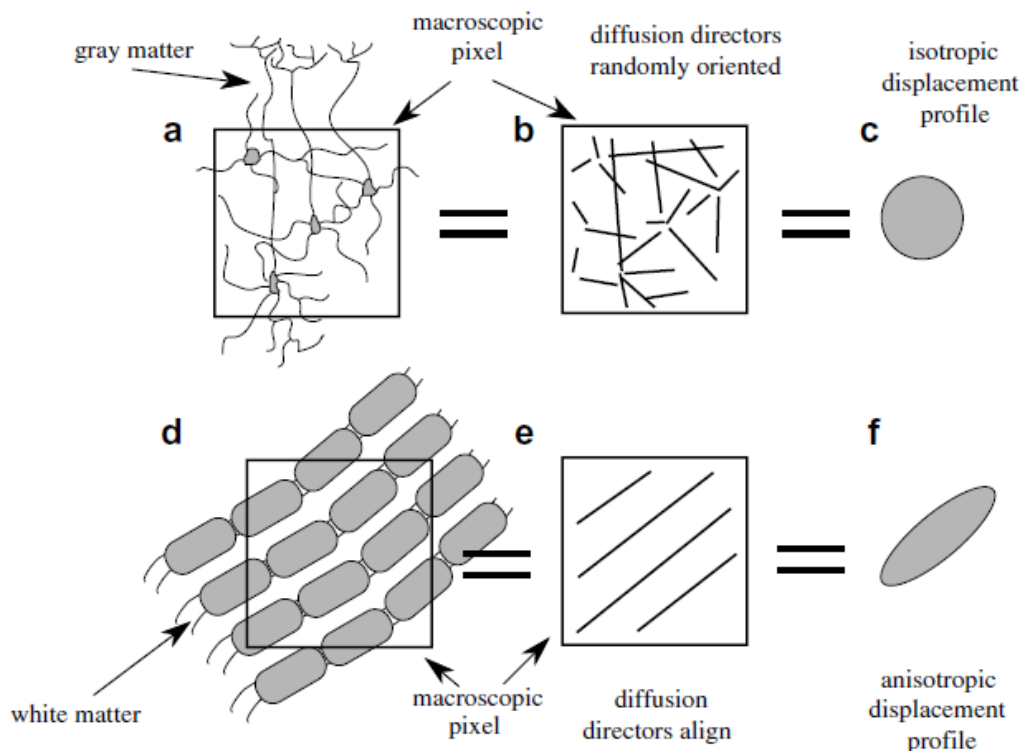
Figure 1.5. The origin of differences in diffusion anisotropy between gray matter (top) and white matter (bottom). In a and d a pictorial representation of microstructure is shown, in b and e the corresponding diffusion directions are schematically represented, and in c and f characteristic displacement profiles are displayed. Reproduced from [Komlosh 2006]

In order to characterize such angular dependence of diffusion, the diffusion tensor was introduced [Basser 1994]. The diffusion tensor is defined as:

$$\boldsymbol{D} = \begin{bmatrix} D_{xx} & D_{xy} & D_{xz} \\ D_{yx} & D_{yy} & D_{yz} \\ D_{zx} & D_{zy} & D_{zz} \end{bmatrix} \tag{1.5}$$

where D_{ab} is the correlation between diffusion along direction a and diffusion along direction a; with a = b (diagonal elements), D_{aa} is the ADC along direction a.

Equation (1.2) can be generalized to the anisotropic case:

$$E = exp(-b\boldsymbol{g}^T\boldsymbol{D}\boldsymbol{g}) =$$

$$= exp\left[-b\left(g_x{}^2D_{xx} + g_y{}^2D_{yy} + g_z{}^2D_{zz} + 2g_xg_yD_{xy} + 2g_xg_zD_{xz} + 2g_yg_zD_{yz}\right)\right]$$

(1.6)

where $\boldsymbol{g} = [g_x\ g_y\ g_z]^T$ is a column vector defining the direction of the diffusion gradient pulses.

Thus, the diffusion tensor can be estimated from images with diffusion weighting along at least 6 independent directions (Diffusion Tensor Imaging, DTI) plus a reference b_0 image with b = 0 or very low. However, redundancy by about 30 directions is recommended and currently applied [Jones 2004].

The diffusion tensor can be diagonalized to find its eigenvectors (v_1, v_2 and v_3) and eigenvalues (λ_1, λ_2 and λ_3), representing the principal directions of diffusion and the associated ADCs, respectively. In particular, the first eigenvector is the direction of maximum diffusion, which in the case of fibrous systems can be considered as corresponding to the direction of the fibers.

The diffusion tensor can also be represented as an ellipsoid (the so-called diffusion ellipsoid, figure 1.6), having the eigenvectors as axes.
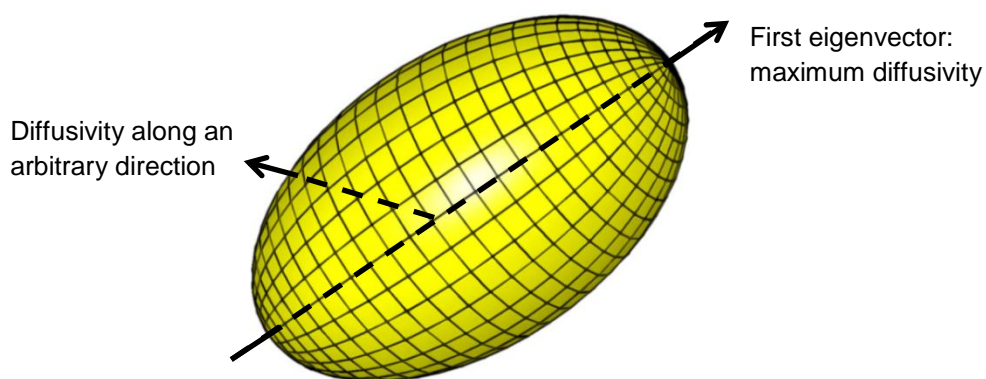
Figure 1.6. The diffusion ellipsoid and its interpretation: the main axis of the ellipsoid is the first eigenvector, its size in any direction represents the apparent diffusivity estimated in that direction

It is an intuitive representation, because the size of the ellipsoid is proportional to the ADC in any direction (according to the hypothesis of the diffusion tensor model, which is only a first order approximation of the real diffusion patterns [King 2001]).

Several parameters can be derived from the diffusion tensor [Basser 1996]; the most widely used are the Mean Diffusivity (MD):

$$MD = \frac{\lambda_1 + \lambda_2 + \lambda_3}{3} \tag{1.7}$$

and the Fractional Anisotropy (FA):

$$FA = \sqrt{\frac{3}{2} \frac{(\lambda_1 - MD)^2 + (\lambda_2 - MD)^2 + (\lambda_3 - MD)^2}{\lambda_1^2 + \lambda_2^2 + \lambda_3^2}} \tag{1.8}$$

MD has the dimension of a diffusion coefficient (mm^2/s) and represents the mean mobility of water molecules in the studied tissue, averaged over all the directions. It is a more meaningful parameter than the ADC measured in an arbitrary direction when the environment is anisotropic.

FA represents the degree of anisotropy (i.e. how greater is diffusivity in the main direction than in the others) and is a dimensionless parameter ranging from 0 (perfect isotropy) to 1 (perfect anisotropy).

Figure 1.7 illustrates the meaning of these parameters.

High MD   Low MD   High FA   Low FA
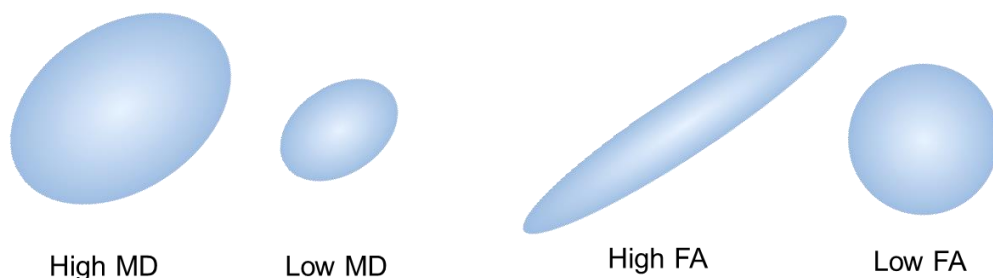
Figure 1.7. Representation of the meaning of MD and FA in terms of the size and shape of the diffusion ellipsoid

Other DTI parameters, commonly used in the study of WM, are the longitudinal (or axial) diffusivity $\lambda_{\parallel} = \lambda_1$, and the radial (or transverse) diffusivity $\lambda_{\perp} = \frac{\lambda_2 + \lambda_3}{2}$. They correspond to the apparent diffusivity along the axis of the tensor and in any direction of the transverse plane, with the hypothesis of cylindrical symmetry, which is a good approximation in the case of WM.

DTI is widely used in clinical practice and in preclinical and clinical research, because it has shown great sensitivity to many pathological conditions associated with microstructural alterations, such as amyotrophic lateral sclerosis [Filippi 2001], epilepsy [Thivard 2005], ischemic lesions [Sotak 2002] and brain tumors [Clark 2003, Schonberg 2006].

1.3. The limits of DTI and the advanced methods

DTI is the most common dMRI technique, and almost the only one used in a clinical context because of the demonstrated sensitivity to microstructural changes and of its requirements in terms of acquisition sequences and post-processing algorithms, relatively easy to comply with.

Nonetheless, it has some limitations, mainly associated with the simple underlying model. The main limit of DTI is that it characterizes all the structures in a voxel with a single three-variate (i.e. the 3 space directions) Gaussian distribution. Thus, if the voxel contains different kinds of structures or groups of structures of the same kind but with different microstructural or orientation characteristics, the diffusion tensor is a representation of the "average" diffusion properties in the voxel and fails to represent the actual microstructure.

A classic example is the so-called "crossing fibers" problem: when two or more White Matter (WM) bundles cross in a voxel, the estimated diffusion tensor is much more isotropic than it would be if only one of the bundles were was present, and its first

eigenvector is in a direction between those of the bundles. So in this case the information derived by DTI (principal direction, FA, MD, etc.) does not represent the actual microstructural characteristics of the tissue and could be even misleading, e.g. indicating pathological structural damage (FA decrease) in place of a physiologically complex structure. Since a relevant percentage of the voxels in WM contain more than one fiber bundle, this is not a negligible problem (different estimates of this percentage have been reported, ranging from 33% [Behrens 2007] to 63% and 90% [Jeurissen 2013]). The same issue arises with more complex configurations in which more than one fiber direction is present, for example with fibers fanning or "kissing" and even more in the so called meso-scale of fiber endings impinging on corical sulci and gyri [Catani 2012].

Partial volume effects at tissue boundaries (e.g., GM/WM, WM/CSF) do limit both DTI and more complex models, since the presence of different kinds of tissues in the same voxel makes estimates depend on a mixture of their properties. Conversely, multi-compartment models can better deal with voxels in regions containing mixed structures An important case of partial volume severely affecting DTI is vasogenic edema, the accumulation of water in the parenchymal extracellular space due to a breakdown of the blood-brain barrier, which may result from trauma, tumors, inflammation or other causes. In areas of vasogenic edema high MD and low FA values are found, but the microstructure of the tissue is not usually altered apart the increase of water in the extracellular space; in particular, the WM bundles are often preserved, so the decreased FA derives from a partial volume effect with extracellular water rather than from a loss of WM integrity. Furthermore, when water molecules are confined in structures with impermeable barriers (restricted diffusion), the displacement distribution deviates from Gaussianity and DTI may provide a poor characterization of diffusion features.

Since these problems come from the assumption of the diffusion tensor model, a general model-free method could seem the best candidate to overcome DTI limits. Such a method

is called q-space imaging (QSI, [Callaghan 1990, Cory 1990, Price 1996]) and is based on the Fourier relation between the displacement probability distribution of the diffusing molecules (also known as the spin propagator) and the signal attenuation with the parameter $q = \gamma \delta g$; this relation is valid in the hypothesis of short gradient pulses (SGP). With an adequate sampling of the so-called q-space (usually obtained by increments of g with fixed δ), the complete statistical distribution of diffusive displacements can be estimated for a given direction and diffusion time (figure 1.8).
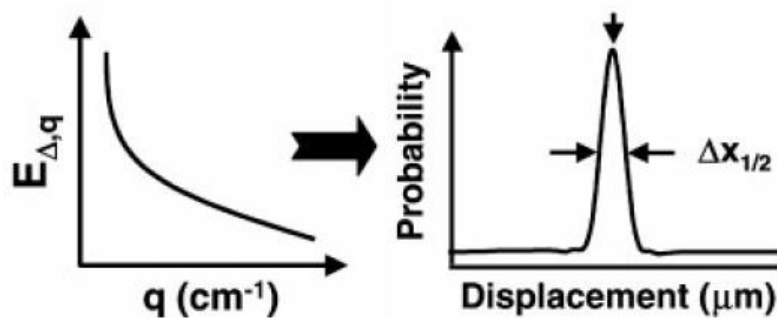
Figure 1.8. Procedure for QSI: the Fourier Transform of the signal decay with q is the probability distribution of displacements. The probability of null displacement and the full-width at half maximum $\Delta x_{1/2}$ (indicated by arrows) are usually evaluated. Reproduced from [Assaf 2000]

The main drawback of QSI is the need of high-performing gradients and very long acquisition times for a good resolution of the displacement distribution. Therefore, QSI is not feasible in clinical practice and its application in research studies is usually limited to the investigation of structures with a well-known and coherent direction, such as the spinal cord and the corpus callosum.

Other advanced dMRI methods find wider application, but are necessarily based on a-priori hypotheses or on mathematical models (obviously more complex than the diffusion tensor). These assumptions allow more reliable and specific results, but limit the application of each technique only to a set of conditions or to some aspects of diffusion.

In particular, two classes of advanced methods can be identified, basing on their aim: the first class focuses on the estimation of the orientation of structures, while the second one

focuses on the microstructural characterization of tissues. A selection of dMRI methods belonging to these two classes will be described in the next two paragraphs.

1.4. Advanced methods focused on the estimation of fiber directions

This class of dMRI methods was developed to estimate the distribution of the directions of fibers in a voxel (the so-called Orientation Distribution Function, ODF) in a more reliable way than allowed by DTI. Since the main aim of these techniques is to identify the direction of the structures in each voxel, some assumptions and simplifications on the other features of the diffusion process are made.

They usually require the acquisition of diffusion-weighted images along a large number of directions with a single b-value (the so-called High Angular Resolution Diffusion Imaging, HARDI), except for Diffusion Spectrum Imaging, as will be explained below.

The main application of these methods is the reconstruction of the trajectory of WM bundles (tractography, paragraph 1.6) and the analysis of structural connectivity between brain areas, with more details, mainly attaining to fiber-crossing.

1.4.1. Multi-tensor

The simplest extension of DTI is the assumption that the signal comes from multiple fiber bundles, each characterized by a Diffusion Tensor [Tuch 2002]:

$$E = \sum_{i=1}^{N} f_i exp(-b\boldsymbol{g}^T \boldsymbol{D}_i \boldsymbol{g}) \tag{1.9}$$

where $\boldsymbol{D}_i$ is the i-th diffusion tensor and f_i the fraction of the signal it explains.

In other words, this method assumes that the distribution of displacements in each fiber bundle is 3D-Gaussian and can be described by linearly combined Diffusion Tensors.

Often, constraints on the axially symmetric shape of the tensor and/or on its anisotropy are applied in order to reduce the complexity of the model and improve the stability of the method [Tuch 2002, Behrens 2007, Hosey 2008]. Sometimes, an additional isotropic compartment is introduced to account for partial volume from CSF or GM [Behrens 2007, Hosey 2005, Hosey 2008].

An issue of the Multi-tensor model is the choice of the number of tensors used to characterize the signal in each voxel. It can be fixed a priori, usually to a number between 2 and 4, based on the knowledge of the average number of bundles crossing in a typical voxel and on the desired orientation detail. Alternatively, the signal in each voxel can be analyzed with multiple models having different numbers of tensors, and the optimal number can be found by comparing their fitting performance [Behrens 2007].

1.4.2. DSI and QBI

Diffusion Spectrum Imaging (DSI, [Wedeen 1999]) is a technique for the identification of fiber directions based on 3D QSI. It requires acquiring data on a 3D Cartesian grid in q-space and next performing a 3D Fourier transform to obtain a 3D spin propagator. The ODF is derived as the radial projection of the spin propagator and the fiber directions are identified as the relative maxima of the ODF.

The main limitation of DSI is the large amount of data required, which corresponds to very long acquisition times. Some variations and extension of DSI have been proposed to reduce the amount of data needed for the estimation of the ODF, but the application of DSI in clinical research is still limited.

A similar approach, with the advantage of greater feasibility in a clinical setting, is Q-Ball Imaging (QBI, [Tuch 2004]). It is based on the principle that an approximation of the ODF can be provided by the Funk transform of the dMRI signal, which is the integral over a large circle in q-space. Thus, the QBI technique can be applied to data acquired with a

HARDI scheme, with a significant reduction of the acquisition time with respect to the complete 3D sampling of the q-space required by DSI. However, the approximation inherent in QBI is theoretically valid only with very large q-values; using high q-values reduces the SNR or requires long acquisition times, so data for QBI are usually acquired with intermediate q-values, even though this introduces blurring into the estimated ODF.

1.4.3. Spherical Deconvolution

This approach is based on the assumption that the dMRI signal in each voxel is the convolution of the fiber ODF on a sphere and a kernel representing the "single fiber response", i.e. the signal one would have if perfectly aligned fibers were present. The ODF can thus be estimated as the spherical deconvolution (SD) of the signal with this kernel [Tournier 2004].
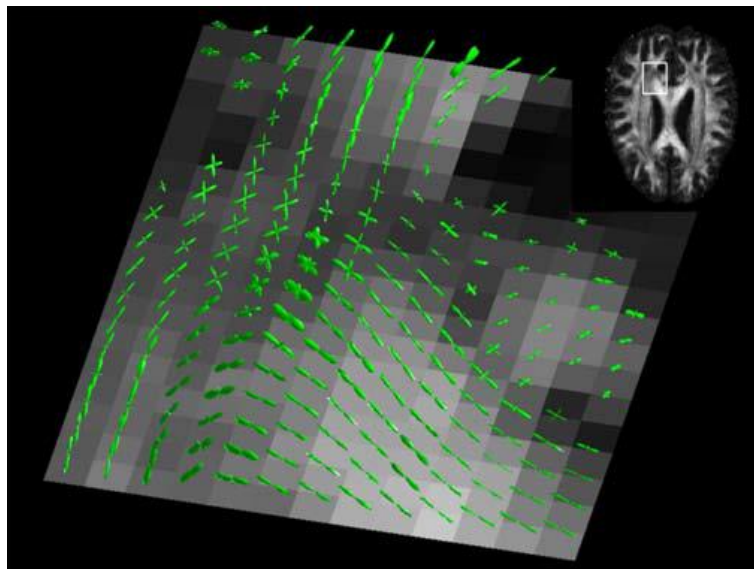
Figure 1.9. Example of FODs estimated by Spherical Deconvolution in a region with fiber crossing. Reproduced from [Dell'Acqua 2005]

The single fiber response can be assumed a priori to have a specific shape or can be estimated directly from the acquired data in highly anisotropic areas, where a single fiber population is expected. Obviously many features of WM influencing diffusion (packing

density, axon diameter, etc.) may vary from a region to another, so the single fiber response is only an approximation of the true fiber response. However, SD methods have shown high angular resolution and precision in the estimation of the ODF, with relatively short acquisition (HARDI schemes are usually applied) and computational times. The original formulation of SD is somewhat sensitive to noise, causing spurious directions and negative orientations; this issue has been addressed by regularization [Tournier 2007] or use of a more robust algorithm based on a modified version of the Richardson-Lucy algorithm [Dell'Acqua 2007, Dell'Acqua 2010].

1.5. Advanced methods focused on microstructure

This class of dMRI methods was developed for a better estimation of microstructural features of the biological tissues than allowed by DTI. Contrary to the techniques introduced in the previous paragraph, here the main focus is not on the identification of fiber directions, but on a more precise characterization of the statistical distribution of the displacements of water molecules in the different compartments of the tissue, and hence on the presence and spatial organization of biological structures.

Even though the main area of application of these methods is cerebral WM, they have found application also in the study of GM and other brain and body structures.

The general idea behind these methods is to go beyond the Gaussian model for diffusion. A model-free approach is Diffusion Kurtosis Imaging (DKI), which considers the higher order terms of the dMRI signal. However, to get parameters more specific to the microstructure of the tissue, the signal is usually analyzed with mathematical models, more complex than the diffusion tensor; most of them are multi-compartment models, expressing the signal as the sum of different terms describing different compartments of the tissue, often including models for restricted diffusion.

Many models have been proposed in the last years; a selection of the most historically important and relevant to the aim of this thesis will be here presented.

1.5.1. DKI

Diffusion Kurtosis Imaging (DKI, [Jensen 2005]) considers the cumulant expansion of the dMRI signal:

$$\ln(E) = -b \cdot ADC + \frac{1}{6}b^2 ADC^2 ADK + O(b^3) \qquad (1.10)$$

Neglecting the higher order terms $O(b^3)$, the signal is characterized by two parameters: the ADC and the Apparent Diffusion Kurtosis (ADK), also named "excess kurtosis" or just "kurtosis"; they can be estimated from data acquired with at least two non-zero b-values (generally obtained by increasing the gradient intensity with δ and Δ kept constant).

Figure 1.10 shows an ADC and an ADK map obtained in the first DKI study on a human brain [Jensen 2005].
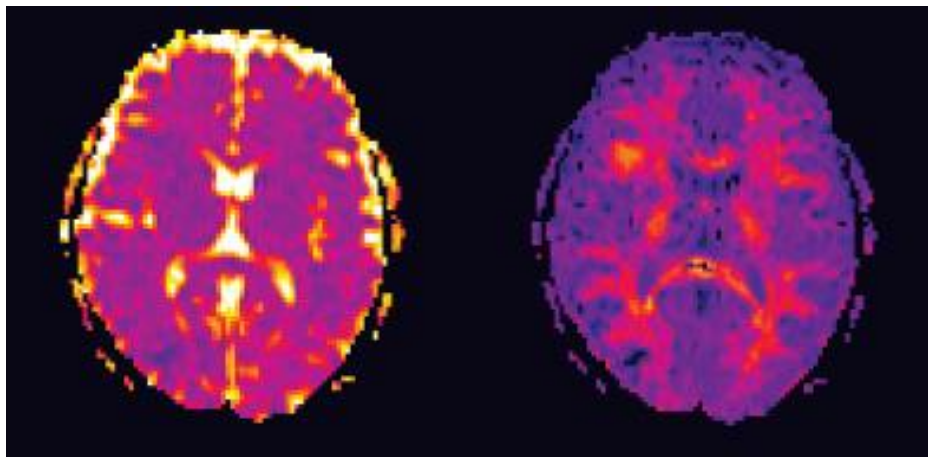
Figure 1.10. Examples of ADC (left) and ADK (right) maps in a human brain. Reproduced from [Jensen 2005]

The ADK is an index of the deviation from Gaussianity of the probability distribution of the displacement of water molecules. In general, a probability distribution has a positive kurtosis if it has more weight on its center and tails (it's "sharper") than a Gaussian distribution with the same variance, while it has a negative kurtosis if it has less weight on

its center and tails than a Gaussian distribution with the same variance. The logarithm of the dMRI signal decay E(b) corresponding to a displacement distribution with positive kurtosis is concave, while a negative kurtosis is associated with a convex shape of $ln(E(b))$. Conversely, a Gaussian distribution has null kurtosis and a linear decay of $ln(E(b))$. However, only positive or virtually null ADK values are generally found in biological tissues.

Since kurtosis is a measure of the deviation from Gaussianity and the most common reason for non-Gaussianity is restriction, the ADK has been interpreted as an index of restriction, or even of more specific features such as myelination or fiber density (for example [Cheung 2009]). Nevertheless, DKI does not imply any biophysical model, and thus it does not directly support any inference about the origin of the deviation from the Gaussian behavior.

In anisotropic systems, a "Kurtosis Tensor" can be introduced [Jensen 2010], with 81 components, of which only 15 are independent because of symmetry. In analogy to the parameters extracted from the diffusion tensor, the mean kurtosis, axial kurtosis, transversal kurtosis and kurtosis anisotropy have been defined [Hui 2008, Jensen 2010, Poot 2010]. The diffusion tensor and the kurtosis tensor together have 21 free parameters; their estimation requires the acquisition of dMRI images in multiple independent directions with multiple shells of diffusion weighting (multiple b-values).

1.5.2. Biexponential model

The biexponential model [Niendorf 1996] is the simplest multi-compartment extension of the Gaussian model. According to this model, the relationship between the dMRI signal and the b-value can be expressed as the sum of two exponential terms:

$$E = f_1 e^{-b \cdot D_1} + f_2 e^{-b \cdot D_2} \qquad (1.11)$$

where f and $f_2 = 1 - f_1$ are the fractions of the signal associated with the two compartments, and D_1 and D_2 are the apparent diffusivities within them.

The amount of deviation from the monoexponential decay depends on the nature of the tissue and on the acquisition parameters (figure 1.11). Among brain tissues, the CSF shows almost perfectly Gaussian free diffusion, while the biexponential behavior is much more important in GM and even more so in WM [Clark 2000].

Considering the dependence on the acquisition parameters, the non-Gaussian nature of diffusion is more evident with large b-values (higher than 1500-2000 s/mm^2) [Clark 2000]. So the data to be analyzed with the biexponential model are usually acquired with protocols including high b-values, which entail a trade-off between the sampling accuracy of the diffusion decay and the acquisition time needed to have a sufficient SNR.
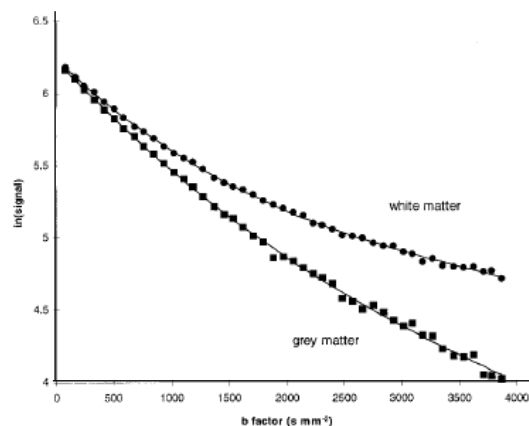
Figure 1.11. Biexponential decay of dMRI signal in GM and WM. Reproduced from [Clark 2000]

The components with low and high diffusivity have been associated with the intracellular and extracellular tissue compartment, respectively. However, this strict association has been questioned, since the estimated f_1 and f_2 do not correspond to the intracellular and extracellular fractions expected from histology [Niendorf 1996, Mulkern 1999].

Obviously, if 3 or more compartments are expected in the considered tissue, the biexponential model can be straightforwardly extended to a multiexponential by adding

further terms to equation (1.11) and two parameters per additional component (its volume fraction and the associated diffusivity).

So far the orientational dependence of the dMRI signal has been neglected, as it has been usually done in many studies, especially the first ones considering the biexponential model. If anisotropy is taken into account, the biexponential (or multiexponential) model becomes a Multi-Tensor, already described in paragraph1.4.1. Depending on the application, the focus is set on the direction of the tensors (as discussed above) or on the diffusion parameters extracted for each component (as discussed here). To reduce the complexity of the Multi-Tensor model and increase the fitting robustness, different constraints on the parameters can be accordingly set.

1.5.3. Models of restricted diffusion in standard geometries

As already mentioned in paragraph 1.3, q-space theory provides a tool for deriving the spin propagator from the dMRI signal in any condition, but its practical implementation is limited by many issues. Moreover, QSI has the advantages of model-free methods (for instance it can be applied in any sample), but the interpretation of its results may be not straightforward: often the estimated propagator conveys little intelligible information about microstructure and requires further assumptions to infer some conclusions, for example in clinical studies.

To exploit the q-space framework in the perspective of microstructure, a different approach is needed: to formulate a hypothesis about the geometry of the studied microenvironment and the characteristics of water diffusion in it, to develop a mathematical model of the corresponding dMRI signal with some free parameters, and to fit it to the data to estimate the parameters.

In particular, this approach is useful when diffusion is restricted, because in that case the spin propagator is strongly associated with the size and shape of the restricting

compartments. Mathematical models for restricted diffusion in standard geometries such as parallel planes, spheres and cylinders have been developed (for example, [Callaghan 1995, Codd 1999]). Since their general analytical form is often intractable, their formulation is usually based on either of two common approximations: the Short Gradient Pulse (SGP) or the Gaussian Phase Distribution (GPD) approximation [Price 1996].

The former is based on the hypothesis that the diffusion gradient pulses have null duration ($\delta \rightarrow 0$, which implies $g \rightarrow \infty$ for a finite diffusion weighting) and is usually considered valid when the gradient pulses are much shorter than the interval between them ($\delta << \Delta$). This condition allows assuming stationary spins during the pulses, but it is often very difficult to implement in typical experiments, especially on clinical MRI scanners. For this reason, in clinical research studies the GPD approximation is often applied: it is based on the hypothesis that the distribution of the phases of spins is Gaussian; this is true only in the case of free diffusion, but GPD accounts for the finite duration of gradient pulses, so it is usually a better approximation than SPG for data acquired on most MRI scanners.

The models for diffusion in the standard geometries mentioned above provide the basis for most multi-compartment models including compartments with restricted diffusion. A selection of them will be presented in the following paragraphs.

1.5.4. Ball and stick

The "ball and stick" [Behrens 2003] is a simple model for WM fibers with partial volume from CSF and/or GM.

It assumes that water molecules in WM are confined into "sticks", i.e. cylinders with null radii; this means that water can move only in the same direction of the fibers and is completely restricted in any perpendicular direction. All the remaining tissue in the voxel is described as a compartment with isotropic Gaussian diffusion.

The analytical form of the ball and stick model is:

$$E = (1 - f)exp(-b \cdot d) + f \cdot exp(-b \cdot d \cdot \boldsymbol{g}^T \mathbf{RAR^T}\boldsymbol{g}) \qquad (1.12)$$

where d is the diffusivity along the fibers and in the isotropic compartment, b is the b-value

and $\boldsymbol{g}$ the gradient direction for the considered acquisition volume, f is the fraction of the

signal relative to the fibers compartment, and $\mathbf{RAR^T}$ is the mathematical representation of

diffusion in a stick with an arbitrary orientation. Specifically, $\mathbf{A}$ is the representation of a

stick orientated along the x axis, which is a tensor with non-null diffusivity only along the x

direction:

$$\mathbf{A} = \begin{bmatrix} 1 & 0 & 0 \\ 0 & 0 & 0 \\ 0 & 0 & 0 \end{bmatrix} \qquad (1.13)$$

and $\mathbf{R}$ is the rotation matrix that rotates the x axis to the fiber direction (θ, ϕ).

This form of the "ball and stick" model assumes that each voxel has a single fiber direction.

However, it can be easily extended to a condition with two or more fiber directions by

adding terms similar to the second one in equation (1.12), or even to a condition with an

intra-voxel distribution of orientations H(θ,φ), as proposed already in [Behrens 2003]:

$$E = (1 - f)exp(-b \cdot d) + f \int_0^{2\pi} \int_0^\pi H(\theta, \phi) \, exp(-b \cdot d \cdot \boldsymbol{g}^T \mathbf{RAR^T}\boldsymbol{g})sin(\theta)d\theta d\phi \qquad (1.14)$$

Obviously the estimation of a full orientation distribution $H(\theta, \phi)$ requires a higher angular

resolution, and thus a quite complex acquisition protocol. On the contrary, for the simple

model in equation (1.12) a standard acquisition protocol is sufficient, similar to those

commonly applied for DTI, with a relatively low b-value (about 1000 s/mm^2) and a not very

large number of diffusion directions (of the order of few tens of independent directions).

1.5.5. CHARMED

The Composite Hindered And Restricted ModEl of Diffusion (CHARMED, [Assaf 2004]) is

another two-compartment model for the study of brain WM. It ascribes the dMRI signal

attenuation to two different processes in the intra-axonal (water inside the WM fibers) and

in the extra-axonal space (water between and outside the fibers). In the intra-axonal space diffusion is supposed to be restricted, while in the extra-axonal space diffusion is described as hindered (figure 1.12).

The exchange rate between the two compartments is supposed to be slow compared to the experimental times, then the signal is modeled as the sum of two independent components:

$$E = f_h E_h + f_r E_r \qquad (1.15)$$

where f_h and f_r are the T_2-weighted volume fractions of the extra-axonal (hindered) and intra-axonal (restricted) compartment, while E_h and E_r are the normalized signals describing diffusion within them.
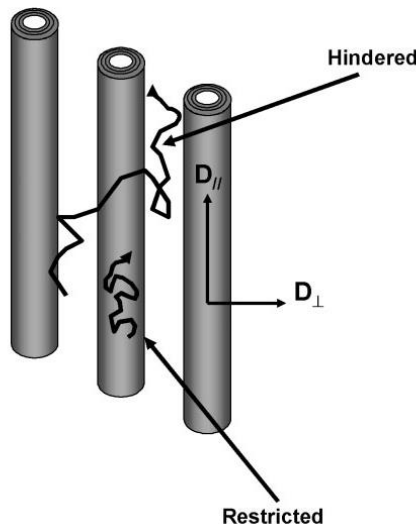
Figure 1.12. Pictorial representation of the CHARMED model, with restricted diffusion in cylinders and hindered restriction outside. Reproduced from [Assaf 2004]

The extra-axonal signal E$_h$ is characterized by a diffusion tensor **D**:

$$E_h = exp\left[-4\pi^2\left(\Delta - \frac{\delta}{3}\right)q^T \mathbf{D}q\right] \qquad (1.16)$$

where q is a vector having the q-value as a norm ($q = \gamma\delta g$) and the same direction of the diffusion gradients. Since anisotropy in the extra-axonal compartment probably derives from the tortuosity induced by the axons, neurofilaments and other structures with the

same orientation of the axons, **D** is expected to have the same principal direction of the intra-axonal compartment. It may be useful to rewrite equation (1.16) separating the terms in the direction parallel and perpendicular to the axon:

$$E_h = exp\left[-4\pi^2\left(\Delta - \frac{\delta}{3}\right)q_\parallel{}^2\lambda_\parallel\right]exp\left[-4\pi^2\left(\Delta - \frac{\delta}{3}\right)q_\perp{}^2\lambda_\perp\right] \qquad (1.17)$$

where $q_\parallel$ and $q_\perp$ are the q-values along the parallel and perpendicular direction, respectively.

The intra-axonal signal E_r is the signal decay for restricted diffusion in impermeable cylinders. It can be demonstrated that the contributions from molecules diffusing along the axons and in the perpendicular direction are independent, and E_r can be written as their product:

$$E_r = E_{r,\parallel}E_{r,\perp} \qquad (1.18)$$

For displacements in the axons along the axial direction, diffusion is supposed to be one-dimensional and free:

$$E_{r,\parallel} = exp\left[-4\pi^2\left(\Delta - \frac{\delta}{3}\right)q_\parallel{}^2 D_\parallel\right] \qquad (1.19)$$

where $D_\parallel$ is the diffusivity in the parallel direction.

The best approximation for diffusion in restricting cylinders was formulated by Codd and Callaghan [Codd 1999], but it is valid only under the SGP hypothesis. CHARMED is based on the formula by Neuman et al. [Neuman 1974], which is more mathematically tractable and more appropriate with standard diffusion gradient pulses:

$$E_{r,\perp} = exp\left[\frac{-8\pi^2 R^4 q_\perp{}^2}{D_\perp TE}\cdot\frac{7}{96}\left(2 - \frac{99}{112}\cdot\frac{2R^2}{D_\perp TE}\right)\right] \qquad (1.20)$$

where R is the radius of the cylinder, $D_\perp$ is the diffusivity in the perpendicular direction and TE is the echo time. In this implementation [Assaf 2004], R was supposed to follow a statistical distribution, fixed a priori to values derived from histological data.

It is straightforward to extend equation (1.15) to multiple hindered and/or restricted compartments:

$$E = \sum_{i=1}^{M} f_{h,i} E_h + \sum_{j=1}^{N} f_{r,j} E_r \qquad (1.21)$$

In particular, a version of CHARMED with one hindered and 2 or 3 restricted compartments is often applied [Assaf 2005, De Santis 2014], which permits to solve fiber crossing.

The acquisition scheme needed for CHARMED is a multi-shell protocol with multiple directions per shell, usually with increasing angular resolutions for higher b-values. For example, the acquisition protocol applied for the first application on human data [Assaf 2005] included 10 b-values ranging from 714 to 10000 s/mm^2 and 169 gradient directions in total, ranging from 6 to 30 in the different shells. The acquisition time was about 17 minutes, which is compatible with studies on patients, and the protocol was feasible on a 3T MRI scanner.

1.5.6. CHARMED extensions and simplifications

AxCaliber [Assaf 2008] is an extension of CHARMED allowing the estimation of axonal diameters from the dMRI signal. The main differences between AxCaliber and CHARMED are the following:

- AxCaliber is a 1D and not a 3D model: it assumes that the images are acquired with diffusion encoding in a direction perpendicular to the axons
- The expression for $E_{r,\perp}$ is based on the formula by Codd and Callaghan [Codd 1999]. AxCaliber was not intended for clinical research, at least initially, but for studies on ex vivo specimens and small animals with high-field MRI scanners; in these conditions the SGP approximation is realistic.

- The distribution of axonal diameters included in $E_{r,\perp}$ is not fixed a priori, but characterized by a gamma statistical distribution with two unknown parameters to be fitted.

- The acquisition protocol includes the repetition of a "CHARMED-like" multi-shell protocol with different values of Δ (ranging from about 10 ms to about 100-150 ms) to evaluate the signal with multiple diffusion times.

A further extension of AxCaliber, with an additional compartment with isotropic diffusion, was applied for the in vivo estimation of the axon diameter distribution in the corpus callosum of rat, validated by histology [Barazany 2009].

The possibility of estimating axon diameters in vivo gained the attention of MRI researchers, because the axon diameter is an important property of WM, one of the main factors determining the conduction velocity of nerves. AxCaliber showed promising results, but its clinical application is limited by many factors, such as the long acquisition time, the need to fulfill the SGP condition and the confinement to the cases in which the direction of fibers is known a priori (corpus callosum, spinal cord, excised nerves).

To allow the estimation of axon diameters in a more clinically-feasible setting, a simplification of CHARMED and AxCaliber models was proposed, named ActiveAx [Alexander 2008, Alexander 2010, Dyrby 2013]. The key differences between this simplified model and AxCaliber are the following:

- It assumes a single axon radius rather than a distribution

- The tensor characterizing the extracellular compartment has cylindrical symmetry:

$$\boldsymbol{D} = (d_{\parallel} - d_{\perp})\boldsymbol{n}\boldsymbol{n}^T + d_{\perp}\boldsymbol{I} \tag{1.22}$$

where $d_{\parallel}$ and $d_{\perp}$ are the axial and radial diffusivities, $\boldsymbol{n}$ is the first eigenvector of the tensor and $\boldsymbol{I}$ is the identity matrix

- The first eigenvector $\boldsymbol{n}$ of the tensor is constrained to be the direction of the cylinders in the intra-axonal compartment

- The intrinsic diffusivities of the intra- and extra-axonal compartments are constrained to be the same and equal to $d_\parallel$.

- The expression for $E_{r,\perp}$ is based on the formula by Van Gelderen et al. [Van Gelderen 1994]:

$$E_{r,\perp} = exp\left[-2\gamma^2 G_\perp{}^2 \sum_{m=1}^{\infty} \frac{2d_\parallel \alpha_m{}^2 \delta - 2 + 2exp(-d_\parallel \alpha_m{}^2 \delta) + 2exp(-d_\parallel \alpha_m{}^2 \Delta) - exp\left(-d_\parallel \alpha_m{}^2 (\Delta - \delta)\right) - exp\left(-d_\parallel \alpha_m{}^2 (\Delta + \delta)\right)}{d_\parallel{}^2 \alpha_m{}^6 (R^2 \alpha_m{}^2 - 1)}\right] \quad (1.23)$$

where $G_\perp$ is the gradient intensity in the direction perpendicular to the fiber, α_m is the mth root of $J_1{}'(\alpha R) = 0$, R is the radius of the cylinder and $J_1{}'$ is the derivative of the Bessel function of the first kind, order 1.

The free parameters of this simplified model are: f (the volume fraction of the intra-axonal compartment), $\mathbf{n}$, R, $d_\parallel$ and $d_\perp$.

Finally, this model was extended to a four-compartment model named Minimal Model of White Matter Diffusion (MMWMD, [Alexander 2010]):

$$E = f_1 E_1 + f_2 E_2 + f_3 E_3 + f_4 E_4 \quad (1.24)$$

E_1 is the normalized signal coming from intra-axonal water (restriction in cylinders with equal diameter, as in the previous model).

E_2 is the normalized signal coming from extra-axonal water, adjacent to, but outside, the cylinders; it is modeled by a cylindrically-symmetric diffusion tensor as in the previous model, but with the addition of a constraint relating $d_\parallel$ and $d_\perp$ values according to a simple tortuosity model [Szafer 1995]:

$$d_\perp = d_\parallel \frac{f_2}{f_1 + f_2} \quad (1.25)$$

E_3 is the normalized signal coming from CSF, where diffusion is not affected by the fibers; it is modeled as isotropic Gaussian diffusion.

E_4 is the normalized signal coming from stationary water, trapped in glial cells and other small compartments or bound to membranes and other subcellular structures; it is not attenuated by diffusion, so $E_4 = 1$.

1.5.7. NODDI

The Neurite Orientation Dispersion and Density Imaging (NODDI, [Zhang 2012]) is a recent technique based on the MMWMD. Differently from the models described above, which considers a single fiber orientation per compartment, it account for the orientation dispersion of neurites (axons and dendrites). With respect to the MMWMD, some simplifications are assumed to keep it clinically feasible; in particular, the cylinders are substituted by sticks as in [Behrens 2003] and the compartment with isotropic restriction from stationary water is neglected.

The NODDI mathematical model is:

$$E = (1 - f_{ISO})[f_{IC}E_{IC} + (1 - f_{IC})E_{EC}] + f_{ISO}E_{ISO} \qquad (1.26)$$

where E_{IC}, E_{EC} and E_{ISO} are the normalized signal expressions for the intra-cellular, extra-cellular and CSF compartment, respectively; f_{ISO} and f_{IC} are the volume fractions of the intra-cellular and CSF compartment, respectively.

The intra-cellular compartment refers to the space bounded by the membrane of neurites and is modeled as a set of sticks, with free diffusion along them and highly restricted diffusion in the perpendicular direction. The expression for E_{IC} was derived by simplifying the orientation-dispersed cylinder model in [Zhang 2011] for the case of sticks:

$$E_{IC} = \int_{\mathbb{S}^2} f(\boldsymbol{n}) \, exp[-bd_{\parallel}(\boldsymbol{g} \cdot \boldsymbol{n})^2]d\boldsymbol{n} \qquad (1.27)$$

where $\boldsymbol{g}$ and b are the gradient direction and b-value, $f(\boldsymbol{n})d\boldsymbol{n}$ is the probability of finding sticks along orientation $\boldsymbol{n}$ and $exp[-bd_{\parallel}(\boldsymbol{g} \cdot \boldsymbol{n})^2]$ is the signal attenuation due to diffusion along a stick with orientation $\boldsymbol{n}$ and intrinsic diffusivity $d_{\parallel}$. The orientation distribution $f: \mathbb{S}^2 \to \mathbb{R}$ is defined as a Watson distribution:

$$f(\boldsymbol{n}) = M\left(\frac{1}{2}, \frac{3}{2}, \kappa\right)^{-1} exp[\kappa(\boldsymbol{\mu} \cdot \boldsymbol{n})^2] \qquad (1.28)$$

where M is a confluent hypergeometric function, $\boldsymbol{\mu}$ is the mean orientation, and κ is the concentration parameter that measures the extent of orientation dispersion about $\boldsymbol{\mu}$. κ is constrained to be positive to avoid ring-shaped distributions, so it ranges from 0 for completely dispersed orientations to ∞ for perfectly aligned fibers. To characterize the orientation dispersion in a more intuitive way, the Orientation Density Index (ODI) was defined:

$$ODI = \frac{2}{\pi} arctan\left(\frac{1}{\kappa}\right) \qquad (1.29)$$

which ranges from 0 for perfect alignment to 1 for maximum dispersion.
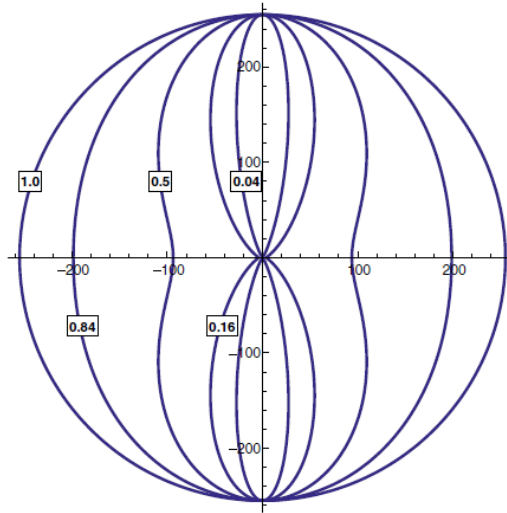
Figure 1.13. Illustration of a set of Watson distribution with the same mean direction but different ODI (0.04, 0.16, 0.5, 0.84, 1.0). Reproduced from [Zhang 2012]

The extra-cellular compartment refers to the space around the neurites, which is occupied by various types of cells; diffusion in this space is modeled as hindered but not restricted by the presence of neurites, so it is characterized by a diffusion tensor. The expression for E_{EC} is:

$$E_{EC} = exp(-b\boldsymbol{g}^T\boldsymbol{D}_{EC}\boldsymbol{g}) \qquad (1.30)$$

where $\boldsymbol{D}_{EC}$ is the apparent diffusion tensor for the extra-cellular compartment and depends on the axonal orientation distribution:

$$D_{EC} = \int_{\mathbb{S}^2} f(n)\, D(n) dn \qquad (1.31)$$

where $D(n)$ is a cylindrically symmetric diffusion tensor having n as the first eigenvector, axial diffusivity $d_\parallel$ (equal to the intrinsic diffusivity along the sticks in the intra-cellular compartment) and radial diffusivity $d_\perp = d_\parallel(1 - f_{IC})$. The apparent extra-cellular diffusion tensor D_{EC} has axial and radial diffusivity equal to $d_\parallel{}'$ and $d_\perp{}'$ respectively:

$$d'_\parallel = d_\parallel\big(1 - f_{IC}(1 - \tau)\big) \qquad (1.32)$$

$$d'_\perp = d_\parallel\left(1 - f_{IC}\frac{1 + \tau}{2}\right) \qquad (1.33)$$

where τ captures the effect of orientation dispersion on the apparent diffusivities:

$$\tau = \frac{\int_0^1 u^2 exp(\kappa u^2) du}{\int_0^1 exp(\kappa u^2) du} \qquad (1.34)$$

τ ranges from $\frac{1}{3}$ for $\kappa = 0$ to 1 for $\kappa \to \infty$.

In the case of perfectly aligned fibers ($ODI = 0$, $\kappa \to \infty, \tau = 1$), $d'_\parallel = d_\parallel$ and $d'_\perp = d_\parallel(1 - f_{IC}) = d_\perp$, so D_{EC} coincides with $D(\mu)$.

In the case of maximum dispersion ($ODI = 1$, $\kappa = 0$, $\tau = \frac{1}{3}$), $d'_\parallel = d'_\perp = d_\parallel\left(1 - \frac{2}{3}f_{IC}\right)$, so D_{EC} is isotropic.

The CSF compartment is modeled as isotropic Gaussian diffusion with diffusivity d_{ISO}:

$$E_{ISO} = exp(-b \cdot d_{ISO}) \qquad (1.35)$$

The complete set of NODDI parameters includes: f_{IC}, $d_\parallel$, κ, μ, f_{ISO} and d_{ISO}, but the diffusivities are fixed to $d_\parallel = 1.7 \cdot 10^{-3}$ mm^2/s and $d_{ISO} = 3 \cdot 10^{-3}$ mm^2/s, which are typical values for in vivo experiments. Thus only the 4 remaining parameters need to be estimated from the data. Maps of the parameters obtained for a healthy subject in [Zhang 2012] are shown in figure 1.14
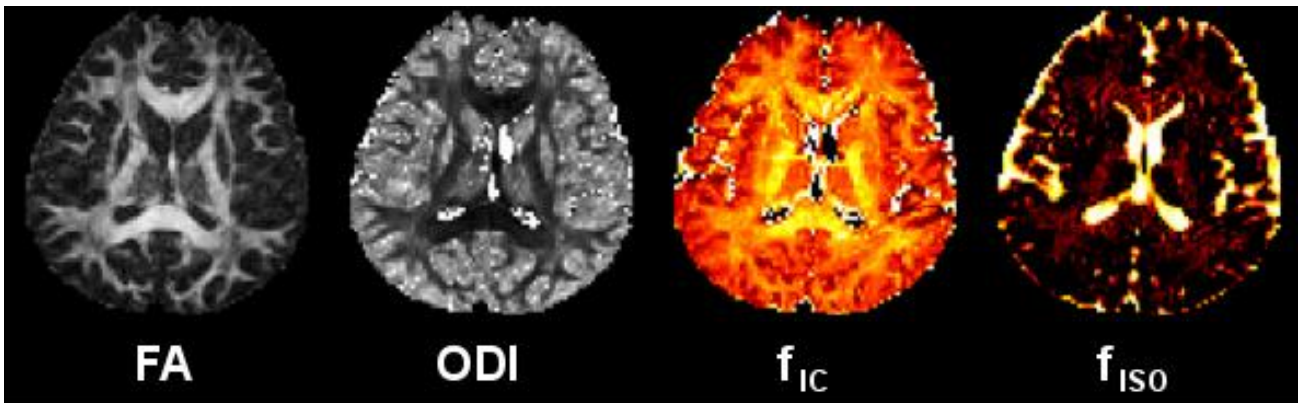
Figure 1.14. Representative maps of the main NODDI parameters (and of FA for comparison) obtained in the brain of a healthy subject. Reproduced from [Zhang 2012]

The acquisition protocol optimized in [Zhang 2012] on a 3T MRI scanners with an acquisition time limit of 30 minutes included two shells with b = 711 s/mm^2 and b = 2855 s/mm^2, 30 and 60 gradient directions, respectively.

The main advantage of NODDI over the other multi-compartment models is that it provides interesting and specific information about tissue microstructure with a clinically feasible framework. The volume fractions f_{IC} and f_{ISO} can be considered as indices of neurite density and of the partial volume from CSF, respectively, while the ODI (derived from κ) quantifies neurite orientation dispersion, thus differentiating tissues with highly coherent fibers, such as the main WM bundles, from tissues where the neurites are more dispersed, such as GM.

Neurite morphology varies with brain development, aging and neurodegenerative disease, so NODDI could have many important applications in clinical studies. Indeed, two recent works applying NODDI to human data have been published.

In [Winston 2013] NODDI was used to investigate the variations of microstructural parameters in patients with focal cortical dysplasia. In all the patients the areas of dysplasia identified by morphological MRI and DTI showed reduced f_{IC}; in an additional patient an area with reduced f_{IC} and increased ODI was found, not identified on the other MRI and DTI images.

In [Kunz 2014], NODDI and CHARMED were used to evaluate microstructural features of brain WM in newborns. In particular, structures with late maturation characterized by thin non-myelinated fibers are associated to lower f_{IC} values, while regions with fiber crossing and fanning have high ODI values.

1.6. Tractography

Fiber tractography [Mori 1999, Jones 1999, Basser 2000] is a procedure aiming at virtually reconstructing the trajectories of WM fiber bundles by connecting local fiber orientations. It is one of the main applications of dMRI models.

The local fiber orientation is usually the first eigenvector of the diffusion tensor (Diffusion Tensor Tractography, DTT), but it can be derived by any dMRI technique. In particular, most of the methods described in paragraph 1.4 were specifically developed for tractography, but also the models developed for microstructural tissue characterization (paragraph 1.5) can be applied. In the following overview, not intended to be complete, some DTT algorithms will be presented, because they have been the first to be developed and are still the most popular; however, the same concepts can be generally extended to use fiber directions estimated by other dMRI methods.

Deterministic streamline tractography is the simplest and most common approach for tractography. The basic idea is to create streamlines through the vector field composed by the tensor principal directions, which are lines having local tangents parallel to the local vectors of the field. Mathematically, this is expressed by the following condition:

$$\frac{d\boldsymbol{r}(s)}{ds} = \boldsymbol{e}_1\big(\boldsymbol{r}(s)\big) \tag{1.36}$$

where $\boldsymbol{r}(s)$ are the 3D coordinates at position s along the streamline and $\boldsymbol{e}_1$ is the vector field of the first eigenvector of the diffusion tensor.

One method to solve this integration problem is the Fiber Assignment by Continuous Tracking (FACT, [Mori 1999]). It consists in starting to track from the center of a voxel and following the direction of the local tensor until the streamline reaches a border of the voxel, where the direction is changed to that of the tensor in the adjacent voxel (figure 1.15).
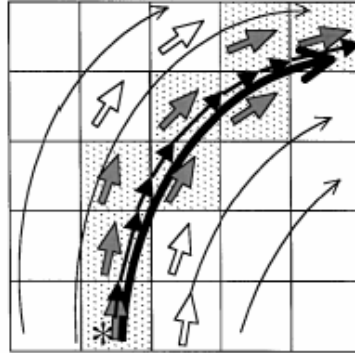
Figure 1.15. Schematic representation of the principle of the FACT tractography method. Reproduced from [Mori 1999]

Another approach is to follow the direction of the tensor only for a short fixed distance Δ (called step size) and then change it; this requires interpolating the vector field at arbitrary positions in space, which is usually done by trilinear interpolation. There are many algorithms for this approach; the most intuitive is Euler integration, which reconstructs the streamlines by iteratively performing this procedure:

$$r_{i+1} = r_i + e_1(r_i)\Delta \tag{1.37}$$

Euler integration assumes that $v(r_i)$ is constant throughout the step size Δ, so it can underestimate the curvature of fibers for large step sizes. A higher order integration algorithm, accounting for the variations of $v(r)$ between r_i and r_{i+1} is the second-order Runge-Kutta method, which consists in iterating this procedure:

$$r_{i+1} = r_i + e_1\left(r_i + e_1(r_i)\frac{\Delta}{2}\right)\Delta \tag{1.38}$$

A deterministic approach different from streamline tractography is tensorline tractography or tensor deflection [Lazar 2003], using the full diffusion tensor to determine the propagation direction:

$$r_{i+1} = r_i + \Delta \, \boldsymbol{D}(r_i) \cdot (r_i - r_{i-1}) \tag{1.39}$$

Tensorline tractography deflects the propagation direction towards the first eigenvector, but limits the amount of deflection when the tensor is less linear, suggesting higher intra-voxel heterogeneity. As a result, the track reconstruction is smoother.

Whichever deterministic tractography algorithm is used, the tracking process needs to be stopped at a certain point. For DTT, at least two termination criteria are commonly set: an anisotropy threshold and a curvature threshold. The rationale behind the anisotropy threshold is that in regions with low anisotropy (for example CSF and GM) the estimation of the principal diffusion direction is highly uncertain, so the probability of following a wrong direction is high. For this purpose, the tracking process is usually limited to the voxels with FA > 0.2. The rationale for the curvature threshold is that WM bundles are not expected to have a radius of curvature on the scale of image resolution, and then very sharp bends are likely caused by artifacts. For this purpose, a curvature or an angle threshold between consecutive steps is applied; even though the latter depends on the step size, it is the most common choice, with values between about 10° and 60°.

Deterministic tractography assumes the fiber direction coincides with the first eigenvector of the local diffusion tensor, but the estimation of the diffusion tensor is affected by uncertainty. To take this uncertainty into account, several probabilistic tractography algorithms [Lazar 2004, Jones 2005, Behrens 2007] have been developed. There are many different methodologies, but the general idea behind most probabilistic tractography methods is to consider multiple directions per voxel in the tracking process and to estimate the confidence of each reconstructed streamline. Thus, probabilistic methods can track fibers also through regions with high uncertainty in the determination of the principal direction, and quantify this uncertainty.

Finally, another different approach is global tractography [Jbabdi 2007]. Instead of propagating the locally estimated directions, the global tractography algorithms look for the

fiber configuration that best explains the dMRI data. They have great potential advantages on local algorithms, especially in terms of robustness, but their application is limited by their extreme computational cost.

Diffusion tractography has many applications in the study of normal and pathological WM. In particular, several tractography studies investigated WM connections during normal brain development [Watts 2003] or aging [Michielse 2010] and in pathologies as multiple sclerosis [Mesaros 2012], amyotrophic lateral sclerosis [Bastin 2013] or schizophrenia [Kubicki 2011]. Moreover, many works combined diffusion tractography with functional MRI to study structural and functional connections involved in the visual system [Toosy 2004], in the motor system [Guye 2003, Magro 2014] or in language [Henry 2004, Catani 2005, Bizzi 2012, Catani 2013]; an example of tractography of the language pathways is shown in figure 1.16. Finally, tractography plays an important role in treatment planning for radiation therapy [Maruyama 2005] and neurosurgery, as will be described in detail in chapter 4. This was only a limited survey of tractography applications, which are growing and expanding in many areas.
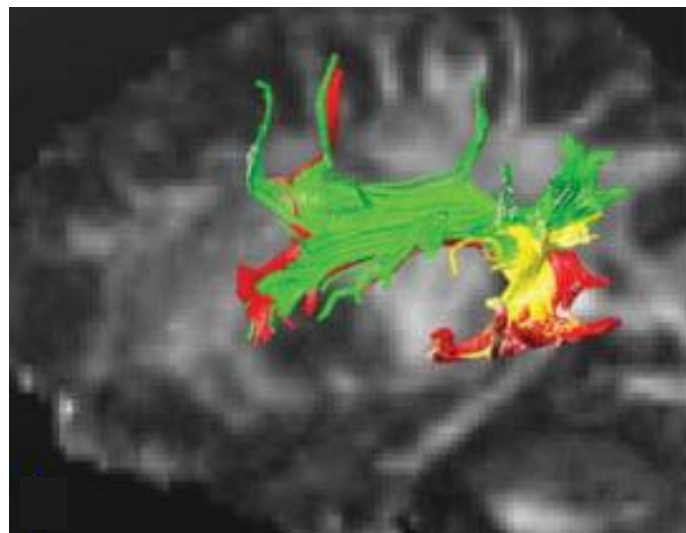
Figure 1.16. Tractography reconstruction of the direct and indirect language pathways (arcuate fasciculus) in a healthy subject, superimposed on a sagittal FA map; the different colors correspond to different segments of the arcuate fasciculus. Reproduced from [Catani 2005]

Bibliography

Alexander DC. A general framework for experiment design in diffusion MRI and its application in measuring direct tissue-microstructure features. *Magn Reson Med*. 2008;60(2):439-448.

Alexander DC, Hubbard PL, Hall MG, et al. Orientationally invariant indices of axon diameter and density from diffusion MRI. *Neuroimage*. 2010;52(4):1374-1389.

Assaf Y, Basser PJ. Composite hindered and restricted model of diffusion (CHARMED) MR imaging of the human brain. *Neuroimage*. 2005;27(1):48-58.

Assaf Y, Blumenfeld-Katzir T, Yovel Y, Basser PJ. AxCaliber: a method for measuring axon diameter distribution from diffusion MRI. *Magn Reson Med*. 2008;59(6):1347-1354.

Assaf Y, Freidlin RZ, Rohde GK, Basser PJ. New modeling and experimental framework to characterize hindered and restricted water diffusion in brain white matter. *Magn Reson Med*. 2004;52(5):965-978.

Barazany D, Basser PJ, Assaf Y. In vivo measurement of axon diameter distribution in the corpus callosum of rat brain. *Brain*. 2009;132(Pt 5):1210-1220.

Basser PJ, Mattiello J, LeBihan D. MR diffusion tensor spectroscopy and imaging. *Biophys J*. 1994;66(1):259-267.

Basser PJ, Pajevic S, Pierpaoli C, Duda J, Aldroubi A. In vivo fiber tractography using DT-MRI data. *Magn Reson Med*. 2000;44(4):625-632.

Basser PJ, Pierpaoli C. Microstructural and physiological features of tissues elucidated by quantitative-diffusion-tensor MRI. 1996. *J Magn Reson*. 2011;213(2):560-570.

Bastin ME, Pettit LD, Bak TH, Gillingwater TH, Smith C, Abrahams S. Quantitative tractography and tract shape modeling in amyotrophic lateral sclerosis. *JMRI-J Magn Reson Im*. 2013;38(5):1140-1145.

Behrens TEJ, Berg HJ, Jbabdi S, Rushworth MFS, Woolrich MW. Probabilistic diffusion tractography with multiple fibre orientations: What can we gain? *Neuroimage*. 2007;34(1):144-155.

Behrens TEJ, Woolrich MW, Jenkinson M, et al. Characterization and propagation of uncertainty in diffusion-weighted MR imaging. *Magn Reson Med*. 2003;50(5):1077-1088.

Bizzi A, Nava S, Ferrè F, et al. Aphasia induced by gliomas growing in the ventrolateral frontal region: assessment with diffusion MR tractography, functional MR imaging and neuropsychology. *Cortex*. 2012;48(2):255-272.

Brown R. A brief account of microscopical observations made in the months of June, July and August, 1827, on the particles contained in the pollen of plants; and on the general existence of active molecules in organic and inorganic bodies. *Philos Mag*. 1828;4:161-173.

Callaghan PT. Pulsed-Gradient Spin-Echo NMR for Planar, Cylindrical, and Spherical Pores under Conditions of Wall Relaxation. *J Magn Reson Ser A*. 1995;113(1):53-59.

Callaghan PT, MacGowan D, Packer KJ, Zelaya FO. High-resolution q-space imaging in porous structures. *J Magn Reson*. 1990;90(1):177-182.

Catani M, Dell'Acqua F, Vergani F, et al. Short frontal lobe connections of the human brain. *Cortex*. 2012;48(2):273-291.

Catani M, Jones DK, Ffytche DH. Perisylvian language networks of the human brain. *Ann Neurol*. 2005;57(1):8-16.

Catani M, Mesulam MM, Jakobsen E, et al. A novel frontal pathway underlies verbal fluency in primary progressive aphasia. *Brain*. 2013;136(Pt 8):2619-2628.

Cheung MM, Hui ES, Chan KC, Helpern JA, Qi L, Wu EX. Does diffusion kurtosis imaging lead to better neural tissue characterization? A rodent brain maturation study. *Neuroimage*. 2009;45(2):386-392.

Clark CA, Barrick TR, Murphy MM, Bell BA. White matter fiber tracking in patients with space-occupying lesions of the brain: a new technique for neurosurgical planning? *Neuroimage*. 2003;20(3):1601-1608.

Clark CA, Le Bihan D. Water diffusion compartmentation and anisotropy at high b values in the human brain. *Magn Reson Med*. 2000;44(6):852-859.

Codd SL, Callaghan PT. Spin Echo Analysis of Restricted Diffusion under Generalized Gradient Waveforms: Planar, Cylindrical, and Spherical Pores with Wall Relaxivity. *J Magn Reson*. 1999;137(2):358-372.

Cory DG, Garroway AN. Measurement of translational displacement probabilities by NMR : an indicator of compartmentation. *Magn Reson Med*. 1990;14(3):435-444.

De Santis S, Assaf Y, Evans CJ, Jones DK. Improved precision in CHARMED assessment of white matter through sampling scheme optimization and model parsimony testing. *Magn Reson Med*. 2014;71(2):661-671.

Dell'Acqua F, Rizzo G, Scifo P, Clarke RA, Scotti G, Fazio F. A model-based deconvolution approach to solve fiber crossing in diffusion-weighted MR imaging. *IEEE Trans Biomed Eng*. 2007;54(3):462-472.

Dell'Acqua F, Rizzo G, Scifo P, et al. A Deconvolution Approach Based on Multi-Tensor Model to Solve Fiber Crossing in Diffusion-MRI. *Conf Proc IEEE Eng Med Biol Soc*. 2005;2:1415-1418.

Dell'Acqua F, Scifo P, Rizzo G, et al. A modified damped Richardson-Lucy algorithm to reduce isotropic background effects in spherical deconvolution. *Neuroimage*. 2010;49(2):1446-1458.

Dyrby TB, Søgaard L V, Hall MG, Ptito M, Alexander DC. Contrast and stability of the axon diameter index from microstructure imaging with diffusion MRI. *Magn Reson Med*. 2012;70(3):711-721.

Einstein A. Über die von der molekularkinetischen Theorie der Wärme geforderte Bewegung von in ruhenden Flüssigkeiten suspendierten Teilchen. *Ann Phys*. 1905;17:549-560.

Filippi M, Inglese M. Overview of diffusion-weighted magnetic resonance studies in multiple sclerosis. *J Neurol Sci*. 2001;186:S37-S43.

Frank LR. Anisotropy in high angular resolution diffusion-weighted MRI. *Magn Reson Med*. 2001;45(6):935-939.

Guye M, Parker GJM, Symms M, et al. Combined functional MRI and tractography to demonstrate the connectivity of the human primary motor cortex in vivo. *Neuroimage*. 2003;19(4):1349-1360.

Henry RG, Berman JI, Nagarajan SS, Mukherjee P, Berger MS. Subcortical pathways serving cortical language sites: initial experience with diffusion tensor imaging fiber tracking combined with intraoperative language mapping. *Neuroimage*. 2004;21(2):616-622.

Hosey TP, Harding SG, Carpenter TA, Ansorge RE, Williams GB. Application of a probabilistic double-fibre structure model to diffusion-weighted MR images of the human brain. *Magn Reson Imaging*. 2008;26(2):236-245.

Hosey T, Williams G, Ansorge R. Inference of multiple fiber orientations in high angular resolution diffusion imaging. *Magn Reson Med*. 2005;54(6):1480-1489.

Hui ES, Cheung MM, Qi L, Wu EX. Advanced MR diffusion characterization of neural tissue using directional diffusion kurtosis analysis. *Conf Proc IEEE Eng Med Biol Soc*. 2008;2008:3941-3944.

Jbabdi S, Woolrich MW, Andersson JLR, Behrens TEJ. A Bayesian framework for global tractography. *Neuroimage*. 2007;37(1):116-129.

Jensen JH, Helpern JA. MRI quantification of non-Gaussian water diffusion by kurtosis analysis. *NMR Biomed*. 2010;23(7):698-710.

Jensen JH, Helpern JA, Ramani A, Lu H, Kaczynski K. Diffusional kurtosis imaging: the quantification of non-gaussian water diffusion by means of magnetic resonance imaging. *Magn Reson Med*. 2005;53(6):1432-1440.

Jeurissen B, Leemans A, Tournier J-D, Jones DK, Sijbers J. Investigating the prevalence of complex fiber configurations in white matter tissue with diffusion magnetic resonance imaging. *Hum Brain Mapp*. 2013;34(11):2747-2766

Jones DK. The effect of gradient sampling schemes on measures derived from diffusion tensor MRI: a Monte Carlo study. *Magn Reson Med*. 2004;51(4):807-815.

Jones DK, Pierpaoli C. Confidence mapping in diffusion tensor magnetic resonance imaging tractography using a bootstrap approach. *Magn Reson Med*. 2005;53(5):1143-1149.

Jones DK, Simmons A, Williams SC, Horsfield MA. Non-invasive assessment of axonal fiber connectivity in the human brain via diffusion tensor MRI. *Magn Reson Med*. 1999;42(1):37-41.

Komlosh ME, Horkay F, Freidlin RZ, Nevo U, Assaf Y, Basser PJ. Detection of microscopic anisotropy in gray matter and in a novel tissue phantom using double Pulsed Gradient Spin Echo MR. *J Magn Reson*. 2007;189(1):38-45.

Kubicki M, Alvarado JL, Westin C-F, et al. Stochastic tractography study of Inferior Frontal Gyrus anatomical connectivity in schizophrenia. *Neuroimage*. 2011;55(4):1657-1664.

Kunz N, Zhang H, Vasung L, et al. Assessing white matter microstructure of the newborn with multi-shell diffusion MRI and biophysical compartment models. *Neuroimage*. 2014;96C:288-299.

Lazar M, Alexander AL. Bootstrap white matter tractography (BOOT-TRAC). *Neuroimage*. 2005;24(2):524-532.

Lazar M, Weinstein DM, Tsuruda JS, et al. White matter tractography using diffusion tensor deflection. *Hum Brain Mapp*. 2003;18(4):306-321.

Le Bihan D, Breton E, Lallemand D, Aubin M-L, Vignaud J, Laval-Jeantet M. Separation of diffusion and perfusion in intravoxel incoherent motion MR imaging. *Radiology*. 1988;168(2):497-505.

Magro E, Moreau T, Seizeur R, Zemmoura I, Gibaud B, Morandi X. Connectivity within the primary motor cortex: a DTI tractography study. *Surg Radiol Anat*. 2014;36(2):125-135.

Maruyama K, Kamada K, Shin M, et al. Integration of three-dimensional corticospinal tractography into treatment planning for gamma knife surgery. *J Neurosurg*. 2005;102(4):673-677.

Mesaros S, Rocca MA, Kacar K, et al. Diffusion tensor MRI tractography and cognitive impairment in multiple sclerosis. *Neurology*. 2012;78(13):969-975.

Michielse S, Coupland N, Camicioli R, et al. Selective effects of aging on brain white matter microstructure: a diffusion tensor imaging tractography study. *Neuroimage*. 2010;52(4):1190-1201.

Mori S, Barker PB. Diffusion Magnetic Resonance Imaging: Its Principle and Applications. *Anat Rec*. 1999;257:102-109.

Mori S, Crain BJ, Chacko VP, van Zijl PCM. Three-dimensional tracking of axonal projections in the brain by magnetic resonance imaging. *Ann Neurol*. 1999;45:265-269.

Mulkern R V, Gudbjartsson H, Westin CF, et al. Multi-component apparent diffusion coefficients in human brain. *NMR Biomed*. 1999;12(1):51-62.

Neuman CH. Spin echo of spins diffusing in a bounded medium. *J Chem Phys*. 1974;60(11):4508.

Niendorf T, Dijkhuizen RM, Norris DG, van Lookeren Campagne M, Nicolay K. Biexponential diffusion attenuation in various states of brain tissue: implications for diffusion-weighted imaging. *Magn Reson Med*. 1996;36(6):847-857.

Poot DHJ, den Dekker AJ, Achten E, Verhoye M, Sijbers J. Optimal experimental design for diffusion kurtosis imaging. *IEEE Trans Med Imaging*. 2010;29(3):819-829.

Price WS. Pulsed-Field Gradient Nuclear Magnetic Resonance as a Tool for Studying Translational Diffusion. Part 1. Basic Theory. *Concept Magn Res*. 2010;28(50):299-335.

Schonberg T, Pianka P, Hendler T, Pasternak O, Assaf Y. Characterization of displaced white matter by brain tumors using combined DTI and fMRI. *Neuroimage*. 2006;30(4):1100-1111.

Sotak CH. The role of diffusion tensor imaging in the evaluation of ischemic brain injury - a review. *NMR Biomed*. 2002;15(7-8):561-569.

Stejskal EO, Tanner JE. Spin Diffusion Measurements: Spin Echoes in the Presence of a Time-Dependent Field Gradient. *J Chem Phys*. 1965;42(1):288.

Szafer A, Zhong J, Gore JC. Theoretical Model for Water Diffusion in Tissues. *Magn Reson Med*. 1995;33(5):697-712.

Thivard L, Lehéricy S, Krainik A, et al. Diffusion tensor imaging in medial temporal lobe epilepsy with hippocampal sclerosis. *Neuroimage*. 2005;28(3):682-690.

Toosy AT, Ciccarelli O, Parker GJM, Wheeler-Kingshott CAM, Miller DH, Thompson AJ. Characterizing function-structure relationships in the human visual system with functional MRI and diffusion tensor imaging. *Neuroimage*. 2004;21(4):1452-1463.

Tournier J-D, Calamante F, Connelly A. Robust determination of the fibre orientation distribution in diffusion MRI: non-negativity constrained super-resolved spherical deconvolution. *Neuroimage*. 2007;35(4):1459-1472.

Tournier J-D, Calamante F, Gadian DG, Connelly A. Direct estimation of the fiber orientation density function from diffusion-weighted MRI data using spherical deconvolution. *Neuroimage*. 2004;23(3):1176-1185.

Tuch DS. Q-ball imaging. *Magn Reson Med*. 2004;52(6):1358-1372.

Tuch DS, Reese TG, Wiegell MR, Makris N, Belliveau JW, Wedeen VJ. High angular resolution diffusion imaging reveals intravoxel white matter fiber heterogeneity. *Magn Reson Med*. 2002;48(4):577-582.

Watts R, Liston C, Niogi S, Uluğ AM. Fiber tracking using magnetic resonance diffusion tensor imaging and its applications to human brain development. *Ment Retard Dev Disabil Res Rev*. 2003;9(3):168-177.

Wedeen VJ, Reese TG, Tuch DS, et al. Mapping fiber orientation spectra in cerebral white matter with Fourier-transform diffusion MRI. *Proc Intl Soc Mag Reson Med*. 2000;8:5627.

Winston GP, Micallef C, Symms MR, Alexander DC, Duncan JS, Zhang H. Advanced diffusion imaging sequences could aid assessing patients with focal cortical dysplasia and epilepsy. *Epilepsy Res.* 2014;108(2):336-339.

Zhang H, Hubbard PL, Parker GJM, Alexander DC. Axon diameter mapping in the presence of orientation dispersion with diffusion MRI. *Neuroimage*. 2011;56(3):1301-1315.

Zhang H, Schneider T, Wheeler-Kingshott CAM, Alexander DC. NODDI: practical in vivo neurite orientation dispersion and density imaging of the human brain. *Neuroimage*. 2012;61(4):1000-1016.

2. MODEL-BASED ANALYSIS OF dMRI SIGNAL IN CJD PATIENTS

Essentially, all models are wrong, but some are useful

George E. P. Box

This chapter addresses the application of isotropic multi-compartment models to the analysis of damaged GM tissue in Creutzfeld-Jacob Disease. The study was developed thanks to a cooperation among the University College of London, the IRCCS Foundation Neurological Institute "C. Besta" and the Politecnico di Milano. It resulted in the scientific paper by Figini et al. [Figini 2014].

2.1. Introduction: Creutzfeldt-Jakob Disease and dMRI

Prion diseases are transmissible, rapidly progressive and fatal neurological diseases. Despite their rarity and the lack of an effective treatment, prion diseases draw exceptional scientific interest, mainly because of their peculiar transmission mechanism, involving the presence of a misfolded isoform (PrP^{Sc}) of the cellular prion protein (PrP^{C}) and unique histological lesions. Sporadic Creutzfeldt-Jakob disease (sCJD), the most common human prion disease type, has a wide spectrum of clinical and histopathological phenotypic heterogeneity that has made its clinical recognition difficult. Four main neuropathological features of sCJD have been described: astrocytosis, associated with neuronal loss, intracellular spongiform degeneration, and PrP^{Sc} accumulation in extracellular space [Puoti

2012]. A great variability on lesion distribution, spongiform degeneration and PrPSc accumulation is influenced by the genotype at codon 129 and the PrPSc type [Gambetti 2003]. In particular, fine spongiosis with small vacuoles is characteristic of the most common phenotypes (MM1, MV1 and VV2), whereas coarse spongiosis with large vacuoles is found in the MM2C and MV2C subtypes [Parchi 2012]. For example, the vacuole average diameter in sCJD MM1 is 5.8 ± 1μm, while in sCJD MM2, a sCJD subtype which can be difficult to distinguish clinically from sCJD MM1, the average vacuole diameter is larger than 15 μm. The subtypes have quite different prognosis, so a non-invasive technique for the estimation of vacuole size would have a great importance. However, currently, definite diagnosis of sCJD and its subtypes can be made only by brain tissue examination. Clinical criteria for the diagnosis of probable sCJD require the presence of at least two clinical signs out of (i) dementia, (ii) cerebellar or visual, (iii) pyramidal or extrapyramidal, (iv) akinetic mutism, and at least one of three tests – 14-3-3 protein in CSF, periodic sharp-wave complexes in the EEG, or abnormally high signal on MRI – must be positive [Zerr 2009]. In particular, asymmetric hyperintensities on dMRI and T_2-weighted Fluid Attenuated Inversion Recovery (FLAIR) in at least three non-contiguous gyri or in the striatum or both is highly suggestive for the diagnosis of sCJD. Currently, dMRI is the best among standard MRI sequences [Young 2005, Kallenberg 2006, Galanaud 2010, Vitali 2011] with a diagnostic accuracy above 90% [Shiga 2004, Young 2005, Satoh 2007, Galanaud 2010, Vitali 2011]. A typical case of sCJD with signal hyperintensity in the cortical ribbon on dMRI and FLAIR is illustrated on Figure 2.1.

However, even though dMRI hyperintensity is currently used as a marker of prion disease [Puoti 2012], the tissue alteration underlying this imaging signal remains unknown. It has been reported that dMRI sensitivity may vary among prion diseases and sCJD subtypes [Krasnianski 2006], which opens the possibility to use it for early diagnosis of sCJD subtypes. Therefore, the identification of the histopathologic substrate associated with the

dMRI signal abnormality is important, because it can guide the precise choice of MRI protocol to maximise diagnostic power.
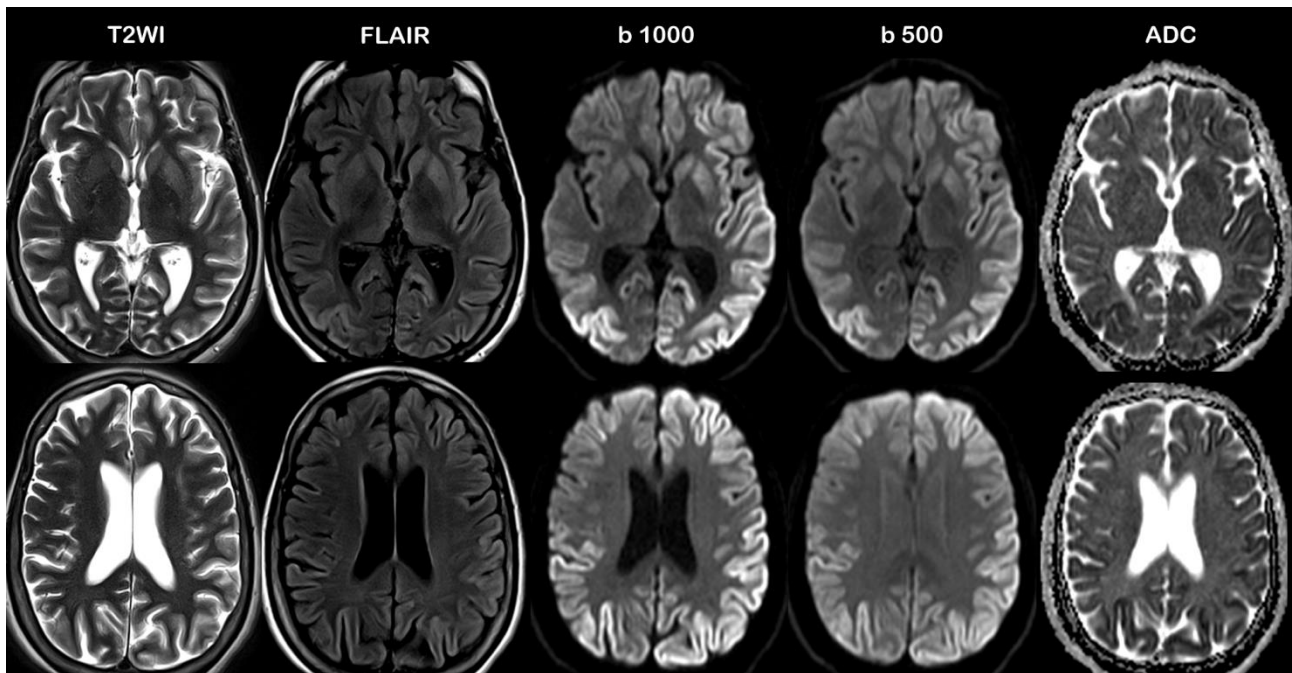
Figure 2.1. MRI signal alterations in a typical sCJD case. The signal abnormality is consistently more prominent in dMRI with b = 1000 (marked as b1000 in figure) than with b = 500 (b500), FLAIR and T_2-weighted MRI (T2WI) in this decreasing order. ADC maps show decreased diffusivity in the affected regions, but the signal alteration is less evident than in dMRI.

A few authors have looked for a correlation between neuropathological changes and dMRI hyperintensity or reduction in ADC. According to some groups [Geschwind 2009, Manners 2009], dMRI hyperintensities may be correlated with spongiosis and PrPSc deposition rather than with gliosis and neuronal loss; Lodi et al. [Lodi 2009] found that patients with fatal insomnia, a prionopathy associated with little or no spongiform changes [Parchi 1999], did not exhibit hyperintensities on dMRI thus pointing to spongiosis as the principal determinant of dMRI signal hyperintensity. On the other hand, Russmann et al. [Russmann 2005] found no significant correlation between ADC and the degree of spongiosis, gliosis or neuronal loss.

Previous MRI studies of prion disease have focused (qualitatively or semi-quantitatively) on the apparent hyperintensity on T_2-weighted FLAIR and dMRI, or quantitatively only on

the ADC [Demaerel 2003, Tschampa 2003, Lin 2006, Galanaud 2008, Hyare 2010a, Hyare 2010b]. Only a recent study [Caverzasi 2014] performed a slightly more sophisticated analysis, by evaluating the FA (which did not show significant differences between patients and controls) and characterizing the evolution of MD with the pathology progression, which revealed a non-linear trend.

In this study specific models for dMRI signal in sCJD were developed, based on two different hypotheses for the origin of dMRI hyperintensity, and the raw signal and the parameters estimated by the models in patients and healthy controls were analyzed. In both the models characterization of T_2 relaxation was included, too, because CJD patients show hyperintensities not only on dMRI but also on T_2-weighted images, so the pathological substrate of CJD likely affects T_2 values.

The acquisition scheme was designed to explore the available range of different diffusion-weightings (b-values), diffusion times and T_2-weightings as widely as possible. The scheme pushes the limits of acquisition times possible on human subjects, but provides a uniquely broad sampling of the possible space of measurements with which to evaluate the candidate models

The work has three main aims:

- to compare the raw dMRI signal in CJD lesions with different acquisition parameters (TE and b-value) in order to investigate through these parameters the dependence of the hyperintensity from the underlying T_2 and diffusion ranges; this may lead to the suggestion of an optimal operating point for a clinical sequence aimed at the detection of hyperintensity.

- to evaluate the MR parameters of each model in healthy subjects and patients in order to see which are informative about the presence of prion pathology and to understand if the proposed models can provide more information than the ADC; this

may lead to new clinical indices of prion pathology and for a better characterization of specific features of the affected tissue.

- to compare the models themselves in terms of fitting performance in order to see which hypothesis is more likely to explain the signal changes, aiming at a general understanding of the pathological mechanism responsible for the signal hyperintensity.

2.2. Materials and methods

2.2.1. Hypotheses for dMRI hyperintensity and mathematical models

As already mentioned, to investigate the origin of hyperintensity in CJD patients we developed a modeling approach based on two main hypotheses on the microstructural tissue alterations that may cause dMRI hyperintensity. Each hypothesis leads to a different family of mathematical models for how the dMRI signal varies with TE, b-value and diffusion time. Our two hypotheses are:

a) reduction of hindered diffusivity caused by prion PrP^{Sc} deposition, increasing the hindrance to water motions in the extracellular space (figure 2.2, top);

b) restriction of water diffusing within intracellular vacuoles (figure 2.2, bottom).

The key difference between the two hypotheses is that (b) implies restricted diffusion, whereas (a) does not. However, both the hypotheses imply a reduction of water diffusive motions compatible with the observed dMRI hyperintensity. The two families of models associated with these hypotheses are (a) biexponential models and (b) bi-compartment models with restricted diffusion in a spherical compartment and hindered diffusion in the other compartment (restricted diffusion model in the following).
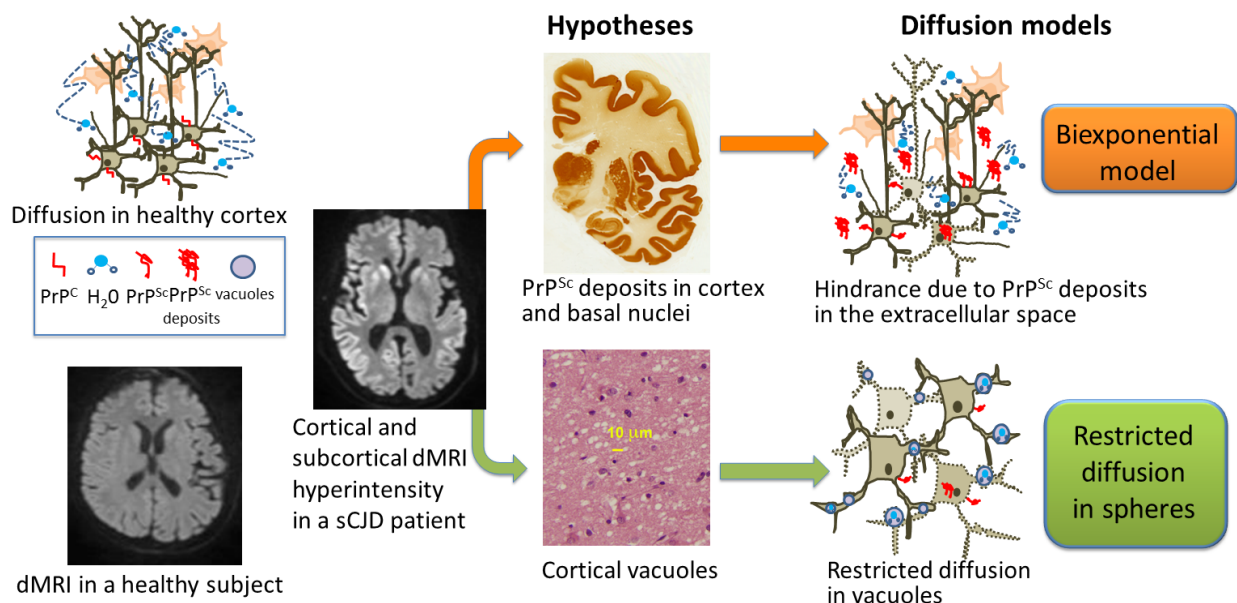
Figure 2.2. Illustration of the development of the mathematical models of diffusion in CJD patients based on the hypotheses on the neuropathological basis of dMRI hyperintensity. From left to right: schematic depiction of diffusion in healthy cortex and representative dMRI in a healthy subject; representative dMRI in a CJD patient showing cortical and subcortical hyperintensities; sections from neuropathology showing the alterations associated with our two hypotheses for dMRI hyperintensity (top: PrP^Sc immunohistochemistry showing PrP^Sc accumulation in the cortex as dark brown coloration; bottom: hematoxylin-eosin staining showing vacuolar degeneration); schematic depictions of pathological diffusion in the two hypotheses; corresponding mathematical models.

The general form of the biexponential model is:

$$S = M_0 \left[f \cdot e^{-\frac{TE}{T_{2,1}}} \cdot e^{-b \cdot d_1} + (1-f) e^{-\frac{TE}{T_{2,2}}} \cdot e^{-b \cdot d_2} \right] \qquad (2.1)$$

where the six free parameters are: M_0, which is a steady-state magnetization parameter; $T_{2,1}$ and $T_{2,2}$, the T$_2$ relaxation parameters for the two compartments; d_1 and d_2, the apparent diffusivities in the two compartments; and f, the volume fraction of the first compartment.

If PrP^Sc deposition only is responsible for dMRI hyperintensity as in hypothesis (a), we expect to find a reduction of diffusivity in at least one of the two compartments as the most

significant difference between patients and controls. If we can associate the two diffusivities with the intra and extracellular compartments, as [Clark 2000] suggests, then we expect to see the reduction in the extracellular compartment, which is normally that with the higher diffusivity.

The restricted diffusion model has two compartments, one with restricted diffusion in a spherical pore (the vacuole), and the other with isotropically hindered diffusion. Mathematically, the model in its most general form is:

$$S = M_0 \left[f \cdot e^{-\frac{TE}{T_{2R}}} \cdot Sph(b, TE, d_R, R) + (1-f)e^{-\frac{TE}{T_{2H}}} \cdot e^{-b \cdot d_H} \right] \qquad (2.2)$$

where $Sph(b, TE, d_R, R)$ is the expression for the signal from water restricted inside a sphere, which uses the GPD approximation, as in [Murday 1968], but adapted for the twice-refocused spin echo sequence as described in [Clayden 2009]. The Sph model has two free parameters: the radius R of the sphere and d_R, the intrinsic diffusivity inside the spherical compartment. The other free parameters of this model are M_0, as in the biexponential model, the T$_2$ values for the two compartments (T_{2R} and T_{2H}), the apparent diffusivity in the hindered compartment (d_H) and the volume fraction of the restricted compartment (f).

If dMRI hyperintensity is caused by restriction in the vacuoles as hypothesis (b) assumes, we expect to observe an increase of the fraction of the restricted compartment f in patients compared to healthy subjects.

We also considered a mono-exponential model:

$$S = M_0 e^{-\frac{TE}{T_2}} e^{-b \cdot ADC} \qquad (2.3)$$

with three free parameters: M_0, T_2 and ADC.

This is a simple standard model, which was included primarily to compare our results with literature, and to understand what information the more complex models can add.

As already mentioned in the introduction, all the proposed models characterize not only diffusion, but also the T_2 decay in each compartment. This choice is not usual in dMRI models and requires a more complex acquisition and fitting procedure, but was motivated by the qualitative knowledge that CJD patients show alterations on T_2-weighted MRI, so the investigation of T_2 relaxation parameters is particularly interesting in this case.

2.2.2. Constraints on the model parameters

We constrained the set of model parameters in the optimization using transformations that limit the range of each parameter to biophysically meaningful values. For all the models we constrained the T_2 values and the diffusivities to be positive and the volume fractions to be in [0, 1] and to sum to 1.

We simplified the general bi-exponential and restricted diffusion models, stated in equations (2.1) and (2.2) above, to reduce the number of parameters and stabilize the fitting and parameter estimation. Briefly:

- The b = 0 signal at various echo times shows no evidence of a biexponential trend, so we fix the two T_2 parameters to be equal in both models.
- The spherical compartment of the restricted diffusion model is insensitive to d_R, so we decided to fix d_R to the diffusivity of free water at body temperature ($3 \cdot 10^{-9}$ m^2/s) since vacuoles contain mostly water.

Thus the simplified biexponential model becomes:

$$S = M_0 \cdot e^{-\frac{T_E}{T_2}}[f \cdot e^{-b \cdot d_1} + (1-f)e^{-b \cdot d_2}] \tag{2.4}$$

with 5 free parameters: M_0, T_2, d_1, d_2 and f

Similarly, the simplified restricted-diffusion model becomes:

$$S = M_0 \cdot e^{-\frac{T_E}{T_2}}[f \cdot Sph(b, T_E, d_R, R) + (1-f)e^{-b \cdot d_H}] \tag{2.5}$$

also with 5 free parameters: M_0, T_2, d_H, R and f (with $d_R = 3 \cdot 10^{-9}$ m^2/s).

2.2.3. Patients and subjects

15 consecutive patients with suspected diagnosis of prion disease and four healthy age-matched elderly subjects were recruited. The study was approved by the local ethical committee and all individuals or their caregivers signed informed consent.

The diagnostic protocol included general clinical assessment, neurological evaluation, polygraphic EEG recording, analysis of the PRNP gene, cerebral MRI and blood laboratory tests, CSF analysis for the presence of 14-3-3 protein and the levels of total tau protein was performed in 11 patients.

Diagnosis of "probable" sCJD was made according to the current diagnostic criteria [Zerr 2009]. Lack of brain tissue examination impeded PrPSc type determination. However, one of six molecular subtypes (MM1, MV1, MM2, MV2, VV1 and VV2) was tentatively assigned to sCJD patients by three neurologists with expertise in prion disease using available clinical data.

Relevant clinical and laboratory data of the study population are reported in Table 2.1. Of the 15 patients enrolled in the study with suspected prion disease, nine were diagnosed as "probable" sCJD, one as familial CJD associated with the E200K PRNP mutation, two as GSS linked to the P102L PRNP mutation, and three as autoimmune encephalopathy. dMRI signal hyperintensity in the cerebral cortex and/or striatum was observed in all CJD patients, while no signal abnormalities were detected in the individuals with GSS or autoimmune encephalopathy.

Table 2.1. clinical data, MRI and laboratory tests results for the 15 patients and 4 healthy controls. The sCJD molecular subtype (MM1, MM2, MV1, MV2, VV2) was assigned to each patient according to the clinical data indicated in this table.

	CJD01	CJD02	CJD03	CJD04	CJD05	CJD06	CJD07	CJD08	CJD09	CJD10	GSS01	GSS02	RPE01	RPE02	RPE03	HC01	HC02	HC03	HC04
Clinical Diagnosis	familial CJD	sCJD	sCJD	sCJD	sCJD	sCJD	sCJD	sCJD	sCJD	sCJD	GSS	GSS	autoimmune encefalopathy	paraneoplastic encefalopathy	paraneoplastic encefalopathy	Normal	Normal	Normal	Normal
Predicted sCJD molecularsubtype	-	VV2	MV2	MM1	MM2	VV2	MV1	MV2	MV2	MV2	-	-	-	-	-	-	-	-	-
EEG	0	0	1	1	1	0	1	0	0	1	0	0	0	0	0	-	-	-	-
dMRI	1	1	1	1	1	1	1	1	1	1	0	0	0	0	0	0	0	0	0
Tau protein concentration (pg/mL)	ND	15432	6983	ND	2100	2062	2113	1648	617	2390	462	ND	267	637	-	-	-	-	-
14-3-3 protein detection	ND	positive	ambiguous	ND	positive	positive	positive	ambiguous	positive	positive	negative	ND	negative	ambiguous	-	-	-	-	-
PRNP codon 129	MV	VV	MV	MM	MM	VV	MV	MV	MV	MV	MM	MM	-	-	-	-	-	-	-
PRNP mutation	E200K	0	0	0	0	0	0	0	0	0	P102L	P102L	0	0	0	-	-	-	-
Clinical findings — Full stage — Mioclonus	1	0	0	1	0	1	1	0	0	1	0	0	0	0	0	0	0	0	0
Clinical findings — Full stage — Behavioural disorder	1	0	0	1	1	0	1	1	0	0	0	0	0	0	1	0	0	0	0
Clinical findings — Full stage — Pyramidal/ Extrapyr signs	0	0	1	1	0	1	1	1	0	1	0	0	0	0	0	0	0	0	0
Clinical findings — Full stage — Cerebellar /visual	1	1	1	0	0	1	1	0	1	0	1	1	0	1	0	0	0	0	0
Clinical findings — Full stage — Dementia	1	1	1	1	1	1	1	1	1	1	0	0	1	0	1	0	0	0	0
Clinical findings — Initial signs	cognitive deficits	cognitive deficits	ataxia	parkinsonism	cognitive deficits	ataxia	cognitive deficits	cognitive deficits	ataxia	cognitive deficits	ataxia	ataxia	cognitive deficits	ataxia	cognitive deficits	-	-	-	-
Disease duration at MRI (mos)	2	2	6	7	3	24	2	23	8	2	12	3	10	5	4	-	-	-	-
Total disease duration (mos)	14	5	7	8	29	24	3	38	17	16	45	33	NA	8	NA	-	-	-	-
Age at onset (years)	60	61	75	74	55	70	69	65	64	73	32	56	59	80	81	66	59	59	63
Sex	F	M	M	M	F	M	M	F	M	F	M	F	M	F	M	F	M	M	M
Patient code	CJD01	CJD02	CJD03	CJD04	CJD05	CJD06	CJD07	CJD08	CJD09	CJD10	GSS01	GSS02	RPE01	RPE02	RPE03	HC01	HC02	HC03	HC04

Abbreviations: 1 = positive; 0 = negative; NA = Not Applicable; ND = Not Determined

2.2.4. MRI acquisition

The study was performed on a 1.5T MR imaging unit (Siemens Avanto, Erlangen, Germany). The imaging protocol consisted of 264 diffusion-weighted volumes and 26 interleaved b = 0 volumes, using a twice-refocused [Reese 2003] single shot spin-echo echo-planar imaging (SS-SE EPI) sequence with four independent diffusion gradient directions, a TR of 7.2 s, nine values of TE in the range 68-107 ms and 13 b-values in the range 250-9000 s mm^{-2} (for each TE, all the b-values were used up to the maximum available for that TE, according to the scheme in Table 2.2, and the four gradient directions were oriented to take advantage of the maximum physical gradients strength); 45 slices were acquired, with a FOV of 220x220 mm^2 and an isotropic resolution of 2.3x2.3x2.3 mm^3. At each value of TE, the increasing b-values were achieved by increasing the gradient strength with the timings of the gradient pulses fixed, and thus the intrinsic timescale of the measurement.

Table 2.2. Acquisition protocol. The images are acquired with increasing TE values (shown in the first column), and increasing b-values (shown in the following columns) for

TE (ms)	b-values (s/mm^2)												
68	0	250	500	800	1000								
71	0	250	500	800	1000								
77	0	250	500	800	1000	1500							
81	0	250	500	800	1000	1500	2000						
89	0	250	500	800	1000	1500	2000	3000					
94	0	250	500	800	1000	1500	2000	3000	4000				
99	0	250	500	800	1000	1500	2000	3000	4000	5000			
103	0	250	500	800	1000	1500	2000	3000	4000	5000	6000		
107	0	250	500	800	1000	1500	2000	3000	4000	5000	6000	7000	8000	9000

However, as TE increased, the lengths of the gradient pulses increased, which provided measurements associated with longer diffusion times. Namely, the twice-refocused single-shot spin-echo (SS-SE) sequence does not specify an equivalent diffusion time;

nonetheless, a longer TE automatically determines longer diffusion gradients timing and diffusion times. The combination of measurements sensitive to different time scales and diffusion weightings enables estimation of pore sizes [Clayden 2009]. The range of pore diameters to which we have sensitivity, with the gradient strength available on the Avanto system, is approximately 5 to 20 μm [Clayden 2009, Dyrby 2013], which is typical of vacuole sizes in prionopathies [Kovacs 2008]. The choice of including multiple TEs has two main reasons: to allow a reliable fit of T_2 decay and to investigate the dependence of hyperintensity on TE in order to find an optimal operating point for clinically feasible lesion detection. As mentioned in the introduction, this protocol was explorative and not intended to be translated in clinics as it is.

2.2.5. Pre-processing and model fitting

Images were corrected for head motion and eddy current distortions using FLIRT (FMRIB's Linear Image Registration Tool, University of Oxford, U.K., [Jenkinson 2002]. An affine transformation with 12 degrees of freedom was calculated to register each b = 0 volume to the first one and then applied to transform the subsequent volumes into the same space. The quality of raw data and the performance of motion and eddy current correction were assessed by visual inspection of each acquired volume.

Regions of interest (ROIs) were manually drawn by an expert neuroradiologist in the following areas in the cortex and basal nuclei of each subject: hippocampus (Hip), inferior temporal gyrus (ITG), superior temporal gyrus (STG), caudate nucleus (Cau), anterior putamen (aPut), dorso-medial thalamus (DMTh), occipital cortex (Occ), inferior parietal lobule (IPL), superior parietal lobule (SPL), precuneus (PreCu), anterior middle frontal gyrus (aMFG), superior frontal gyrus (SFG), anterior cingulate cortex (ACC); each ROI was drawn in both hemispheres and on multiple slices, with particular care to avoid partial volume with WM or CSF. In sCJD patients each ROI was classified as affected or

unaffected according to the presence or absence of signal hyperintensity on dMRI and if affected the delineation was limited to the area of evident hyperintensity. The signal of each ROI was averaged over all voxels and slices included by the ROI.

The fitting procedure was similar to that in [Panagiotaki 2012]. Briefly, each model was fitted to the data using an iterative non-linear optimization procedure from multiple starting points to avoid local minima. Here a Levenberg–Marquardt algorithm [Marquardt 1963] was used for minimizing a chi-squared objective function with the Rician noise model [Sijbers 1999, Alexander 2008]. The objective function is the negative log-likelihood:

$$F = -log(L) = \sum_{n=1}^{M} \left[2log\sigma - logI_0 \left(\frac{S_n \tilde{S}_n}{\sigma^2} \right) + \frac{S_n^2 + \tilde{S}_n^2}{2} - logS_n \right] \qquad (2.6)$$

where L is the likelihood of the measurements given the model estimates, M is the number of measurements, σ is the standard deviation of the noise, $\tilde{S}_n$ is the n-th measurement, S_n is the model predicted signal and I_0 is the zero-order modified Bessel function of the first kind. For all models, the best fit parameters were chosen from the models after 100 perturbations of the starting parameters to ensure a reliable minimum. Measurements below a noise-floor threshold, selected from the estimated noise variance, were ignored during the fitting procedure.

The Bayesian Information Criterion (BIC, [Schwartz 1978]), proportional to the negative logarithm of the marginal likelihood of the observed data given the model, was used to compare the performance of the different models. It was computed in each ROI for each model as:

$$BIC = -2log(L) + k \cdot log(M) = 2F + k \cdot log(M) \qquad (2.7)$$

where L, M and F have the same meaning as in (2.6), while k is the number of model parameters. The BIC is particularly useful when comparing models with different complexity because it rewards the models that minimize the objective function, but it

simultaneously penalizes those with a high number of parameters, so it allows a trade-off between the desired fitting accuracy and the complexity needed to achieve it.

All the described procedures were implemented in MatLab (The Mathworks, Natick, MA, USA)

2.2.6. Statistical analysis

For each anatomical area, the 38 ROIs (two ROIs per subject, in the left and right hemisphere respectively) were divided in five groups: CJD+ (i.e. affected ROIs in CJD patients), CJD- (i.e. unaffected ROIs in CJD patients), HC (i. e. ROIs in healthy controls), RPE (i.e. ROIs in patients with RPE) and GSS (i.e. ROIs in patients with GSS).

Since in the biexponential model the two terms in (2) have the same expression, they are randomly associated with the "fast" component (higher diffusivity) and the "slow" one (lower diffusivity) respectively. After the fitting procedure, we renamed the higher value between d_1 and d_2 as d_F and the lower one as d_S in order to make them homogenous between subjects. Accordingly, we redefined f as the fraction of the fast component.

The mean raw signal for each combination of acquisition parameters was compared between CJD patients and controls, to understand which combination is most sensitive to the anomalies. The contrast-to-noise ratio (CNR) was calculated as:

$$CNR = \frac{m_+ - m_C}{\sigma_N} \tag{2.8}$$

where m_+ and m_C are the mean values of the raw signal averaged among all the hyperintensity regions and among all the control regions, respectively; σ_N is the standard deviation of noise (measured in a ROI outside the brain), averaged among all patients and controls. This measure was performed in order to understand whether the hyperintensity shown by each combination of the acquisition parameters may be masked by noise or is sufficiently high to be reliably detected.

The mean value and standard deviation of each estimated parameter were calculated in each group, and a one-tailed t-test was used to test significant contrasts between each of the pathological groups and the healthy controls, either considering the ensemble of group ROIs or separating specific anatomical areas.

2.3. Results

2.3.1. Analysis of the raw dMRI signal

The mean raw signal in the CJD+ regions was higher than in CJD- regions and in HC with all the considered combinations of b-value and TE (Figure 2.3, A); this increase was consistent across all the parameter combinations and significant in almost all of them.

The signal in CJD- regions was slightly higher than in controls, but the difference was never significant.

Since the human eye is sensitive to contrast rather than to absolute signal, the relative difference of the raw signal between each pair of groups was calculated as an index of contrast visible in dMRIs comparing pathological and normal tissue (Figure 2.3, B).

The contrast increased with b-value and TE reaching a peak with b = 3000 s/mm^2 and TE = 103 ms, then slightly decreasing for even higher b-values. The estimated CNR at the peak was about 5.5, which was sufficiently high to prove that the hyperintensity was not masked by noise. Almost the same trend was found for the contrast between CJD+ and CJD- signal, while the contrast between CJD- and HC was quite low and rather independent from the acquisition parameters.
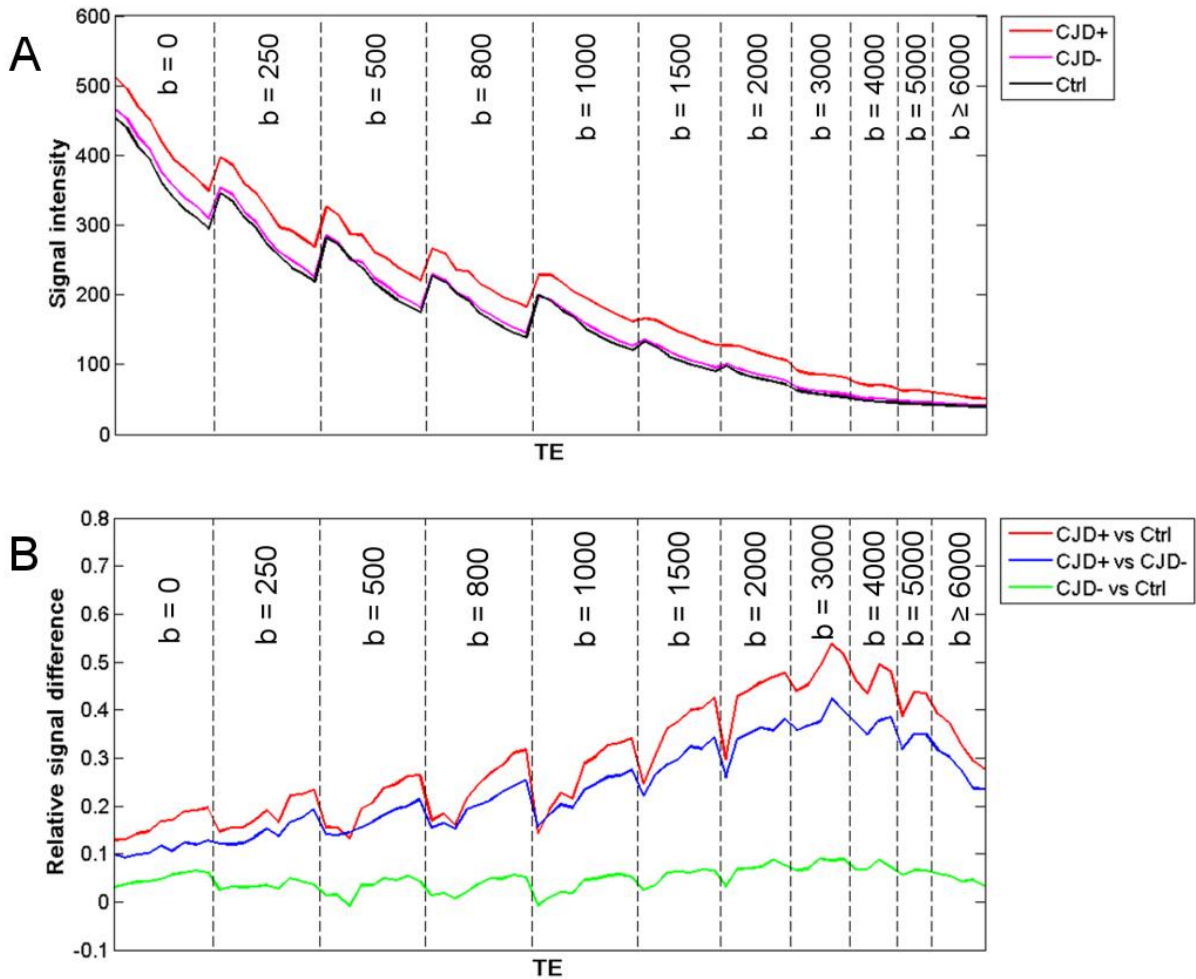
**Figure 2.3**. Raw dMRI signal in the different groups.
A) raw signal in the three main groups at each combination of the acquisition parameters.
B) relative difference between the mean signal in each pair of groups at each combination of the acquisition parameters.
In both the plots, for any b-value reported on the graph, the TE grows from left to right (see the TE values applied at each b-value in Table 2.2)

2.3.2. Fitting performance of the models

The quality of fit was good for the biexponential and restricted-diffusion models and the two models predict very similar signals, while the mono-exponential model predicts quite different signals at high b-values (figure 2.4).
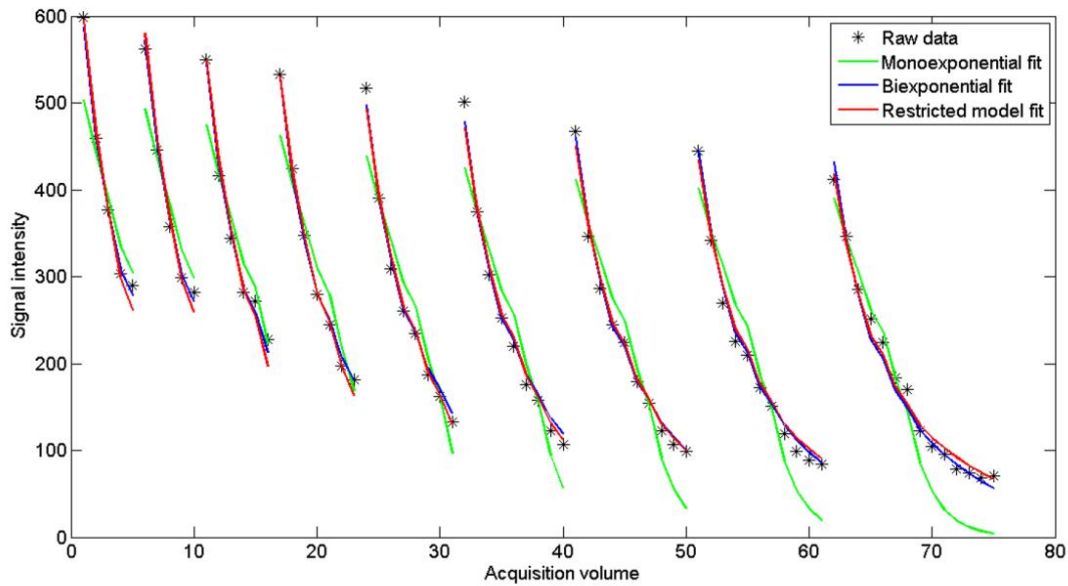
Figure 2.4. Visual assessment of the quality of fit in a representative ROI of a CJD patient. The raw signal (stars) and the signal predicted by each model (solid lines with different colors) are shown for every volume acquired. See Supplementary Table 1 for the acquisition parameters applied.

The BIC score was considered as a quantitative index of the fitting performance of the three models in each group of ROIs (Table 2.3). In the affected ROIs (CJD+) the biexponential and restricted-diffusion models performed significantly better than the mono-exponential model although they performed very similarly to each other (the difference was not significant).

Thus, although the fitting results did not show that either of the two hypotheses about the origin of the signal hyperintensity was better than the other, they did show that both the bi-compartment models provided a better fit to the data than the standard mono-exponential model and so should provide more sensitive and specific parameters. Also in the CJD- group and in controls no significant difference between the two bi-compartment models was found and BIC significantly decreased in both of them compared to the mono-exponential model, but this decrease was lower than in CJD+.

Table 2.3. Mean BIC values for each model in CJD+, CJD- and HC ROIs. Higher values are associated with worse fitting performances. Values marked with $^{(*)}$ are significantly lower than the mean BIC of the mono-exponential in the same group of ROIs, showing a better fitting performance of the bi-compartment models with respect to the traditional one.

BIC values	CJD+	CJD-	HC
Biexponential	2277 ± 141 $^{(*,\#)}$	2106 ± 156 $^{(*)}$	2022 ± 80 $^{(*)}$
Restricted	2287 ± 141 $^{(*,\#)}$	2116 ± 156 $^{(*)}$	2031 ± 86 $^{(*)}$
Mono-exponential	2633 ± 367 $^{(\#)}$	2305 ± 291 $^{(\#)}$	2143 ± 163

Values marked with $^{(\#)}$ are significantly higher than the mean BIC of the mono-exponential in the HC group, showing a worse fitting performance with respect to the normal case, probably due to pathologically changes not fully explained by the models.

It can be also noticed that the BIC was always significantly higher in the affected regions than in the healthy ones, thus suggesting that neither of the newly proposed models fully explains the MRI signal in affected areas; nonetheless, the increased difference between the mono-exponential and the bi-compartment models described above means that these models significantly improve the characterization of the pathological alterations.

2.3.3. Comparison of the estimated parameters between patients and controls

We first performed a statistical analysis between each group and the healthy subjects without separating the different anatomical areas. The results are shown in table 2.4 and will be described below for each group.

Table 2.4. Results of the group analysis.
Mean relative difference in each parameter between each group (CJD+, CJD-, RPE or GSS respectively) and the healthy controls. Not statistically significant differences are marked as "n.s."

		CJD+	CJD-	RPE	GSS
Biexponential	M_0	n.s.	n.s.	n.s.	n.s.
	T_2	+26%	+10%	n.s.	n.s.
	d_F	-14%	n.s.	n.s.	n.s.
	d_S	-37%	n.s.	-20%	n.s.
	f	+4%	n.s.	+9%	n.s.
Restricted	M_0	n.s.	n.s.	n.s.	n.s.
	T_2	+18%	+8%	n.s.	n.s.
	d_H	n.s.	+8%	+10%	n.s.
	f	+46%	+19%	n.s.	n.s.
Monoexp	M_0	-8%	n.s.	n.s.	n.s.
	T_2	+31%	+12%	+5%	n.s.
	ADC	-20%	n.s.	+5%	n.s.

In a second step we investigated the regional dependence of the parameters and we noticed a range of biophysical variability among different anatomical areas in the healthy subjects (table 2.5). For instance, the diffusivities were lower in Cau, aPut and DMTh than in the cortical areas, while T_2 was longer in the frontal cortex and shorter in aPut and DMTh. So we repeated the statistical analysis considering the anatomical regions separately.

Table 2.5. Mean value of each estimated parameter in each anatomical area in the healthy controls

HC	Biexponential					Restricted					Monoexp		
	M_0	T_2 (ms)	d_F ($\mu m^2/s$)	d_S ($\mu m^2/s$)	f	M_0	T_2 (ms)	d_H ($\mu m^2/s$)	R (μm)	f	M_0	T_2 (ms)	ADC ($\mu m^2/s$)
ACC	832±69	95±3	1510±227	236±63	0.622±0.062	822±67	95±3	1157±78	0.21±0.06	0.182±0.010	751±62	101±4	735±33
PreCu	1289±50	81±5	2150±307	358±76	0.496±0.067	1248±49	82±5	1232±34	0.83±1.72	0.171±0.013	1121±41	87±6	784±27
SFG	781±101	107±6	2070±298	364±74	0.501±0.062	766±97	108±6	1303±89	0.15±0.01	0.188±0.019	694±91	115±7	803±47
aMFG	803±104	106±9	2240±267	393±38	0.484±0.042	786±98	107±9	1354±93	0.15±0.02	0.187±0.014	712±91	114±11	833±35
STG	1031±85	82±6	2090±895	290±109	0.546±0.088	1018±87	82±6	1295±26	1.86±3.08	0.207±0.031	895±94	89±8	744±89
ITG	899±175	92±11	1720±455	263±136	0.576±0.130	884±169	92±11	1177±89	0.24±0.08	0.186±0.015	805±153	98±12	739±50
SPL	1495±87	86±3	2580±279	372±60	0.554±0.069	1460±88	87±3	1559±190	3.24±3.39	0.175±0.022	1265±75	95±4	955±75
IPL	1270±48	83±4	1930±283	341±58	0.531±0.053	1237±46	84±4	1212±90	0.21±0.03	0.164±0.010	1122±44	88±4	789±59
Occ	1236±104	77±5	1560±190	178±36	0.638±0.040	1250±139	76±7	1225±72	4.90±3.11	0.231±0.041	1065±90	83±6	689±34
Hip	895±61	93±4	1660±1043	109±143	0.732±0.146	908±61	91±5	1326±490	3.78±3.32	0.209±0.077	792±96	101±8	737±65
Cau	858±65	81±2	1040±134	51±62	0.763±0.054	859±62	80±2	992±84	1.46±2.27	0.200±0.025	791±60	84±3	623±28
aPut	879±31	73±2	1080±157	29±60	0.740±0.068	883±26	72±3	1035±77	2.64±2.19	0.239±0.030	795±29	76±2	584±33
DMTh	995±22	74±3	1240±248	62±94	0.732±0.085	993±22	74±3	1129±73	1.71±1.79	0.216±0.012	888±24	78±3	650±43

In the affected regions of CJD patients (CJD+ group) we found an increase of T_2, a decrease of diffusivities and an increase of the fraction of the restricted compartment with respect to controls (Table 2.4).

The percentage of difference of each estimated parameter in each region is specified in table 2.6, while figure 2.5 the regional dependence of the statistical significance of the differences in a selected subset of parameters.

Table 2.6. Relative difference of each estimated parameter in each anatomical area between the CJD+ group and the healthy controls.

CJD+ vs HC	Biexponential					Restricted				Monoexp			Nr of ROIs
	M_0	T_2	d_F	d_S	f	M_0	T_2	d_H	f	M_0	T_2	ADC	
ACC	-14% ***	+36% ***	17%	-9%	-6%	-13% **	+32% ***	4%	+27% **	-18% ***	+46% ***	-12% **	17
PreCu	-5% *	+19% ***	-24% ***	-52% ***	+23% ***	3%	+9% **	-4%	+89% ***	-9% ***	+25% ***	-21% ***	19
SFG	-15% *	+44% **	-21% **	-56% ***	+27% ***	-13% *	+37% **	0%	+24% *	-20% **	+61% **	-17% ***	8
aMFG	-16% **	+41% ***	-24% ***	-53% ***	+30% ***	-14% *	+36% ***	-3%	+18% **	-20% **	+54% ***	-15% ***	11
STG	+11% *	+23% ***	-23%	-45% **	9%	+18% ***	+13% **	3%	+53% ***	6%	+29% ***	-23% ***	13
ITG	+23% **	8%	-2%	-26%	3%	+29% **	2%	8%	+48% **	+15% *	+13% *	-14% **	13
SPL	-7%	+12% *	-34% ***	-52% ***	+14% **	3%	2%	-13%	+96% **	-8%	+15% *	-27% ***	10
IPL	7%	+17% ***	-3%	-34% **	+8% *	+14% **	+9% **	+13% *	+76% ***	0	+24% ***	-15% **	15
Occ	5%	31%	-7%	-38% ***	-5%	22%	12%	-57%	+158% *	-1%	40%	-29% *	3
Hip	-11% *	+22% **	-8%	-19%	-3%	-9% *	+16% ***	13%	33%	-15% *	+29% **	-15% *	9
Cau	-9% **	+31% ***	-1%	81%	-10% *	-9% **	+29% ***	-10% *	+14% *	-12% ***	+35% ***	-19% ***	17
aPut	-8% ***	+28% ***	-16% **	41%	-5%	-6% ***	+25% ***	-17% ***	+17% **	-10% ***	+30% ***	-26% ***	16
DMTh	-5% *	+23% ***	4%	28%	-9% *	1%	+15% ***	-1%	+58% ***	-12% ***	+29% ***	-22% ***	14

Statistically significant differences are marked according to the significance level: * p<0.05, ** p<0.01, *** p<0.001.

The main differences between CJD+ and HC are the following:

- T_2 was significantly increased in almost all the areas and in all three models (figure 2.5, B). Lengthening in T_2 relaxation time was greatest in the frontal cortex, while it was lower in the parietal and temporal areas. Minor differences were observed when comparing the different models.

- The proton density, M_0, was significantly increased in the temporal cortex and decreased in most of the other areas; some inconsistencies were observed among the three models, thus this parameter was not very informative.

- Diffusivities were generally reduced in all three models. In the biexponential model, d_F was significantly reduced in PreCu, SFG, aMFG, SPL and aPut (figure 2.5, C),

while d_S was reduced in PreCu, SFG, aMFG, STG, SPL IPL and Occ (figure 2.5, D); in most of the other areas d_F and d_S decreased, though not significantly. In the restricted-diffusion model, the differences in d_H were not significant in most anatomic regions. In the mono-exponential model, the *ADC* was significantly reduced in all the anatomical areas (Figure 2.5, E).

- Differences in the fraction of the "fast" component of the biexponential model varied with the anatomical position: the fraction was significantly increased in the frontal and parietal lobes and in PreCu, significantly decreased in Cau and DMTh.

- The fraction of the spherical compartment in the restricted-diffusion model was significantly increased in all the areas but Hip (Figure 2.5, F). The increase was particularly important (greater than 40%) in STG, ITG, SPL, IPL, PreCu and DMTh.

- For the radius of the spherical compartment we didn't perform a statistical analysis because isotropic restriction in the healthy controls is probably related to different conditions than in the CJD patients, so a comparison is not very meaningful. Moreover, in the Ctrl group the fraction of the spherical compartment is always quite low, and then the radius estimate may be uncertain. However, In all regions of the CJD+ the mean radius of the spherical compartment was in the range between 3 and 10 μm, compatible with the dimensions of vacuoles in CJD as measured by histopathology [Kovacs 2008], while in the control group the radii were generally much smaller (about 1.6 μm on average). Fig. 5a shows the mean radius estimated in each subject, averaged across all the considered ROIs.). When averaged across all the affected ROIs, the mean radius was larger (about 7 μm) in 2 patients (CJD08 and CJD10) compared to the other 8 patients (3-6 μm) (figure 2.6, A). Differences in size were observed also among anatomical areas: the radius was greater in SPL, PreCu, DMTh and Occ, while it was smaller in frontal regions (aMFG, SFG, and ACC) (figure 2.6, B).
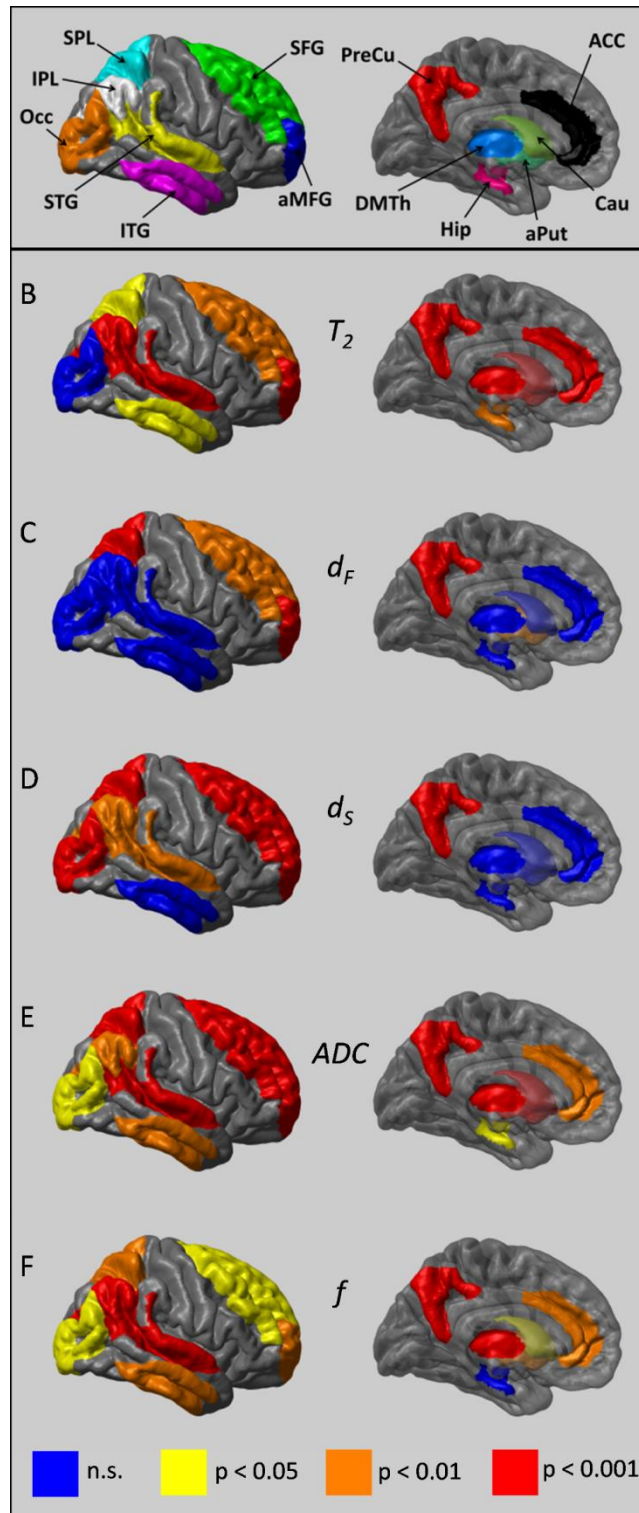
Figure 2.5. Lateral (left) and mesial (right) renderings of anatomical areas (A) and regional localization of statistical CJD+ to HC contrasts in the estimated parameters (B-F):
T_2 in the mono-exponential model (B); d_F (C) and d_S (D) in the biexponential model; *ADC* in the mono-exponential model (E); the volume fraction of the spherical restricted compartment in the restricted-diffusion model (F). In each panel the analysed areas without significant differences are in blue, while the areas with statistically significant differences are in yellow ($p < 0.05$), orange ($p < 0.01$) or red ($p < 0.001$)
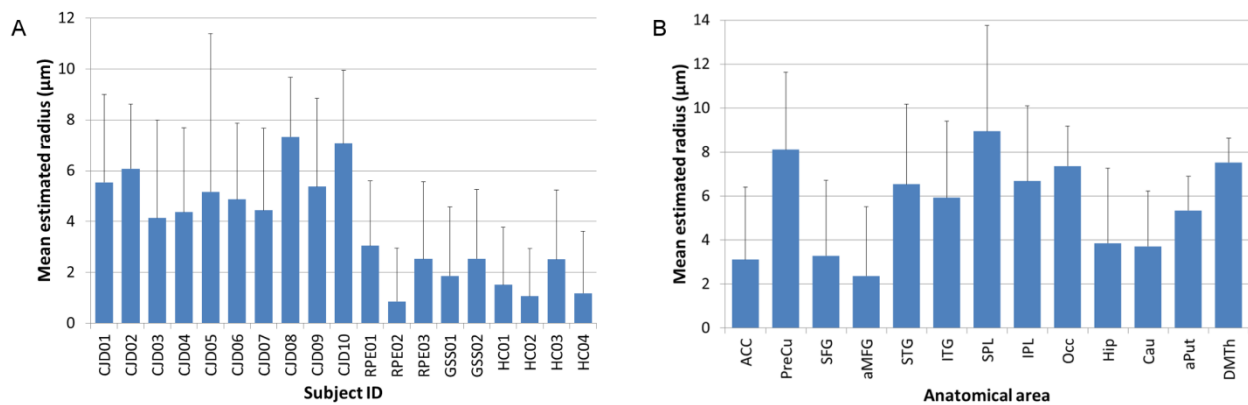
Figure 2.6. Estimated radius of the spherical compartment in the different subjects and areas.
A) Histogram showing the estimated radius averaged across all the ROIs in each subject.
B) Histogram showing the estimated radius averaged across all the CJD+ ROIs in each anatomical area

Comparing the CJD- group and the control group (tables 2.4 and 2.7), the relative alterations of T_2 and of the fraction of the restricted compartment were generally smaller and less statistically significant, but followed the trend of those reported above for the CJD+ group. The radius of the spherical compartment in CJD- was significantly larger than in healthy and pathological controls (p < 0.001) but smaller than in CJD+ regions (p < 0.001).

On the contrary in the CJD- group there was no significant change in diffusivity in the mono-exponential model (i.e. *ADC*), in the biexponential model (i.e. d_F and d_S) nor in the restricted-diffusion model (i.e. d_H). This result suggests that both models can explain the appearance of signal hyperintensity on dMRI either as a reduction of diffusivity (biexponential model) or as an increase of intra-vacuolar volume fraction (restricted model).

Table 2.7. Relative difference of each estimated parameter in each anatomical area between the CJD- group and the healthy controls.

CJD- vs HC	Biexponential					Restricted				Monoexp			Nr of ROIs
	M_0	T_2	d_F	d_S	f	M_0	T_2	d_H	f	M_0	T_2	ADC	
ACC^	-17% *	+22% ***	10%	-11%	0%	-17% **	+22% ***	1%	3%	-18% **	+24% ***	-2%	3
PreCu	11%	1%	11%	-8%	13%	15%	-2%	24%	25%	8%	3%	13%	1
SFG	-7%	+12% **	-6%	-27% *	+19% **	-7%	+12% **	5%	3%	-8%	+15% **	0%	12
aMFG	-12% *	+15% **	11%	-16%	11%	-12% *	+15% **	6%	5%	-14% **	+18% **	0%	9
STG	7%	-2%	-23%	-35% *	+17% *	8%	-3%	-5%	5%	7%	-2%	-3%	7
ITG	+18% *	-3%	-13%	-26%	7%	+20% *	-5%	-4%	+19% *	+14% *	-1%	-12%	7
SPL	-16% ***	0%	-19% *	-21% *	6%	-16% ***	1%	-13% *	2%	-14% **	4%	-13% **	10
IPL	1%	3%	+27% **	14%	-3%	0%	3%	+18% *	5%	-2%	10%	+12% *	5
Occ	+13% **	7%	+13% *	2%	0%	+23% ***	-1%	+24% *	+56% ***	+10% **	+15% *	5%	17
Hip	-11% **	+12% ***	21%	+111% *	-18% *	-12% ***	+13% ***	0%	5%	-13% *	+19% **	1%	11
Cau	-5% *	+15% *	29%	154%	-12%	-7% *	17%	7%	2%	-9% *	19%	0%	3
aPut	-7% **	+13% ***	9%	5%	-2%	-6% *	+12% ***	5%	9%	-10% **	+16% **	-7%	4
DMTh	3%	5%	1%	15%	-1%	+6% *	3%	3%	+17% *	2%	6%	-3%	6

Statistically significant differences are marked according to the significance level: * p<0.05, ** p<0.01, *** p<0.001.
^ In ACC no change is significant because there is just one sample in the CJD- group.

In the RPE group a slight increase of T_2 and diffusivities in comparison with healthy controls (tables 2.4 and 2.8) was observed, while in the GSS group just few sporadic anatomic reductions of M_0 and T_2 were found (tables 2.4 and 2.9).

The CJD+ group was also compared with the RPE and GSS groups and with a "generalized" control group including all the ROIs in non-CJD subjects (HC, RPE and GSS). In all three comparisons similar results as between CJD+ and healthy controls were found. These results demonstrated that increased T_2, decreased diffusivities and increased restricted volume fraction are the main changes in MR parameters associated with regions of dMRI signal hyperintensity.

Table 2.8. Relative difference of each estimated parameter in each anatomical area between the RPE group and the healthy controls.

RPE vs HC	Biexponential					Restricted				Monoexp		
	M_0	T_2	d_F	d_S	f	M_0	T_2	d_H	f	M_0	T_2	ADC
ACC	-11% **	+11% **	+31% *	19%	-8%	-12% **	+11% **	+18% **	+12% **	-14% **	+13% **	8%
PreCu	3%	3%	-6%	-24% *	+25% **	5%	1%	+18% *	9%	1%	4%	+12% *
SFG	-7%	+15% *	9%	-13%	19%	-6%	+15% *	+20% ***	1%	-8%	+18% *	+16% ***
aMFG	-11% *	5%	-13%	-33% *	+26% *	-11% *	5%	5%	4%	-11% *	5%	1%
STG	-2%	1%	-22%	-35%	+17% *	-2%	1%	-3%	-3%	-1%	0%	-1%
ITG	+25% *	-8%	2%	-9%	11%	+25% *	-8%	+11% *	-1%	+23% *	-7%	+9% *
SPL	-3%	-2%	-19% **	-21% **	+14% *	-1%	-2%	-2%	2%	-1%	-3%	-1%
IPL	+16% **	2%	-3%	-17%	+18% **	+17% **	1%	+10% **	-2%	+15% **	2%	+11% **
Occ	2%	3%	-2%	-15%	9%	2%	3%	5%	-9%	4%	3%	+10% **
Hip	-3%	+7% *	-15%	-16%	3%	-4%	+8% *	-3%	-10%	-3%	8%	5%
Cau	-4%	1%	+30% *	1%	-5%	-4%	0%	+30% *	+25% *	-10% *	4%	4%
aPut	-8% *	2%	18%	-78%	-2%	-7% *	2%	+23% *	+16% *	-13% *	5%	0%
DMTh	-4%	3%	-6%	-95%	6%	-2%	1%	4%	8%	-6%	4%	-5%

Table 2.9. Relative difference of each estimated parameter in each anatomical area between the GSS group and the healthy controls.

GSS vs HC	Biexponential					Restricted				Monoexp		
	M_0	T_2	d_F	d_S	f	M_0	T_2	d_H	f	M_0	T_2	ADC
ACC	-21% ***	4%	-21% **	-59% *	+20% **	-20% ***	3%	-5%	3%	-18% **	2%	-2%
PreCu	-3%	-5%	9%	12%	-10%	-3%	-5%	3%	5%	-3%	-5%	1%
SFG	-19% **	3%	-14%	-14%	11%	-18% **	3%	-1%	5%	-17% **	1%	0%
aMFG	-20% **	2%	-14%	-11%	8%	-19% **	2%	-7% *	2%	-17% **	0%	-4%
STG	9%	-5%	-16%	16%	-6%	9%	-5%	-11%	-14% *	+13% *	-8%	1%
ITG	+22% *	-14% *	+24% *	+51% *	-22% *	+21% *	-14% *	4%	-1%	+21% *	-15% *	5%
SPL	-4%	-9% ***	-15%	-23%	8%	1%	-12% ***	1%	+39% ***	-4%	-10% ***	-8% *
IPL	10%	-4%	-2%	-18%	11%	13%	-6% *	+11% **	27%	8%	-3%	2%
Occ	4%	-3%	2%	-5%	4%	4%	-3%	5%	-3%	5%	-3%	7%
Hip	-2%	-2%	-34%	-55%	8%	-3%	0%	-22%	-20%	3%	-5%	-6%
Cau	-10% **	2%	36%	250%	-19%	-11% **	3%	2%	-3%	-9% **	2%	5%
aPut	-18% **	+5% *	-1%	-100%	-1%	-17% **	+4% *	5%	20%	-18% **	+5% *	-5%
DMTh	3%	-4% *	30%	243%	-19%	2%	-4% *	1%	-3%	+3% *	-5% *	6%

Statistically significant differences are marked according to the significance level: * p<0.05, ** p<0.01, *** p<0.001.

2.4. Discussion

In this study mathematical models have been used to analyse differences in dMRI signal in patients with suspected prion disease and controls. Data were acquired with an advanced imaging protocol using many combinations of TE, diffusion weightings and times that allowed an in-depth analysis of the MRI signal abnormality. The results of the model-based analyses showed significantly longer T_2, lower diffusivity, or greater fraction of restricted diffusion in dMRI hyperintense areas. For the first time an estimate of the radius of the restricted compartment was provided, that in affected ROIs may be related to the presence and size of vacuoles.

A first inspection performed on raw dMRI signal showed a significantly higher signal in the CJD+ group with respect to healthy subjects, GSS and RPE, across the whole range of b-values. The absolute difference between the signal in CJD+ and controls in each ROI appears almost constant across different echo times and b-values. The relative difference in signal tends to increase with both b and TE, reaching a maximum at b = 3000 s/mm^2 and TE = 103 ms, which indicates an optimal operating point. Since the relative signal difference is closer to the contrast seen by human eye than the absolute signal. Our results are in agreement with previous studies [Hyare 2010a, Riva-Amarante 2011] which suggested use of high b-values (b = 3000) for a better contrast of CJD lesions.

In the second part of the study the dMRI signal was analysed with three mathematical models: biexponential, spherical restricted-diffusion and mono-exponential. This is the first study probing CJD with diffusion models more complex than the mono-exponential one. The two new bi-compartment models are derived from two hypotheses about the origin of the hyperintensity on dMRI and FLAIR MR images in CJD patients: a) the reduction of diffusivity in the extracellular space due to the deposition of prion protein (PrPSc) and b) the restriction of water trapped inside disease-related vacuoles. The aims of the model-

based analysis were (i) to evaluate the differences in the parameters of each model associated with CJD, and (ii) to compare the models themselves to understand the underlying neuropathological substrate. As for aim (i), the statistical analysis highlighted some consistent differences: in CJD patients the T_2 value is markedly increased in almost all hyperintense affected regions, the diffusivities are generally reduced in the mono- and biexponential models, and the fraction of the spherical compartment estimated by the restricted-diffusion model is increased. Although the ADC is the only parameter to show statistically significant differences in all the areas, this does not support the mono-exponential model. The biexponential and restricted-diffusion models also show statistically significant differences in all areas, though explaining them by means of different parameters. Furthermore, the models pin down the source of the statistical differences more precisely to particular parameters that are not the same in different anatomic regions.

The ADC numerical values found for CJD patients and controls in our study are compatible with those reported by previous works that have shown a reduction in ADC in CJD patients [Demaerel 2003, Tschampa 2003, Hyare 2010b]. For the other MR parameters there are no previous numerical results in the literature, but the quantitative results of the present work are in agreement with qualitative results reported in many clinical studies about the sensitivity of different MRI sequences to CJD.detection. In particular, according to our results both the T_2-weighted and the diffusion-weighted component of the signal are altered; thus confirming the common evidence that also FLAIR and T_2-weighted sequences can detect the pathology to some extent due to the alteration of T_2. Nonetheless, dMRI sequences are more sensitive because they include both T_2 and diffusion weightings. The increase of the T_2 relaxation time may be related to neuronal loss, resulting in a more homogeneous microenvironment due to reduction of microstructural components that cause surface relaxation. Conversely, the similar performance of the two

bi-comparment models leaves open the question about the micro-structural mechanisms underlying decreased MD, as discussed later on.

Focusing spherical restriction, this is the first study attempting to measure vacuolar average size. A significant increase in the radius of the spherical compartment was found in sCJD patients compared with normal and pathological controls, even though a direct comparison is not very meaningful because the source of isotropic restriction in controls, where vacuoles are absent, may be different to CJD patients (e.g., cell soma), requiring different hypotheses as to the ADC within the compartment. The estimated radius of the spherical restricted compartment in affected regions was compatible with the dimension of the vacuoles in CJD as measured by histopathology [Kovacs 2008]. This supports the association of the restricted portion of signal with the vacuoles, and that the radius of the sphere is an estimation of the average size of the vacuoles in the considered ROI or voxel. If confirmed on a larger group of patients with pathology proven sCJD subtype, these results might have implications for early in vivo diagnosis of sCJD subtype. Interesting differences in average vacuolar size among anatomical areas were also found; for example the estimated radius was smaller in the frontal lobes, cingulate, hippocampus and caudate, larger in the thalamus, parietal and occipital lobes. This variation may reflect genuine differences in vacuole size, although other factors, such as differences in vacuole membrane permeability, may also bias the estimate.

Interestingly, in the "unaffected regions" of CJD patients (CJD- group) an increase of T_2 and of the fraction of the spherical compartment in the restricted-diffusion model was found (although lower than in affected CJD+ regions), but no coherent changes in diffusivities were evident. These results suggest that perhaps the pathological alterations in regions without MR signal hyperintensity might be at subclinical stage.

Only minor differences in the estimated parameters were found in GSS and RPE patients with respect to healthy subjects; furthermore, almost the same differences resulted from

the comparison between the CJD+ group and each of the three control groups (healthy, GSS and RPE). GSS is a genetic form of prion disease characterized by accumulation of N- and C-terminal truncated fragments of PrP in form of amyloid plaques. Spongiform changes are usually absent or mild, except for a subgroup of patients with the P102L mutation showing a CJD-like phenotype. In patients with RPE the absence of MR signal abnormalities was an early clue to eventually rule out the diagnosis of sCJD.

Thus we can conclude that the above reported differences in T_2, diffusivity and vacuolar volume fraction are specific to CJD and unlikely related to unspecific neuronal degeneration.

With regards to the specific pathological mechanisms altering diffusion properties, addressed in aim (ii), it can be observed that both the bi-compartment models have a better fitting performance than the mono-exponential one, and the difference in BIC is much greater in the affected ROIs than in the healthy tissue, even though the BIC values themselves are higher. Small differences in BIC values for healthy subjects show only small benefits of the more complex models compared to the mono-exponential, while in CJD+ the advantages of the more complex models are much more significant. Although our models cannot capture all the signal abnormality (because the BIC is always higher in CJD+ than in control ROIs) they represent a step towards a better characterization of the affected tissue, and some interesting observations can be inferred by a detailed analysis of the results.

As to mechanisms underlying the decreased MD, since the biexponential and the restricted-diffusion models have similar fitting performances, a possible explanation is that both pathological features of CJD may determine the dMRI signal abnormality to some extent. In affected ROIs water diffusion might be both hindered with lower diffusivity likely caused by prion PrP^{Sc} deposition in the extracellular space (hypothesis a) and restricted in vacuoles with impermeable barriers (hypothesis b). In the biexponential model the

reduction of diffusivity occurs in both extra and intracellular compartments, which does not support hypothesis (a) directly, as this hypothesis implies a reduction only in the extra-cellular "fast" diffusion compartment, even though this observation does not refute hypothesis (a) because the assignment of components in the biexponential model to the intra and extracellular spaces is not strict [Clark 2000]. However, in the restricted-diffusion model the differences between CJD+ and controls are found primarily in the restricted compartment and the diffusivity in the hindered compartment is almost never significantly altered. This finding somewhat goes against the combined hypothesis. Perhaps the biological mechanism involved in CJD is even more complex than we initially anticipated with the two hypotheses. Permeability of the vacuole walls is one possible mechanism that our models did not consider. It would reduce observable restricted diffusion and produce signal profiles closer to the biexponential model, as we observe. Thus, a key area for further work is to study more sophisticated models, probably requiring more exotic measurements [Drobnjak 2010, Lasic 2011] that include this kind of effect. A better understanding of the hallmark dMRI features of CJD will have an impact in designing new MRI sequences and may improve detection of disease in prionopathies, especially in pre-symptomatic patients. It has to be noted that the long and complex acquisition protocol used here was not intended as practical to run routinely for clinical assessment, but rather to provide the best information with which to identify an appropriate model. In future studies, an economical imaging scheme, more practical for clinical assessment, could be found basing on these preliminary results, for example using the experiment design optimization algorithm in [Alexander 2008].

A few limitations of this study should be acknowledged. First of all, the clinical diagnosis was available for all the patients but not autopsy-proven results: so it was not possible to look for a correlation of MRI parameters with neuropathological results. Regarding the acquisition protocol, the twice-refocused SS-SE EPI dMRI sequence available on our

scanner has advantages from the point of view of image quality, but does not allow setting the diffusion time independently from the TE: a standard Stejskal-Tanner sequence could help obtaining clearer results on the dependence of the signal on the acquisition parameters. Finally, more sophisticated models could be investigated, as discussed above. However, this work can represent an important step forward to a better characterization of MRI abnormalities in prionopathies and to foster the development of more sensitive sequences for early diagnosis of sCJD. Furthermore, the explored model parameters displayed promising differentiations by the analysis of clinically feasible scans and, if validated by larger trials, could provide further diagnostic information.

Bibliography

Alexander DC. A general framework for experiment design in diffusion MRI and its application in measuring direct tissue-microstructure features. *Magn Reson Med*. 2008;60(2):439-448.

Caverzasi E, Henry RG, Vitali P, et al. Application of quantitative DTI metrics in sporadic CJD. *NeuroImage Clin*. 2014;4:426-435.

Clark CA, Le Bihan D. Water diffusion compartmentation and anisotropy at high b values in the human brain. *Magn Reson Med*. 2000;44(6):852-859.

Clayden JD, Nagy Z, Hall MG, Clark CA, Alexander DC. Active imaging with dual spin-echo diffusion MRI. *Inf Process Med Imaging*. 2009;21:264-275.

Demaerel P, Sciot R, Robberecht W, et al. Accuracy of diffusion-weighted MR imaging in the diagnosis of sporadic Creutzfeldt-Jakob disease. *J Neurol*. 2003;250(2):222-225.

Drobnjak I, Siow B, Alexander DC. Optimizing gradient waveforms for microstructure sensitivity in diffusion-weighted MR. *J Magn Reson*. 2010;206(1):41-51.

Dyrby TB, Søgaard L V, Hall MG, Ptito M, Alexander DC. Contrast and stability of the axon diameter index from microstructure imaging with diffusion MRI. *Magn Reson Med*. 2012;70(3):711-721.

Figini M, Alexander DC, Redaelli V, et al. Mathematical models for Magnetic Resonance signal abnormality in patients with prion diseases. *NeuroImage Clin*. 2014. *(submitted)*

Galanaud D, Dormont D, Haïk S, Chiras J, Brandel JP, Ranjeva JP. Differences of apparent diffusion coefficient values in patients with Creutzfeldt-Jakob disease according to the codon 129 genotype. *Am J Neuroradiol*. 2008;29(7):E57.

Galanaud D, Haik S, Linguraru MG, et al. Combined diffusion imaging and MR spectroscopy in the diagnosis of human prion diseases. *Am J Neuroradiol*. 2010;31(7):1311-1318.

Gambetti P, Kong Q, Zou W, Parchi P, Chen SG. Sporadic and familial CJD : classification and characterisation. *Brit Med Bull*. 2003;66:213-239.

Geschwind MD, Potter CA, Sattavat M, et al. Correlating DWI MRI With Pathologic and Other Features of Jakob-Creutzfeldt Disease. *Alz Dis Assoc Dis*. 2009;23(1):82-87.

Hyare H, Thornton J, Stevens J, et al. High-b-value diffusion MR imaging and basal nuclei apparent diffusion coefficient measurements in variant and sporadic Creutzfeldt-Jakob disease. *Am J Neuroradiol*. 2010;31(3):521-526.

Hyare H, Wroe S, Siddique D, et al. Brain-water diffusion coefficients reflect the severity of inherited prion disease. *Neurology*. 2010;74(8):658-665.

Jenkinson M, Bannister P, Brady M, Smith S. Improved Optimization for the Robust and Accurate Linear Registration and Motion Correction of Brain Images. *Neuroimage*. 2002;17(2):825-841.

Kallenberg K, Schulz-Schaeffer WJ, Jastrow U, et al. Creutzfeldt-Jakob disease: comparative analysis of MR imaging sequences. *Am J Neuroradiol*. 2006;27(7):1459-1462.

Kovacs GG, Budka H. Prion diseases: from protein to cell pathology. *Am J Pathol*. 2008;172(3):555-565.

Krasnianski A, Meissner B, Schulz-Schaeffer W, et al. Clinical features and diagnosis of the MM2 cortical subtype of sporadic Creutzfeldt-Jakob disease. *Arch Neurol*. 2006;63(6):876-880.

Lasič S, Nilsson M, Lätt J, Ståhlberg F, Topgaard D. Apparent exchange rate mapping with diffusion MRI. *Magn Reson Med*. 2011;66(2):356-365.

Lin Y-R, Young GS, Chen N-K, Dillon WP, Wong S. Creutzfeldt-jakob disease involvement of rolandic cortex: a quantitative apparent diffusion coefficient evaluation. *Am J Neuroradiol*. 2006;27(8):1755-1759.

Lodi R, Parchi P, Tonon C, et al. Magnetic resonance diagnostic markers in clinically sporadic prion disease: a combined brain magnetic resonance imaging and spectroscopy study. *Brain*. 2009;132(Pt 10):2669-2679.

Manners DN, Parchi P, Tonon C, et al. Pathologic correlates of diffusion MRI changes in Creutzfeldt-Jakob disease. *Neurology*. 2009;72(16):1425-1431.

Marquardt DW. An Algorithm for Least-Squares Estimation of Nonlinear Parameters. *J Soc Indust Appl Math*. 1963;11(2):431-441.

Murday JS, Cotts RM. Self-Diffusion Coefficient of Liquid Lithium. *J Chem Phys*. 1968;48(11):4938-4945.

Panagiotaki E, Schneider T, Siow B, Hall MG, Lythgoe MF, Alexander DC. Compartment models of the diffusion MR signal in brain white matter: a taxonomy and comparison. *Neuroimage*. 2012;59(3):2241-2254.

Parchi P, Capellari S, Chin S, et al. A subtype of sporadic prion disease mimicking fatal familial insomnia. *Neurol* . 1999;52(9):1757.

Parchi P, de Boni L, Saverioni D, et al. Consensus classification of human prion disease histotypes allows reliable identification of molecular subtypes: an inter-rater study among surveillance centres in Europe and USA. *Acta Neuropathol*. 2012;124(4):517—529.

Puoti G, Bizzi A, Forloni G, Safar JG, Tagliavini F, Gambetti P. Sporadic human prion diseases: molecular insights and diagnosis. *Lancet Neurol*. 2012;11(7):618-628.

Reese TG, Heid O, Weisskoff RM, Wedeen VJ. Reduction of eddy-current-induced distortion in diffusion MRI using a twice-refocused spin echo. *Magn Reson Med*. 2003;49(1):177-182.

Riva-Amarante E, Jiménez-Huete A, Toledano R, et al. Usefulness of high b-value diffusion-weighted MRI in the diagnosis of Creutzfeldt-Jakob disease. *Neurología*. 2011;26(6):331-336.

Russmann H, Vingerhoets F, Miklossy J, et al. Sporadic Creutzfeldt-Jakob disease: a comparison of pathological findings and diffusion weighted imaging. *J Neurol*. 2005;252(3):338-342.

Satoh K, Shirabe S, Tsujino A, et al. Total tau protein in cerebrospinal fluid and diffusion-weighted MRI as an early diagnostic marker for Creutzfeldt-Jakob disease. *Dement Geriatr Cogn Disord*. 2007;24(3):207-212.

Schwarz G. Estimating the Dimension of a Model. *Ann Stat*. 1978;6(2):461-464.

Shiga Y, Miyazawa K, Sato S, et al. Diffusion-weighted MRI abnormalities as an early diagnostic marker for Creutzfeldt-Jakob disease. *Neurology*. 2004;63(3):443-449.

Sijbers J, den Dekker AJ, Raman E, Van Dyck D. Parameter estimation from magnitude MR images. *Int J Imag Syst Tech*. 1999;10(2):109-114.

Tschampa HJ, Mürtz P, Flacke S, Paus S, Schild HH, Urbach H. Thalamic involvement in sporadic Creutzfeldt-Jakob disease: a diffusion-weighted MR imaging study. *Am J Neuroradiol*. 2003;24(5):908-915.

Vitali P, Maccagnano E, Caverzasi E, et al. Diffusion-weighted MRI hyperintensity patterns differentiate CJD from other rapid dementias. *Neurology*. 2011;76(20):1711-1719.

Young GS, Geschwind MD, Fischbein NJ, et al. Diffusion-weighted and fluid-attenuated inversion recovery imaging in Creutzfeldt-Jakob disease: high sensitivity and specificity for diagnosis. *Am J Neuroradiol*. 2005;26(6):1551-1562.

Zerr I, Kallenberg K, Summers DM, et al. Updated clinical diagnostic criteria for sporadic Creutzfeldt-Jakob disease. *Brain*. 2009;132(10):2659-2668.

3. MICROSTRUCTURAL FEATURES OF BRAIN TUMORS BY NODDI

What is required of a working hypothesis

is a fine capacity for discrimination.

Jean-Francois Lyotard

This chapter addresses the study of tumoral and peritumoral areas, where DTI provides poor information while multi-compartmental models can improve the microstructural characterization.

Compared to the previous chapter addressing only GM, this study considers anisotropic models and increased angular resolution because WM areas were often involved. Hence, the need for reduced complexity inherent in clinical studies suggests limiting the geometrical detail. A good compromise was represented by the NODDI scan protocol and model, which simplify neurites to sticks, though leaving space to direction uncertainty by the ODI parameter. The applicability of NODDI in cases of isotropic restriction, expected in some tumors, was preliminary assessed by the comparison with a multi-compartment isotropic diffusion model.

The study was carried out through a cooperation among the Humanitas Research Hospital, the University College of London and the Politecnico di Milano.

3.1. Introduction: Glioma characterization and MRI

Gliomas are the most common tumors of the central nervous system. They arise from glial cells, which support and protect neurons in the brain, and are named according to the type of cells they likely originate from, basing on their histological features: astrocytomas from astrocytes, oligodendrogliomas from oligodendrocytes, ependymomas from ependymal cells, mixed gliomas containing cells from different types of glia (for example oligoastrocytomas from oligodendrocytes and astrocytes). In particular, glioblastoma multiforme (GBM), a malignant astrocytoma, is the most common brain glioma and has the worst prognosis.

The accurate classification of gliomas is fundamental for the modern clinical practice of neuro-oncology, because it allows predicting the biological behavior of the tumor and its response to therapy, providing a basis for planning chemotherapy, radiotherapy or surgery. In particular, the most widely used classification system for gliomas is the histology-based grading defined by the World Health Organization (WHO), which associates each type of glioma to a malignancy scale from I to IV [Louis 2007].

Grade I gliomas have low proliferative potential and are generally cured by surgical resection alone.

Grade II gliomas are generally infiltrative in nature and, despite low proliferative activity, often recur. Some type II tumors tend to progress to higher grades of malignancy, for example low-grade diffuse astrocytomas may transform to anaplastic astrocytoma or GBM.

Grade III gliomas have histological evidence of malignancy, including nuclear atypia and mitosis. Patients with grade III tumors usually receive adjuvant radio- and/or chemotherapy.

Grade IV gliomas are cytologically malignant, mitotically active, necrosis-prone tumors typically associated with rapid pre- and postoperative disease evolution and a fatal

outcome. Examples of grade IV neoplasms include GBM, most embryonal neoplasms and many sarcomas.

The determination of tumor grade is based on histology, and biopsy remains the gold standard, but it has some limitations: it is invasive, operator-dependent and has an inherent sampling error due to the small number of biopsy samples. Thus, the characterization of brain gliomas by neuroimaging would be very important, and MRI is one of the best candidates for this task because its non-invasiveness and multiparametric nature. Indeed, a qualitative differentiation between low-grade gliomas (LGG) and high-grade gliomas (HGG) can be obtained by the visual inspection of morphological, contrast-enhanced, diffusion-weighted and perfusion-weighted MRI and of the derived maps.

LGG are usually homogeneous on morphological MRI, with hyperintensity on T_2-weighted images, no signal abnormality on contrast-enhanced, diffusion- or perfusion-weighted MRI. ADC is usually high, FA is usually low (figure 3.1). Peritumoral edema is uncommon.

Grade III gliomas are usually hyperintense on T_2-weighted images and may present peritumoral edema. They usually have areas of contrast-enhancement and elevated relative cerebral blood volume (rCBV, estimated by perfusion-weighted MRI) and may show areas of increased dMRI signal and low ADC.

Grade IV gliomas are usually heterogeneous, with ring-shaped areas of contrast-enhancement, peritumoral edema and necrotic or cystic areas. dMRI signal is usually heterogeneous, rCBV is high (figure 3.2).

This qualitative differentiation of brain gliomas is user-dependent and not very accurate: for example, contrast-enhancement may be absent in a non-negligible percentage of malignant lesions [Scott 2002].
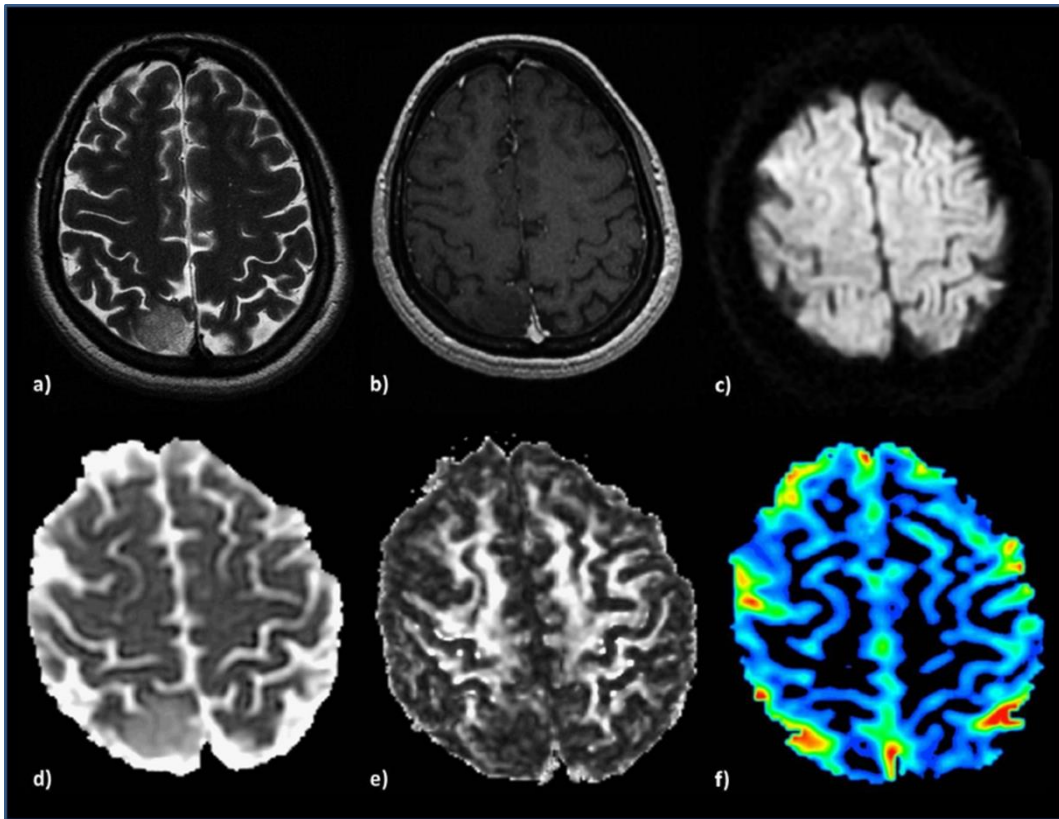
Figure 3.1. MRI images of a typical LGG: a) T_2-weighted, b) contrast-enhanced, c) dMRI, d) ADC map, e) FA map, f) rCBV map. Reproduced from [Svolos 2014]
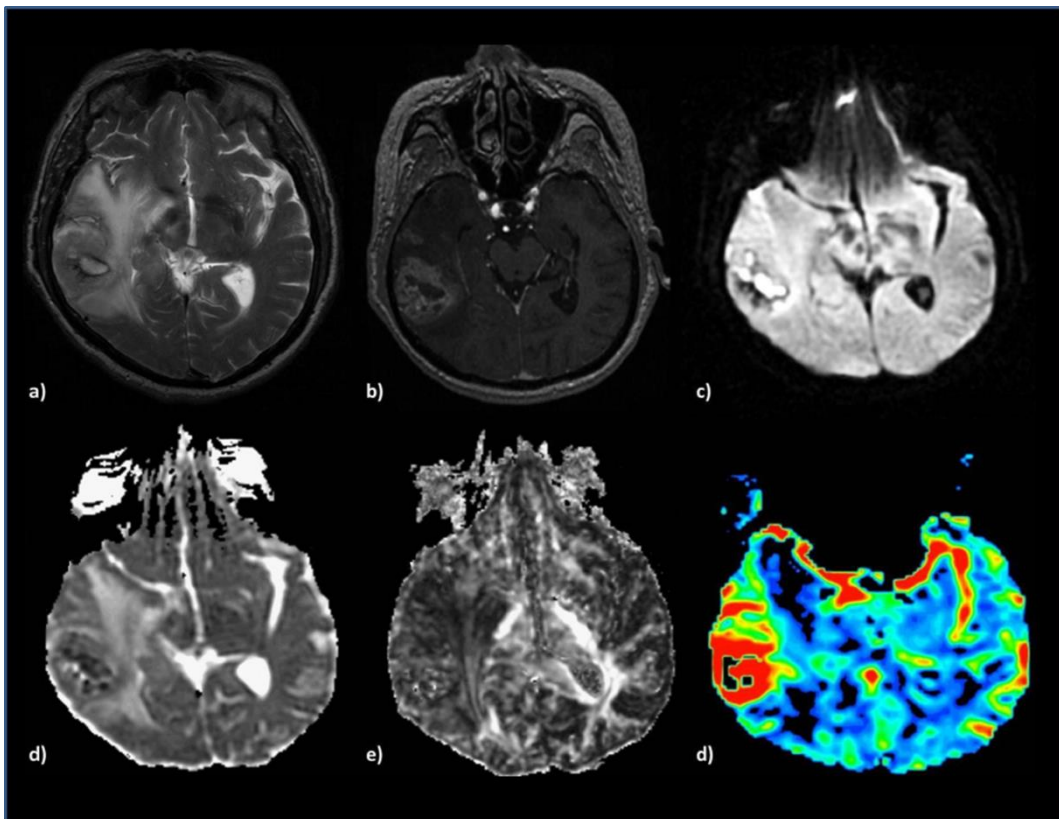
Figure 3.2. MRI images of a typical GBM: a) T_2-weighted, b) contrast-enhanced, c) dMRI, d) ADC map, e) FA map, f) rCBV map. Reproduced from [Svolos 2014]

Thus, the quantitative characterization of brain gliomas by advanced techniques as dMRI and perfusion MRI has been investigated by many research groups, because these techniques have the potential to provide more specific data about lesions [Svolos 2014]. In particular, the application of dMRI is interesting, because it conveys information about microstructure, even though the results have to be considered carefully.

Many studies succeeded in differentiating LGG and HGG by evaluating the intratumoral ADC or MD [Sugahara 1999, Kono 2001, Inoue 2005, Lee 2008, Kang 2011, Liu 2011, Server 2014]. In particular, these studies found higher intratumoral diffusivity in LGG than in HGG.

This result was associated to higher cellularity in HGG, which is intuitive since a higher density of cells causes higher hindrance of water molecules in the tissue and then reduces the apparent diffusivity. Indeed, an inverse correlation between ADC and cellularity in brain tumor (figure 3.3) was demonstrated by several works [Chenevert 1997, Sugahara 1999, Gauvain 2001, Kono 2001, Guo 2002].
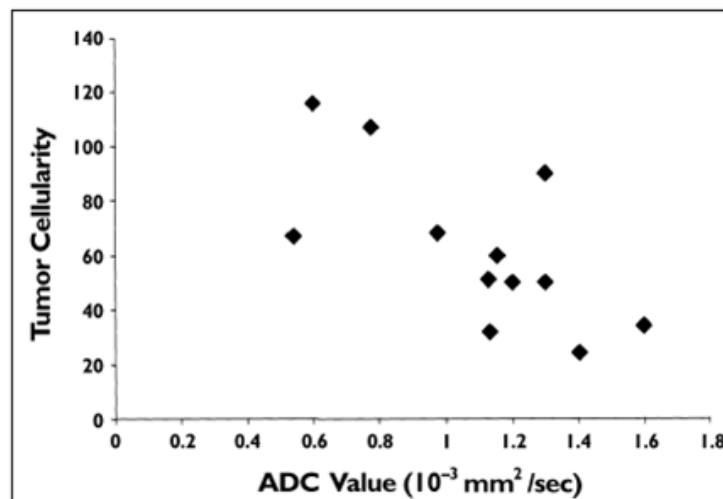
Figure 3.3. Correlation between ADC and tumor cellularity. Reproduced from [Gauvain 2001]

However, a recent study [Rahm 2014] highlighted a bad colocalization between areas with low ADC and areas with abnormally high metabolic activity, detected by Positron Emission Tomography with the amino acid O-(2-^{18}F-fluorethyl)-L-tyrosine. According to the authors,

this implies that ADC is not directly correlated with tumor cell density, but may be influenced by many factors (non-tumor cell density, alteration of water distribution).

A few works considered also differences in FA. Some of them found no significant differences between HGG and LGG [Lee 2008, Server 2014], while according to others FA can distinguish them, even more accurately than ADC or rCBV [Liu 2011], but with contradictory results: some studies obtained a higher FA in HGG [Beppu 2003, Inoue 2005], others found the opposite [Stadbauer 2006].

This survey of studies attempting glioma grading by dMRI demonstrates a great interest in this research field and a good potential of this technique, but also important limitations. A higher standardization of acquisition and analysis protocols would probably reduce the variability of results, but the application of standard dMRI methods likely limits the specificity of the mentioned studies.

The purpose of this work is to investigate the usefulness of an advanced multi-compartment dMRI model, NODDI ([Zhang 2012], paragraph 1.5.7) in the microstructural characterization of brain gliomas. NODDI parameters are expected to provide complementary and more specific information on glioma microstructure than standard dMRI parameters such as MD (or ADC) and FA. Different types of lesion will be analyzed and the possibility to differentiate gliomas of different grades and to characterize their microstructural features will be assessed.

3.2. Materials and methods

3.2.1. MRI acquisition and neuropathology

MRI data from 71 patients with histologically confirmed diagnosis of brain glioma were acquired on a 3T MRI scanner (Siemens Verio, Erlangen Germany). A dMRI protocol was

acquired with the following parameters: TE = 96 ms, TR = 15 s, 8 b = 0 volumes and 60 diffusion-weighted ones in 2 shells (b-values: 700 and 2000 s/mm^2) with 20 and 40 diffusion gradient directions, respectively. 64 axial slices were acquired, with a FOV of 256 x 256 mm^2 and an isotropic resolution of 2 x 2 x 2 mm^3. This acquisition protocol was chosen basing on the evaluation of accuracy and precision of NODDI parameters estimation by different protocols performed in [Zhang 2012], on the resulting recommendations for clinical studies, on the hardware features of the available scanner and on the acquisition time allowed on brain tumor patients.A T$_2$-weighted Turbo Spin Echo sequence was acquired for anatomical reference with the following parameters: TE = 106 ms, TR = 5420 ms, flip-angle = 150°, NA = 2. 40 slices were acquired, with a FOV of 512 x 512 mm^2, an in-plane resolution of 0.47x0.47 mm^2 and a slice thickness of 3 mm. A T$_1$-weighted MPRAGE sequence was acquired after injection of a gadolinium-based contrast agent, with the following parameters: TE = 2.73 ms, TR = 1800 ms, TI = 900 ms, flip-angle = 9°, NA=1. 176 slices were acquired, with a FOV of 448 x 512 mm^2, an in-plane resolution of 0.45 x 0.45 mm^2 and a slice thickness of 0.9 mm.

All patients had surgery and neuropathological diagnosis; in particular, the tumor grade was determined.

3.2.2. Pre-processing and model fitting

The dMRI images were corrected for motion and distortions using FSL's FLIRT [Jenkinson 2002] and the quality of realignment was assessed by visual inspection. The brain area was extracted using the semi-automatic Region Competition Snakes algorithm in ITK-SNAP [Yushkevich 2006].

The diffusion tensor in each voxel was estimated with Diffusion Toolkit [Wang 2007] using the whole data set, and FA and MD maps were derived.

The NODDI model was fitted to the data using the NODDI Matlab Toolbox [http://www.nitrc.org/projects/noddi_toolbox], which uses a three-stage fitting procedure, with an initial grid search, a gradient descent and a Markov Chain Monte Carlo, each finding the optimal starting point for the following step, as described in [Alexander 2010]. The following parameters were estimated: the principal direction of the intracellular compartment, the orientation dispersion index (ODI), the volume fraction of the CSF (f_{ISO}) and the relative volume fraction of the intracellular compartment (f_{IC}), as defined in equations (1.29) and (1.26).

The original formulation of NODDI in equation (1.29) defines f_{IC} as the intracellular volume fraction relative to the non-CSF tissue, but in some applications it may be more useful to have an estimate of the intracellular volume fraction with respect to the whole voxel. In this study the volume fractions of the intracellular (f_{ICV}) and extracellular space (f_{ECV}) were defined as follows:

$$f_{ICV} = (1 - f_{ISO})f_{IC} \tag{3.1}$$

$$f_{ECV} = (1 - f_{ISO})(1 - f_{IC}) \tag{3.2}$$

so that $f_{ICV} + f_{ECV} + f_{ISO} = 1$.

A primary aim of this work is the characterization of areas of high cellularity in gliomas, which are presumably associated to low MD or high restriction, and high dMRI signal, here evaluated as hyperintensity in the trace-weighted map, i.e. the map of $S_0\exp(-b \cdot tr(\boldsymbol{D}))$, where S_0 is the b = 0 signal and $tr(\boldsymbol{D}) = D_{xx} + D_{yy} + D_{zz} = \lambda_1 + \lambda_2 + \lambda_3 = 3 \cdot MD$.

NODDI was developed to model WM and does not explicitly account for isotropic restriction, expected in highly cellular lesions, thus it could not be very appropriate for identifying and characterizing them. However, it can be expected that in those regions NODDI would found still high intracellular volume fractions (f_{ICV}), but associated to high orientational dispersions (ODI); moreover, the need to keep the model simple and to

evaluate anisotropic restriction in the peritumoral and healthy WM motivated the choice of the "standard version" of NODDI to analyze the dMRI data.

Nevertheless, to test the performance of NODDI and the validity of the estimated parameters in tumor areas with high cellular density, the images from a subset of 20 patients were analyzed with a simple diffusion model including compartments with restricted, hindered and free diffusion. It was designed as the "isotropic equivalent" of NODDI and has the following mathematical form:

$$E = f_R + f_H exp(-b \cdot D) + f_F exp(-b \cdot D_F) \tag{3.3}$$

where f_R, f_H and f_F are the volume fractions of the restricted, hindered and free diffusion compartments, respectively. Water in the restricted compartment was modeled as stationary, as in the MMWMD ([Alexander 2010], paragraph 1.5.6), i.e. it is supposed not to move at all in any direction because it is "trapped" in tissue areas with very high cellular density. Thus, no diffusive motion happens in this compartment and the associated signal is not attenuated by diffusion. Water in the hindered and free diffusion compartments is modeled with Gaussian isotropic diffusion, with diffusivities D and D_F, respectively. D_F was fixed to $3 \cdot 10^{-3}$ mm^2/s, which is a typical value for diffusivity in the CSF.

Since the volume fractions are constrained to sum to 1 ($f_R + f_H + f_F = 1$), the model has three free parameters: f_R, f_F and D.

The same fitting procedure described in paragraph 2.2.5 was used here. For both NODDI and the isotropic diffusion model, the log-likelihood (equation (2.6)) was used as an objective function, and the BIC (equation (2.7)) was calculated to evaluate the fitting performance.

3.2.3. Statistical analysis

Multiple Regions of interest (ROIs) were delineated in each lesion and in contralateral hemisphere, according to the appearance on T$_2$-weighted images, contrast-enhanced T$_1$-

weighted images and trace-weighted maps. In particular, in heterogeneous lesions evident areas of necrosis, contrast enhancement, edema (perilesional hyperintensity on T_2-weighted images), and high cellularity (hyperintensity on trace-weighted maps), were segmented.

The mean and standard deviation of each estimated parameter were calculated in each ROI. The comparison between NODDI and the isotropic model by the BIC was performed only in areas with high orientation dispersion (ODI > 0.4), because a poor performance of the isotropic model is trivial where anisotropy is high. The statistical significance of the difference was compared using a paired one-tail t-test. The correlation between corresponding parameters in the two models (f_{ICV} and f_R, f_{ISO} and f_F, respectively) was evaluated in the same areas, using the Pearson's correlation coefficient.

Concerning the correlation between dMRI (NODDI and DTI) and the tumor grade a single representative value for each parameter of the former was derived to be related to the single outcome of neuropathology. Namely, the maximum f_{ICV} and f_{ISO} among the lesion ROIs was considered, while f_{ECV} was averaged among all the ROIs, excluding those with high cellularity (f_{ICV} > 0.3). This choice was motivated by a different spatial distribution of the parameters: generally tumors (especially LGG) exhibit multiple regions with high f_{ECV}, possibly with some isolated areas with high f_{ICV} and f_{ISO}. For DTI, the mean, minimum and maximum MD and the mean FA among the ROIs were considered.

The relation between each dMRI parameter and the tumor grade was assessed by comparing the mean value of each dMRI parameter in the three groups defined by the tumor grades (WHO grade II, III and IV); an unpaired one-tail t-test with unequal variances was used to evaluate the statistical significance of the differences.

3.3. Results

3.3.1. Neuropathological diagnosis and conventional MRI

In the group of 71 patients, 27 were diagnosed with a WHO grade II lesion: 14 oligodendrogliomas, 6 astrocytomas and 7 oligoastrocytomas. 2 patients presented areas with contrast enhancement, 4 had areas of presumed high cellularity basing on trace-weighted map hyperintensity.

15 patients were diagnosed with a WHO grade III tumor: 4 anaplastic oligodendrogliomas, 8 anaplastic astrocytomas and 3 anaplastic oligoastrocytomas. 5 patients presented areas of contrast enhancement, 8 had areas of presumed high cellularity.

29 patients were diagnosed with a WHO grade IV tumor: 28 GBM and 1 gliosarcoma. All the 29 patients presented areas of contrast enhancement, 25 had areas of presumed high cellularity.

17 regions of presumed peritumoral edema were identified on the T_2-weighted images (16 in grade IV patients, 1 in a grade III patient).

3.3.2. Comparison between NODDI and the isotropic diffusion model

From the subset of 20 patients presenting pathological regions of high cellularity, analyzed with both NODDI and the isotropic diffusion model defined in equation (3.3), the ROIs having high orientation dispersion (ODI > 0.4) were selected, resulting in a dataset of parameters from the two models for 44 ROIs.

The comparison of the BIC between the two models showed a better performance of NODDI in all the ROIs. The mean BIC was 609.88 ± 134.99 for NODDI and 671.71 ± 163.72 for the isotropic model. Considering only the 25 pathological areas with high cellularity ($f_{ICV} > 0.3$), which are the primary target of this analysis, the mean BIC was

631.53 ± 175.39 for NODDI and 700.43 ± 206.89 for the isotropic model. In both cases a paired t-test demonstrated statistical significance of the differences (p < 0.001).

In the same ROIs, the volume fractions estimated by the two models (f_{ICV} and f_R, f_{ISO} and f_F, respectively) were compared.

A very good correlation was found both between f_{ICV} and f_R (figure 3.4) and between f_{ISO} and f_F (figure 3.5); the Pearson's correlation coefficients were 0.903 and 0.961, respectively. However, some important differences in the absolute values of the estimated fractions can be noticed: the angular coefficients of the lines of regression were 0.272 for f_{ICV} vs. f_R and 0.619 for f_{ISO} vs. f_F, respectively. So, if the isotropic model is considered as a valid reference in areas of low diffusion anisotropy, NODDI tends to underestimate both the volume fractions, especially f_{ICV}.

According to these results, NODDI can fit the data well even in regions with relatively high isotropic restriction; the estimated volume fractions can be meaningful parameters for comparing different lesions, but their absolute value displays a consistent scaling error. Indeed, the relation between f_{ICV} and the real restricted volume can be affected by the simplification of sticks with null radius.
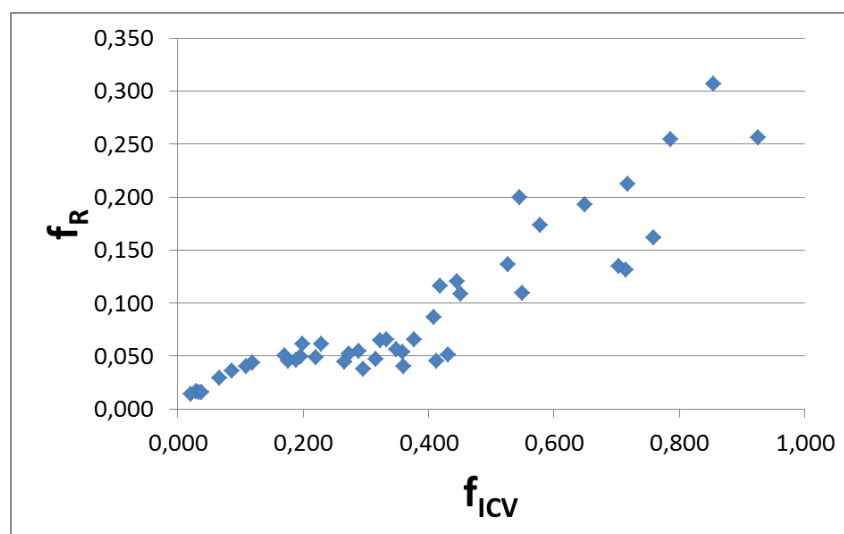
Figure 3.4. Correlation between f_{ICV} and f_R in 44 ROIs with ODI > 0.4
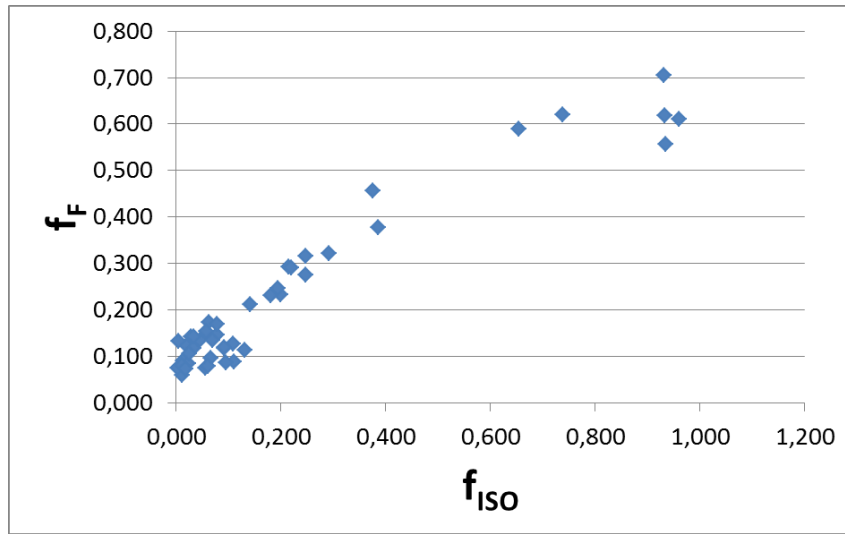
Figure 3.5. Correlation between f_{ECV} and f_F in 44 ROIs with ODI > 0.4

3.3.3. Estimated DTI and NODDI parameters

In this paragraph, a qualitative overview of the estimated NODDI and DTI parameters in the different types of lesions will be presented, with particular reference to the differentiation between tumor grades. For each tumor grade, the typical pattern of NODDI and DTI parameters will be presented, and some representative plots will be shown.

In the great majority of grade II gliomas the most evident result was an increase of f_{ECV} with respect to the contralateral healthy tissue (figure 3.6 and 3.7). MD was slightly increased with respect to the healthy tissue; FA was reduced and ODI was increased with respect to the contralateral WM, generally with a diffusion anisotropy similar or even smaller than the healthy GM.

In 2 cases there were areas with relatively increased f_{ICV} with respect to the rest of the lesion (see the second bar in figure 3.8); in these areas MD was relatively low.
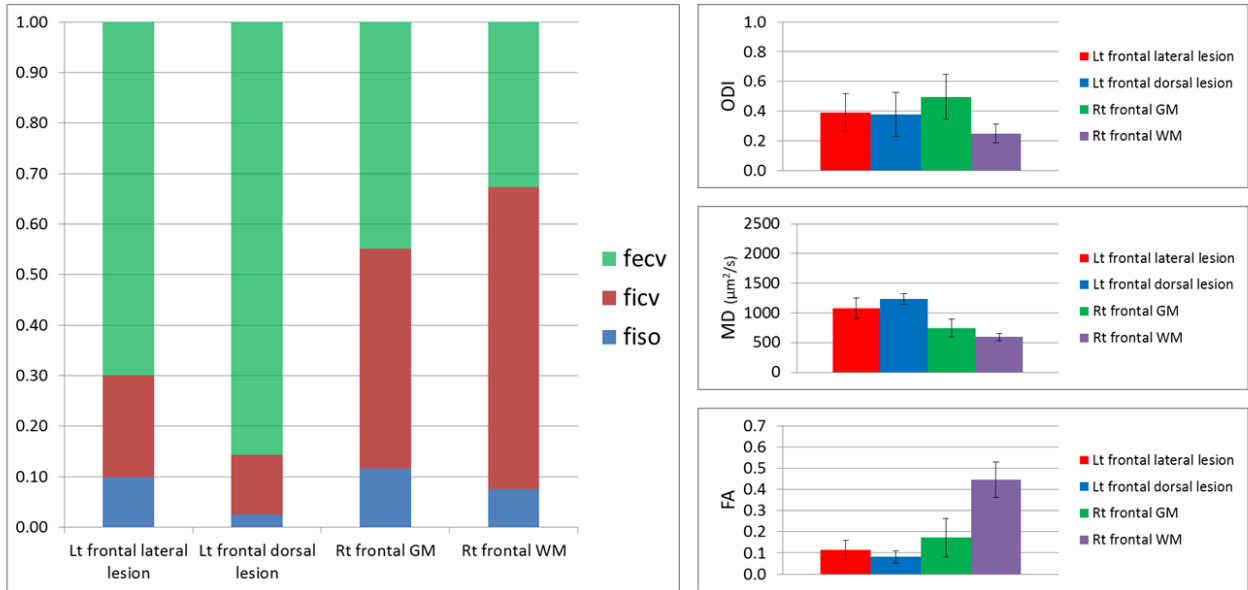
Figure 3.6. Parameters estimated by NODDI (f_{ECV}, f_{ICV}, f_{ISO} and ODI) and by DTI (MD and FA) in an oligodendroglioma showing typical characteristics of grade II gliomas. The bar graph on the left side shows the mean relative fractions of the three compartments estimated by NODDI in each ROI, while the bar graphs on the right side show the mean and standard deviation (error bars) of ODI, MD and FA in each ROI.

The first two ROIs were placed in different regions of the tumor, while the other two ROIs were placed in the contralateral GM and WM, respectively.
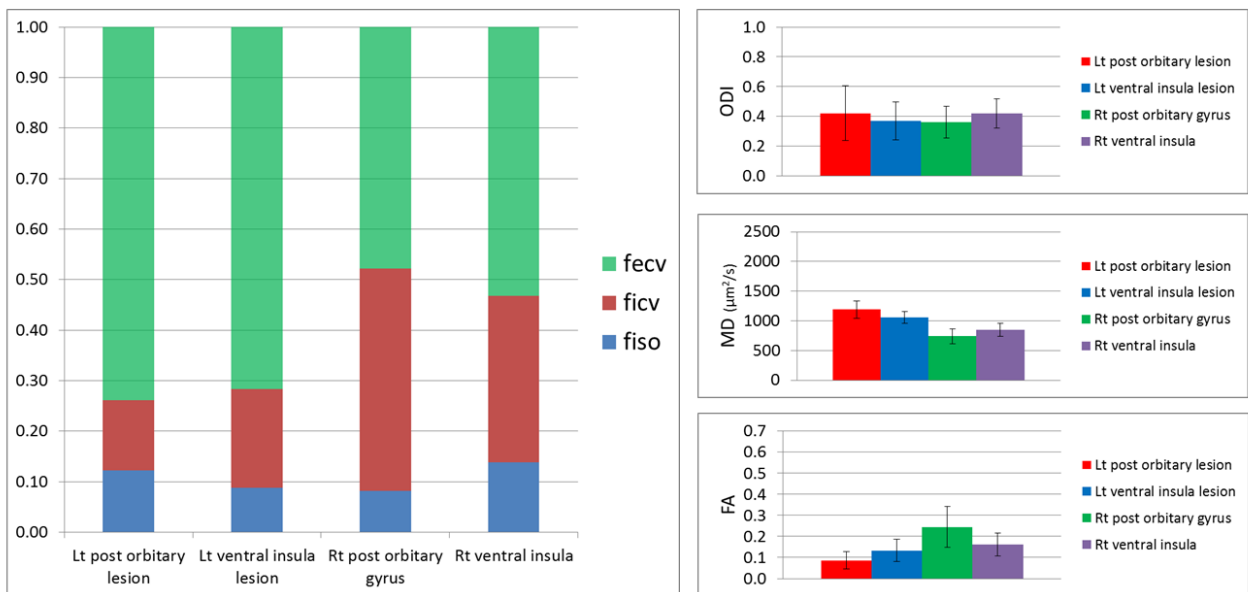
Figure 3.7. Parameters estimated by NODDI and by DTI in an oligodendroglioma showing typical characteristics of grade II gliomas. The bar graphs have the same meaning as in figure 3.6. The first two ROIs were placed in different affected regions, while the other two ROIs were placed in the corresponding contralateral areas.
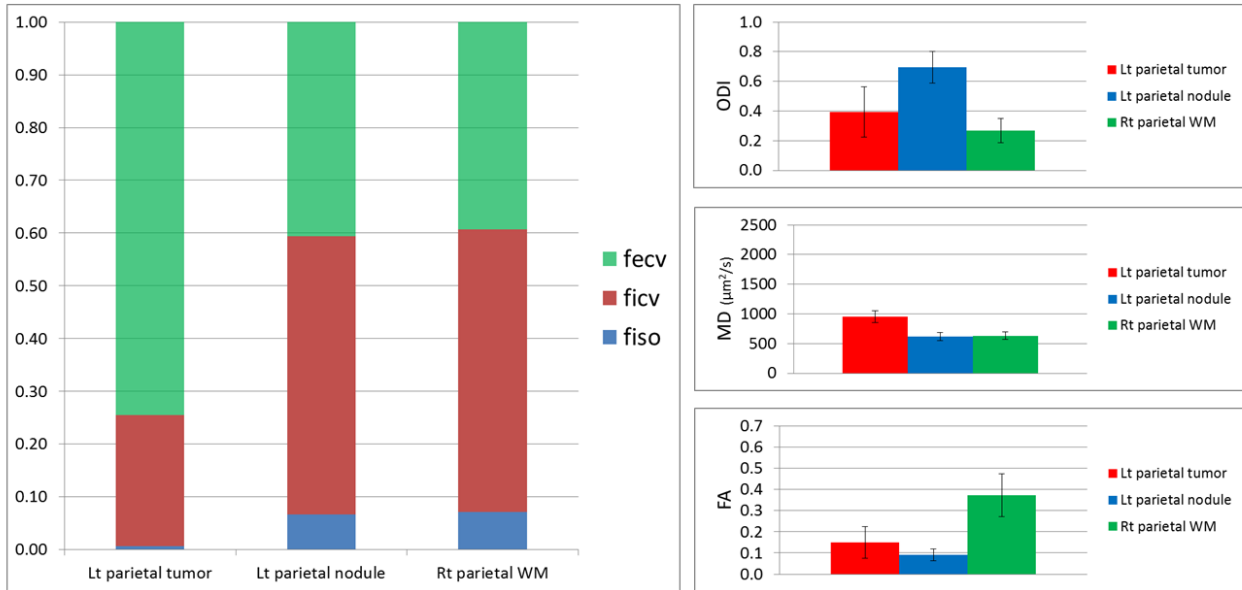
Figure 3.8. Parameters estimated by NODDI and by DTI in an oligoastrocytoma with an area with increased cellularity. The bar graphs have the same meaning as in figure 3.6. The first two ROIs were placed in the bulk tumor and in the nodule with higher dMRI intensity; the third ROI was placed in the contralateral WM.

In grade III gliomas few different patterns of NODDI parameters were found considering the population of this study.

Some cases presented very similar characteristics to those described for grade II: tumors with increased f_{ECV} and MD with respect to the healthy contralateral regions and low FA even when the lesion was in a WM area (figure 3.9).

However, in several cases regions with relatively high f_{ICV} were found, usually corresponding to areas of hyperintensity in the diffusion trace-weighted maps. With respect to the areas with high f_{ECV}, these regions had lower MD values, usually comparable or even lower than the contralateral healthy tissue. They were interpreted as regions of higher tumor cellularity, likely the most aggressive parts of the tumors.

In some patients areas with high f_{ICV} were detected together with areas with high f_{ECV} (as the first ROI in figure 3.10), while in other cases all the considered affected ROIs had high f_{ICV} (figure 3.11).

In two patients, areas with increased f_{ISO} and MD were detected.
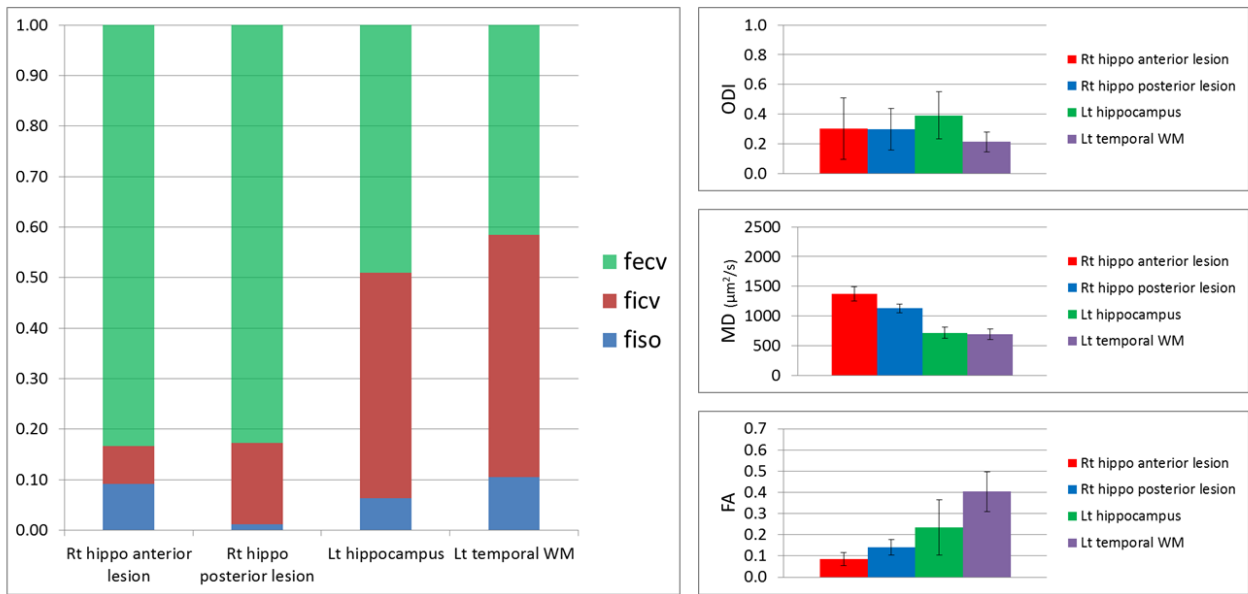
Figure 3.9. Parameters estimated by NODDI and by DTI in an anaplastic astrocytoma without areas of increased cellularity. The bar graphs have the same meaning as in figure 3.6. The first two ROIs were placed in different regions of the tumor, while the other two ROIs were placed in the contralateral GM and WM, respectively.
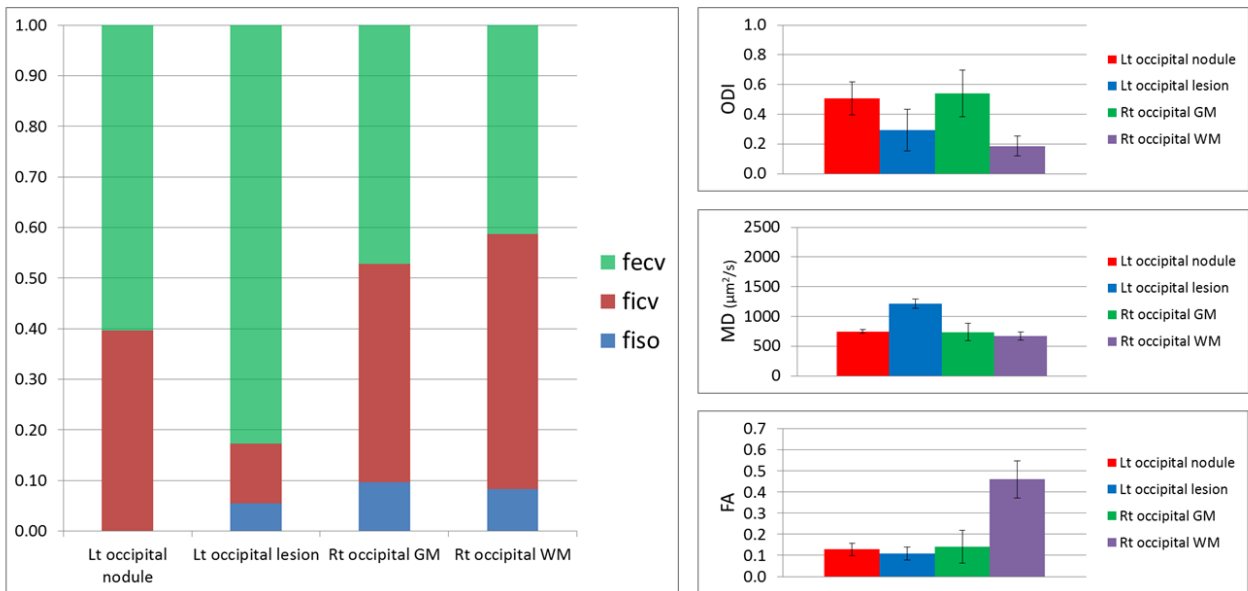
Figure 3.10. Parameters estimated by NODDI and by DTI in an anaplastic oligoastrocytoma with an area of presumed increased cellularity. The bar graphs have the same meaning as in figure 3.6. The first two ROIs were placed in different regions of the tumor, while the other two ROIs were placed in the contralateral GM and WM, respectively.
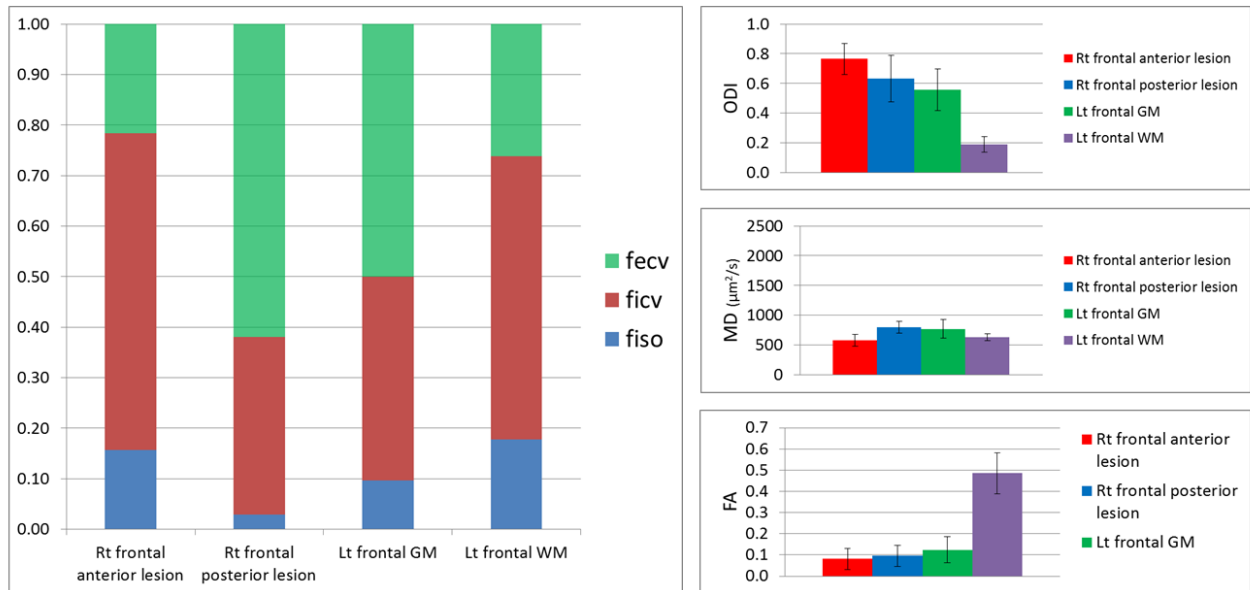
Figure 3.11. Parameters estimated by NODDI and by DTI in an anaplastic oligoastrocytoma with areas of presumed increased cellularity. The bar graphs have the same meaning as in figure 3.6. The first two ROIs were placed in different regions of the tumor, while the other two ROIs were placed in the contralateral GM and WM, respectively.

Grade IV gliomas were generally very heterogeneous both on conventional MRI images and in the distribution of estimated NODDI parameters.

In most of the cases, regions with increased f_{ISO} were found, usually in the core of the tumor; they were interpreted as necrotic areas. In these areas f_{ISO} ranged from very large fractions as in the first ROI in figure 3.12 and in figure 3.13 to relatively smaller fractions as in the second ROI shown in figure 3.14, but always much larger than in the healthy tissue. The MD was generally increased, but with a certain variability.

Regions with contrast enhancement, as the second ROI in figure 3.12 and in figure 3.13, were associated with relatively increased f_{ECV} and f_{ISO} and relatively high MD.

In most of the lesions, regions with high f_{ICV} were found, with the same features described above for the areas of presumed high cellularity in grade III gliomas. See for example the third ROI in figure 3.13 and the first one in figure 3.14

In some patients, regions with increased f_{ECV} were detected, with characteristics similar to those described for grade II gliomas. They were interpreted as areas with low cellularity but not necrotic, probably the less aggressive parts of the tumor, at an earlier stage of development with respect to the rest of the lesion. See for example the fourth ROI in figure 3.14.

In several grade IV patients peritumoral areas of presumed vasogenic edema were detected (for example, the third ROI in figure 3.12 and in figure 3.14). These areas were associated with increased f_{ECV} and f_{ISO} and with a low ODI, usually comparable with that of healthy WM. MD was high, FA was low compared to the healthy WM.

Considering the 17 ROIs of presumed vasogenic edema, they all had $f_{ICV} < 0.2$, $f_{ISO} > 0.15$ and $ODI < 0.3$, with only one exception with higher ODI. On the contrary, it was not possible to identify univocal DTI parameters for edema: MD is generally high, but with a relative degree of variability, and FA was generally quite low, ranging from 0.05 to 0.25. The impact of this finding on tractography is discussed in the next chapter.
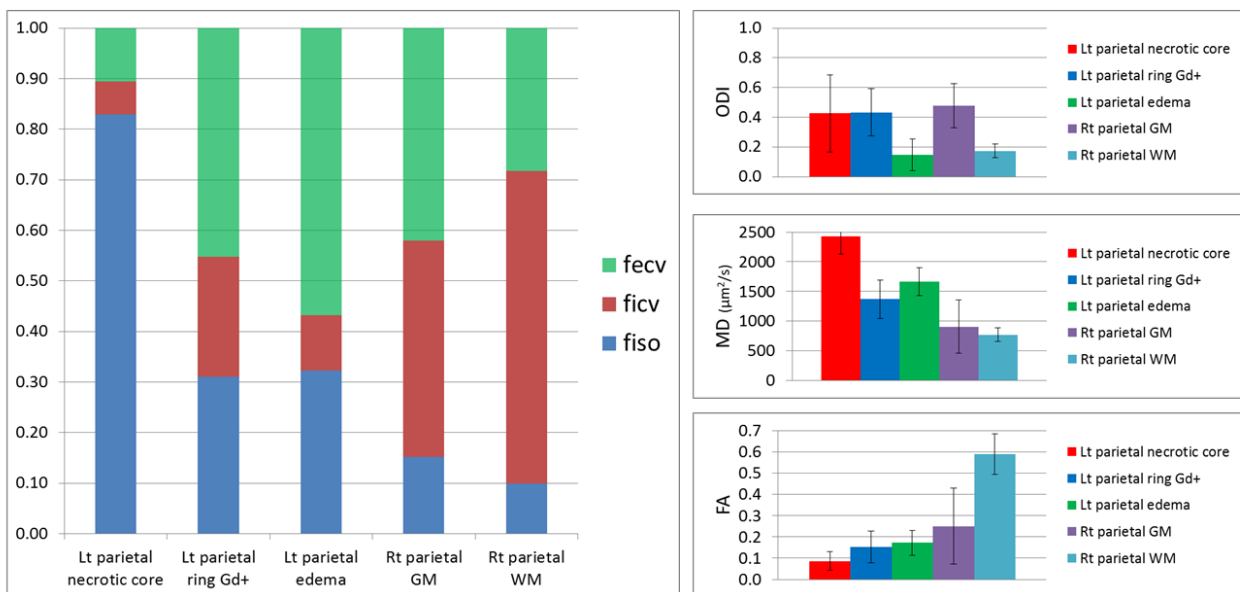
Figure 3.12. Parameters estimated by NODDI and by DTI in a representative GBM with areas of presumed necrosis, contrast enhancement and edema. The bar graphs have the same meaning as in figure 3.6. The first three ROIs were placed in different regions of the tumor and edema, while the other two ROIs were placed in the contralateral GM and WM, respectively.
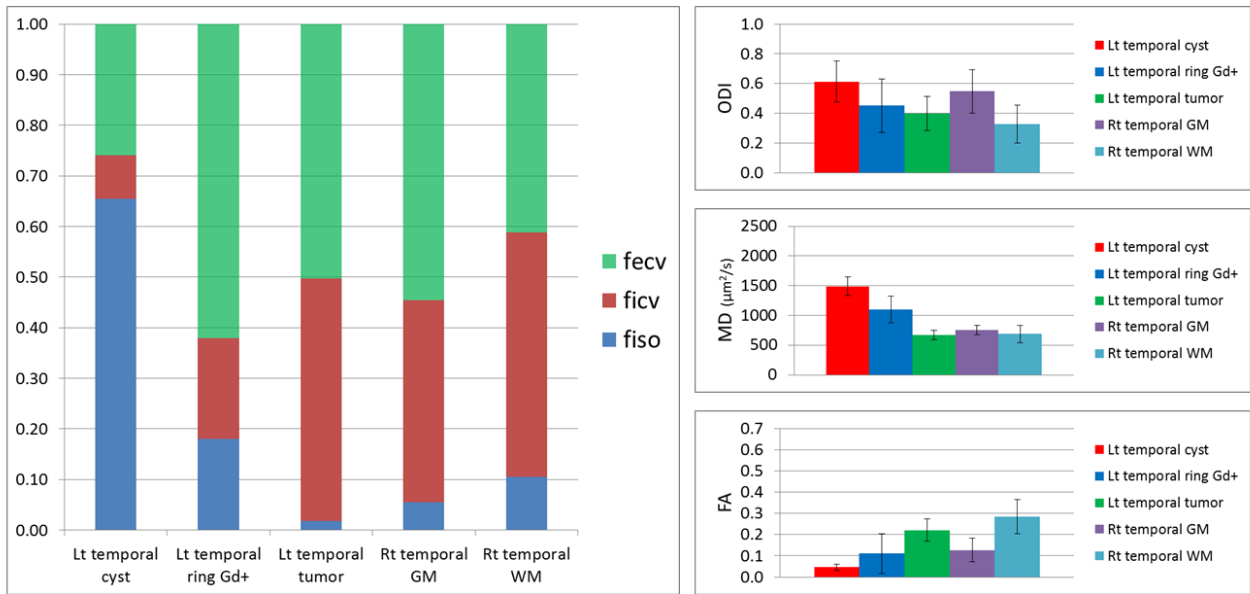
Figure 3.13. Parameters estimated by NODDI and by DTI in a representative GBM with an area of presumed increased cellularity. The bar graphs have the same meaning as in figure 3.6. The first three ROIs were placed in different regions of the tumor, while the other two ROIs were placed in the contralateral GM and WM, respectively.
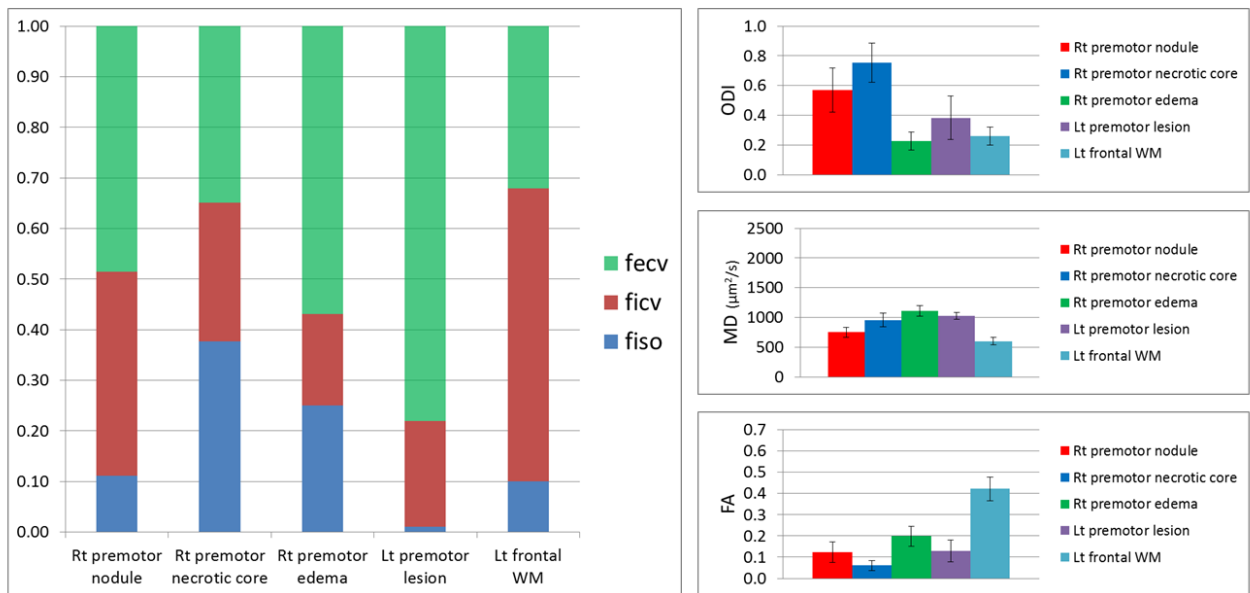

Figure 3.14. Parameters estimated by NODDI and by DTI in a representative GBM with an area of increased extracellular volume. The bar graphs have the same meaning as in figure 3.6. The first three ROIs were placed in different regions of the tumor and edema, while the other two ROIs were placed in the contralateral GM and WM, respectively.

In summary, the parameters estimated by NODDI had quite different distributions among the ROIs delineated in tumors with different WHO grade. On the contrary, DTI parameters were not very informative: MD values were generally quite high, but not specific to the different lesion types; only in the areas with presumed high cellularity relatively low MD values were found rather consistently. FA values provided no specific information about the lesions. In the following paragraph, a more quantitative approach will be used for the correlation between NODDI and DTI parameters and the tumor grade.

3.3.4. Correlation between dMRI parameters and the tumor grade

The mean f_{ECV}, maximum f_{ICV} and maximum f_{ISO} were calculated among the ROIs in each lesion, and then compared between the grade II, grade III and grade IV gliomas to investigate the possibility to differentiate between different tumor grades basing on the microstructural parameters estimated by NODDI.

The average features of grade II and grade III gliomas were similar (grade III cases presented only a slight increase of f_{ECV} and f_{ICV}), while grade IV gliomas had lower f_{ECV}, higher f_{ICV} and higher f_{ISO} compared to the other two groups (figure 3.15).
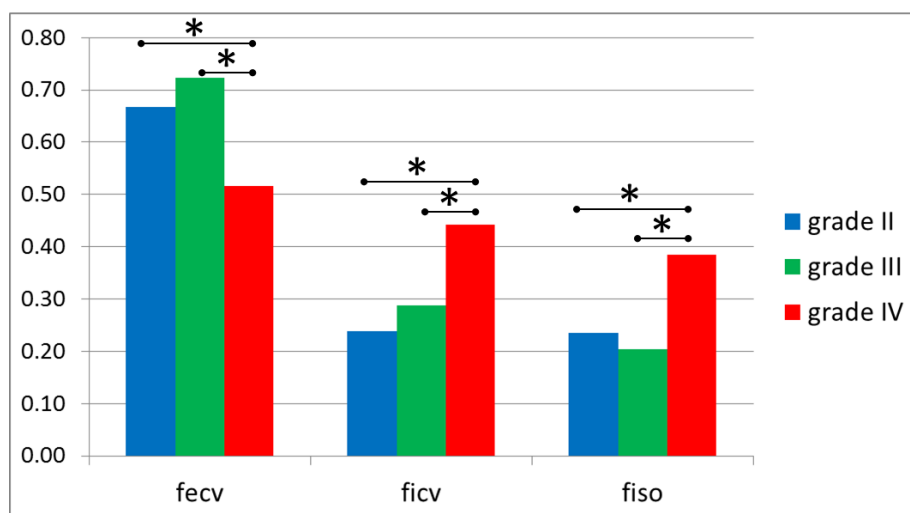
Figure 3.15. Bar graph showing the mean f_{ECV}, maximum f_{ICV} and maximum f_{ISO} averaged among the patients with grade II, grade III and grade IV gliomas, respectively. The significant differences are marked with stars.

The differences between grade II and grade IV and between grade III and grade IV were significant for all NODDI parameters (p < 0.01), while none of them showed statistically significant differences between grade II and grade III gliomas.

Considering DTI parameters, the mean MD and FA were calculated among the ROIs in each patient; moreover, the minimum and maximum MD were considered, because they were assumed to be the best DTI indices of areas of increased cellularity and necrosis, thus corresponding to the maximum f_{ICV} and f_{ISO}, respectively.

No DTI parameter showed important differences between grade II and grade III groups, while grade IV gliomas had slightly lower mean MD, a lower minimum MD and a slightly higher maximum MD. The FA looked uninformative to the tumor grade.

Only the difference in mimimum MD between grade II and grade IV groups was significant (p < 0.01)
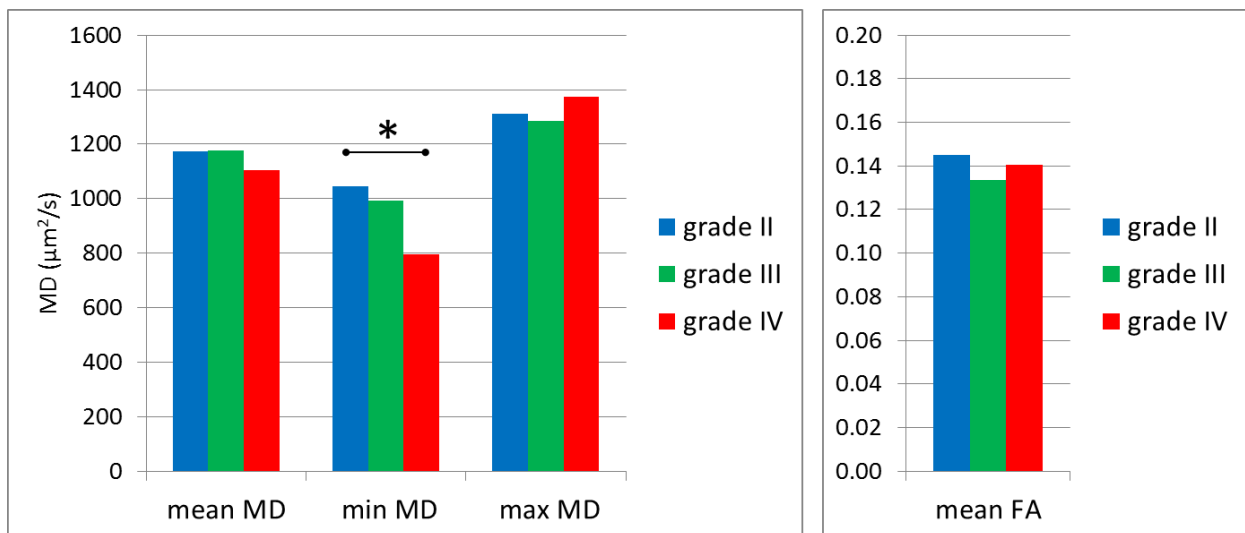
Figure 3.15. Bar graph showing the mean, minimum and maximum MD and the mean FA averaged among the patients with grade II, grade III and grade IV gliomas, respectively. The significant differences are marked with stars.

3.4. Discussion

In this study, the dMRI data from 71 patients with brain gliomas were analyzed with NODDI to investigate the possibility of this model to characterize the microstructural features of the different types of tumors.

In a preliminary step, NODDI results in a subset of 20 patients were compared with those from an isotropic diffusion model to understand if NODDI can be useful also in areas with isotropic restriction. This comparison showed a better performance of NODDI (evaluated by the BIC) in all the considered regions with relatively high orientation dispersion.

Moreover, the corresponding volume fractions of the two models were highly correlated, so it was possible to conclude that a relatively high value of f_{ICV} associated with a high value of ODI could be an index of isotropic restriction. However, a scaling error in the absolute values of the estimated volume fractions was also noticed. In particular, the f_{ICV} estimated by NODDI was always much smaller than the f_R estimated by the isotropic model. This could be expected from the mathematical form of the intracellular space in NODDI, modeled as a set of sticks with free diffusion along the axis of each stick and perfectly restricted diffusion in the perpendicular direction. When the ODI is high, the set of sticks can be thought as approximately equivalent to the "average" of a compartment with isotropic restriction (coming from diffusion in the perpendicular directions of each stick) and a compartment with isotropic free, or at least hindered, diffusion (coming from diffusion along the sticks). Thus, the volume fraction of the compartment with truly restricted diffusion is smaller than the f_{ICV} estimated by NODDI.

As a conclusion about this preliminary experiment, NODDI is sensitive to isotropic restricted diffusion, as is expected in regions of high cellularity inside brain tumors, but the numeric values of the estimated volume fractions have to be considered carefully; however,

they should be still useful when comparing data from different regions or different subjects acquired in the same conditions.

Once these preliminary results confirmed the possibility to investigate the microstructural features of brain tissues including isotropic restriction, the analysis of NODDI and DTI parameters was extended to all the patients in the studied population. Multiple ROIs were drawn for each patient in the affected and contralateral healthy areas identified on T_2-weighted and contrast-enhanced MRI. The patients were classified according to the tumor grade defined by the neuropathological analysis and the difference in NODDI and DTI parameters between groups were examined.

In almost all the ROIs analyzed in grade II gliomas, NODDI provided high f_{ECV} values, with reduced f_{ICV}. This suggests that these tumors have low cellularity, since most of water is in the extracellular space.

Also in grade III gliomas ROIs with increased f_{ECV} were found, but in several cases there were additional regions with relatively increased f_{ICV}, presumably associated with high cellularity.

In grade IV gliomas, areas with different features were typically observed: some ROIs had very high f_{ISO} (presumably necrotic or cystic areas), some had both increased f_{ISO} and relatively high f_{ECV} (usually associated with contrast-enhancement), and others had relatively high f_{ICV} (high cellularity). Peritumoral areas of presumed edema had increased f_{ECV} and f_{ISO} (reduced f_{ICV}) with relatively low ODI.

However, this classification had some exceptions: for example, few ROIs with presumed high cellularity or with high f_{ISO} were found in grade II tumors, and ROIs with presumed low cellularity (f_{ECV}) were found in grade IV cases.

A quantitative group-analysis showed statistically significant differences in NODDI parameters between grade IV and both grade II and III, with a reduction of f_{ECV} and an increase of maximum f_{ICV} and f_{ISO} in grade IV cases. These changes are coherent with

the previous qualitative analysis, since in grade IV patients less ROIs with low cellularity and more ROIs with high cellularity or necrosis were detected.

DTI parameters were much less specific to the different kinds of lesions identified. In particular, MD values were generally increased with respect to the contralateral healthy tissues, but similar values were obtained in many cases with a quite different appearance on conventional MRI and different NODDI volume fractions; for example, both areas with increased f_{ECV} and areas with relatively high f_{ISO} had similarly increased MD. The only exception was the quite consistent detection of areas with low cellularity by low MD values, comparable or even smaller than in healthy regions.

FA values were not informative about the lesional features; quite low values were usually found in affected ROIs, and the differences among them appeared to be more correlated with the anatomical location of the tumor (WM lesions tended to have higher FA) than with the microstructural changes induced by the tumor itself.

The only statistically significant difference in DTI parameters shown by the group-analysis was a reduction of the minimum MD in grade IV cases with respect to grade II (but not grade III) cases. This result probably corresponds to the increase in f_{ICV} observed by NODDI, because both are assumed to be indices of the presence of highly cellular regions. Instead, the other findings by NODDI (reduced portion of ROIs with low cellularity and increase of necrosis) were not evident with DTI, as could be expected from the qualitative results described above.

It can be concluded that DTI is much less specific than NODDI in the differentiation between tumor grades and in the microstructural characterization of the various lesions and lesion components.

The main limitation of this study is the lack of precise correspondence between the ROIs identified on MRI for the analysis of NODDI and DTI parameters and the bioptic samples used for the neuropathological examination. Thus, the dMRI parameters obtained in the

various ROIs had to be combined to perform a correlation analysis with the tumor grade, which in turn were defined on a sample with unknown spatial relationship with the MRI ROIs. As a consequence, it was not possible to validate NODDI findings in terms of the regional variation of neuropathological features. A rather obvious future extension of this work would be a study with bioptic samples extracted from the same locations of the ROIs drawn on MRI (or vice-versa). This would allow a more precise correlation between NODDI results and histopathological measures, for example indices of cellularity or tumor proliferation. However, the findings of this work are compatible with the known features of the different glioma grades and with the appearance of the examined ROIs on on T_2-weighted and contrast-enhanced images. Then it is expected that the validity of these preliminary results will be confirmed by neuropathological validation.

If NODDI results in the differentiation between the lesion components will be validated, a further step would be to identify precise thresholds for a classification of affected areas by NODDI parameters, as shown in paragraph 3.3.3 for peritumoral edemas, which could not be easily identified basing on NODDI parameters. However, this task arises several issues about the meaning of the absolute values of the estimated parameters.

First of all, no model is perfect: NODDI allows a good fitting of clinical dMRI data, but it implies many assumptions on the underlying tissue and the interpretation of the estimated volume fractions could be not very straightforward in some cases, as highlighted in the case of isotropic restriction. Moreover, NODDI is a single fiber model as DTI, and could provide not correct results in areas of fiber crossing, but this should not be a relevant issue in tumor areas.

Even if the hypotheses of the model about the geometrical features of the tissue were perfectly satisfied, the volume fractions are relative to the signal and not to the amount of water present in the voxel, which could be quite variable between different regions, especially in brain tumors. Moreover, they are estimated from images with relatively high

T_2-weighting and the different T_2 values among the compartments is not taken into account by NODDI, so the estimated fractions themselves are T_2-weighted. This problem could be solved by estimating proton-density and T_2 from images acquired with multiple echo times, but this would require a more complex acquisition scheme with a longer acquisition time, which would limit its clinical application. Alternatively, the found volume fractions could be normalized using an internal reference, such as the contralateral tissue, but this could introduce biases because the microstructural features of normal brain have a certain degree of variability among anatomical locations.

Finally, similar NODDI parameters could be found in quite different conditions. For example, the tumor components with high cellularity, which are assumed to arise from previously low-cellularity lesions, have often similar volume fractions to the healthy tissue (see figures 3.8, 3.11 and 3.13). Thus, it is possible that a tumor component at a very initial stage, with only a limited increase of f_{ECV}, has very similar volume fractions to a high-grade lesion with increased cellularity. Therefore, NODDI parameters alone may be insufficient for an accurate classification of lesions in some cases, and have to be combined with data from conventional MRI or other sources.

In conclusion, this work provided promising preliminary results about glioma differentiation and characterization based on NODDI, even though this procedure presents many challenges. If these findings are validated, NODDI could be a very useful tool for the diagnosis and the planning of therapy and/or surgery in brain tumor patients.

Bibliography

Alexander DC, Hubbard PL, Hall MG, et al. Orientationally invariant indices of axon diameter and density from diffusion MRI. *Neuroimage*. 2010;52(4):1374-1389.

Beppu T, Inoue T, Shibata Y, et al. Measurement of fractional anisotropy using diffusion tensor MRI in supratentorial astrocytic tumors. *J Neuro-Oncol*. 2003;63(2):109-116.

Chenevert TL, McKeever PE, Ross BD. Monitoring early response of experimental brain tumors to therapy using diffusion magnetic resonance imaging. *Clin Cancer Res*. 1997;3(9):1457-1466.

Gauvain KM, McKinstry RC, Mukherjee P, et al. Evaluating pediatric brain tumor cellularity with diffusion-tensor imaging. *Am J Neuroradiol*. 2001;177(2):449-454.

Guo AC, Cummings TJ, Dash RC, Provenzale JM. Radiology Lymphomas and High-Grade Astrocytomas : Comparison of Water Diffusibility and. *Neuroradiology*. 2002;224(16):177-183.

Inoue T, Ogasawara K, Beppu T, Ogawa A, Kabasawa H. Diffusion tensor imaging for preoperative evaluation of tumor grade in gliomas. *Clini Neurol Neurosurg*. 2005;107(3):174-180.

Jenkinson M, Bannister P, Brady M, Smith S. Improved Optimization for the Robust and Accurate Linear Registration and Motion Correction of Brain Images. *Neuroimage*. 2002;17(2):825-841.

Kang Y, Choi SH, Kim KG. Gliomas : Histogram Analysis of Apparent Diffusion Coeffi cient Maps Purpose : Methods : Results : *Radiology*. 2011;261(3):882-890.

Kono K, Inoue Y, Nakayama K, et al. The role of diffusion-weighted imaging in patients with brain tumors. *Am J Neuroradiol*. 2001;22(6):1081-1088.

Lee HY, Na DG, Song I-C, Lee DH. Diffusion-Tensor Imaging for Glioma Grading at 3-T Magnetic Resonance Imaging : Analysis of Fractional Anisotropy and Mean Diffusivity. *J Comput Assist Tomogr*. 2008;32(800):298-303.

Liu X, Tian W, Kolar B, et al. MR diffusion tensor and perfusion-weighted imaging in preoperative grading of supratentorial nonenhancing gliomas. *Neuro Oncol*. 2011;13(4):447-455.

Louis DN, Ohgaki H, Wiestler OD, et al. The 2007 WHO classification of tumours of the central nervous system. *Acta Neuropathol*. 2007;114(2):97-109.

Rahm V, Boxheimer L, Bruehlmeier M, et al. Focal changes in diffusivity on apparent diffusion coefficient MR imaging and amino acid uptake on PET do not colocalize in nonenhancing low-grade gliomas. *J Nucl Med*. 2014;55(4):546-550.

Scott JN, Brasher PMA, Sevick RJ, Rewcastle NB, Forsyth PA. How often are nonenhancing supratentorial gliomas malignant? A population study. *Neurol* . 2002;59(6):947-949.

Server A, Graff BA, Josefsen R, et al. Analysis of diffusion tensor imaging metrics for gliomas grading at 3 T. *Eur J Radiol*. 2014;83(3):e156-e165.

Stadlbauer A, Ganslandt O, Buslei R, Buchfelder M, Salomonowitz E, Nimsky C. Gliomas : Histopathologic Evaluation of Changes in Directionality and Magnitude of Water Diffusion at Diffusion-Tensor MR Imaging. *Radiology*. 2006;240(3):803-810.

Sugahara T, Korogi Y, Kochi M, et al. Usefulness of diffusion-weighted MRI with echo-planar technique in the evaluation of cellularity in gliomas. *JMRI-J Magn Reson Im*. 1999;9(1):53-60.

Svolos P, Kousi E, Kapsalaki E, et al. The role of diffusion and perfusion weighted imaging in the differential diagnosis of cerebral tumors: a review and future perspectives. *Cancer Imaging*. 2014;14(1):20.

Wang R, Benner T, Sorensen AG, J W V. Diffusion Toolkit : A Software Package for Diffusion Imaging Data Processing and Tractography. In: *Proc Intl Soc Mag Reson Med*; 2007:3720.

Yushkevich PA, Piven J, Hazlett HC, et al. User-guided 3D active contour segmentation of anatomical structures: significantly improved efficiency and reliability. *Neuroimage*. 2006;31(3):1116-1128.

Zhang H, Schneider T, Wheeler-Kingshott CAM, Alexander DC. NODDI: practical in vivo neurite orientation dispersion and density imaging of the human brain. *Neuroimage*. 2012;61(4):1000-1016.

4. NODDI-BASED TRACTOGRAPHY IN PERITUMORAL EDEMA

Fast is fine, but accuracy is everything.

Xenophon

This chapter addresses the enhancement of fiber reconstruction in peritumoral edema where Diffusion Tensor tractography fails due to decreased FA, but surgical planning may consider the preservation of important surviving bundles. NODDI, based on its simplified description of fibers and their distinction from the extracellular compartment and free water is a good candidate for more sensitive and specific detection of fiber direction, though feasible from data achievable in clinical scans.

Results were described in [Figini 2014a] and a preliminary presentation was given in [Figini 2014b].

4.1. Introduction: Tractography in oncological neurosurgical planning

Diffusion tractography (paragraph 1.6) is widely used in research studies to qualitatively evaluate the presence and the path of bundles connecting brain regions, or to quantitatively compare them in terms of "connection strength", even though the validity of the latter approach has been discussed [Jones 2010].

It also plays an important role in glioma surgery. When planning and performing a neurosurgery operation, it would be fundamental to define the boundaries of the lesion and whether the surrounding areas contain important WM bundles or have residual

functionality, in order to preserve undamaged tracts; Diffusion tensor tractography (DTT, [Mori 1999, Basser 2000]) is widely used for this purpose, together with other techniques, such as functional MRI (fMRI) and intraoperative electrical stimulation [Black 1987, Bizzi 2009, Ng 2010, Dimou 2013]. In particular, the presurgical planning usually includes fMRI to identify areas involved in specific functional tasks, and DTT to reconstruct the trajectory of structurally undamaged WM tracts. Both fMRI and DTT results can be visualized in neuronavigation systems during surgery (figure 4.1), and their spatial relationship with the tumor is taken into account to resect the maximum part of the affected tissue without causing neurologic deficits [Wolbers 2014]. In this phase, subcortical electrical stimulation is usually applied to further validate the detection and localization of still functional areas to be preserved by the surgeon [Bello 2008].
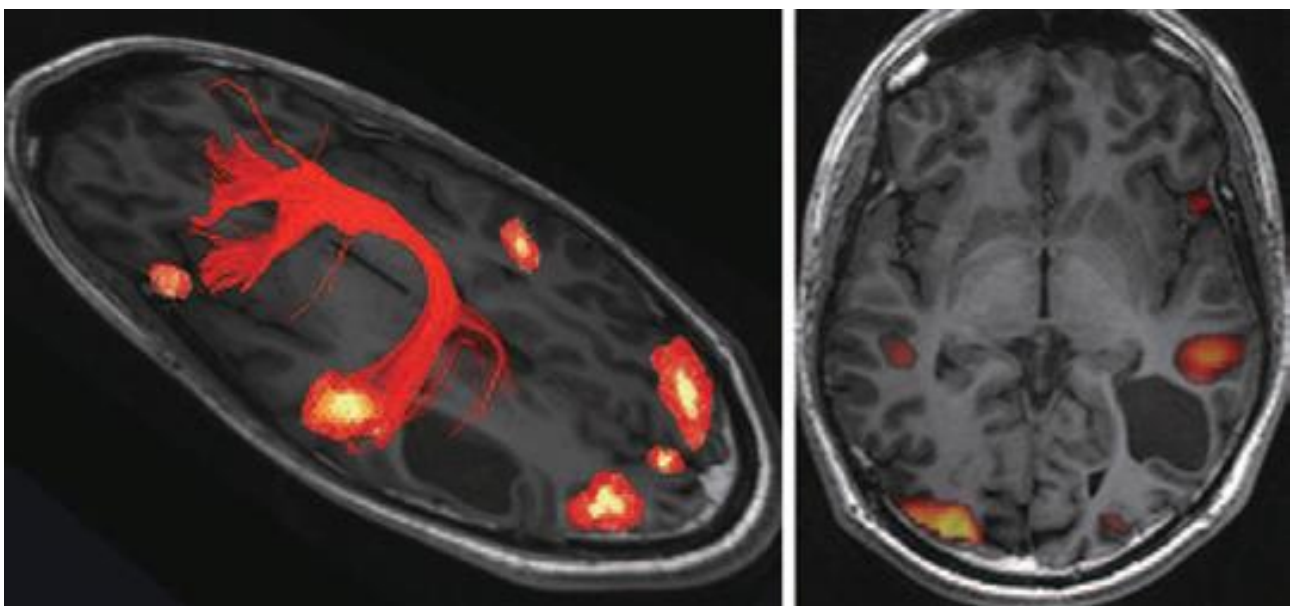
Figure 4.1. Visualization of DTT and fMRI results in neuronavigation for neuro-oncological surgery. Left: DTT reconstruction of the arcuate fasciculus. Left and right: fMRI showing the brain areas activated in a verbal fluency task. Reproduced from [Wolbers 2014]

However, in some cases DTT fails to reconstruct WM tracts that are still intact and functional, but surrounded by damaged brain tissue. This limitation is mainly related to the termination criteria generally used in DTT, based both on a maximum angle between the

directions in adjacent voxels to avoid unnaturally sharp bends and on a threshold on FA to prevent the reconstruction of tracts where the estimation of directions is not reliable (paragraph 1.6). FA is not very specific: a low value of FA could be related to different conditions, for example to isotropic diffusion, such as in the CSF, to the presence of WM fibers with no prevalent direction, such as in the case of "fiber crossing", or to partial volume between WM and isotropic tissues. In the last case fibers with a coherent direction may be present, but not reconstructed by DTT due to the reduction of FA.

A common case in oncological presurgical mapping in which DTT shows this limit is the reconstruction of fibers through areas of vasogenic edema, where DTI parameters do not characterize the tissue properly, as already discussed in paragraph 1.3. In areas of vasogenic edema low FA values are found [Lu 2003, Provenzale 2004], and almost no streamlines are reconstructed by DTT regardless of the actual state of underlying WM [Yamada 2003, Schonberg 2006, Bizzi 2009]. Conversely, it is common evidence that in those regions still functional tracts may be found, confounded by the abnormal presence of CSF. This was demonstrated by histology [Kuroiwa 1994], magnetic source imaging [Schiffbauer 2001] cortical stimulation [Berman 2004]. Moreover, a case was reported [Yamada 2003] in which the CST, initially not detected by DTT because of the presence of edema, was successfully reconstructed after the resection of the tumor and consequent reduction of edema.

Since the limitation of DTT in areas of partial volume is mainly related to its inadequacy in differentiating the characteristics of multiple compartments (the signal in each voxel is characterized by a single tensor), the use of a multicompartmental model could help to overcome it. In clinical applications, the recently proposed NODDI [Zhang 2012] seems advantageous over other models, because it provides specific microstructural parameters with a clinically-feasible acquisition scheme (paragraph 1.5).

The purpose of this work is to assess the feasibility of a NODDI-based tractography procedure (NODDIT) in brain tumor patients and the advantage over DTT. In particular, the utility of NODDI parameters to identify the presence of coherent fibers within vasogenic edema was investigated; the advantage of NODDI (and other multi-compartment models) over DTI is that it provides parameters specific to the WM compartment, thus solving partial volume issues, at least on a theoretical level. In particular, NODDI quantifies the amount of non-free diffusion, associated to brain tissue, thus NODDIT can use two separate thresholds to detect the presence of structures and to specifically evaluate the orientational coherence of fibers. On the contrary, in DTT the same parameter (FA) is used to assess both these conditions.

To allow a fair comparison with DTT, NODDIT parameters were first calibrated to have a performance as similar as possible to DTT on normal WM and next assessing the different outcomes in edema.

4.2. Materials and methods

4.2.1. MRI Acquisition, pre-processing and model fitting

The brain tumor patients selected for this work are a subset of the population of the study on the microstructural characterization of brain tumors described in chapter 3. The same acquisition, pre-processing and fitting procedures explained in paragraphs 3.2.1 and 3.2.2 were followed here, with the only exception of the analysis based on the isotropic diffusion model (paragraph 3,2,2).

In particular, the following parameters estimated by NODDI were considered: the principal direction of the intracellular compartment, the orientation dispersion index (ODI) and the

volume fraction of the CSF (f_{ISO}). From DTI, the first eigenvector, the FA and MD were considered.

4.2.2. Selection of the subjects for the study

From the population of patients with brain tumors described in chapter 3, 10 patients were chosen as a control group to calibrate NODDIT algorithm on healthy hemispheres and structures (C group) and 10 for analysis in tumor and tumor surrounding structure (T group). C subjects were selected according to clinical reports and further inspection by an expert neuroradiologist having the following features: no lesion in one hemisphere and on both sides of the corpus callosum (CC) and cortico-spinal tract (CST), which were used as target structures. T patients were chosen on the basis of the diagnosis of glioblastoma multiforme (GBM) with the purpose of differentiating the tumor ROI with damaged fibers from the surrounding edema ROI, where preserved fibers are hardly detected by the classical DTI analysis.

4.2.3. ODI threshold calibration

The aim of this preliminary stage was to investigate the dependence of the results of NODDIT on the termination criteria based on both an ODI and a f_{ISO} threshold, and to find a way to fairly compare DTT and NODDIT. Therefore we compared NODDIT with different ODI thresholds and DTT in healthy regions of C subjects, selected to have lesions only in one hemisphere and far from the CC and the CST.

For NODDIT, the main direction of the intracellular compartment estimated by the model in each voxel was used, and different ODI upper thresholds were applied: every 0.05 from 0 to 0.25, every 0.01 from 0.25 to 0.7 and every 0.05 from 0.7 to 1. A f_{ISO} upper threshold of

0.8 was also applied to exclude the voxels with high contamination of CSF, where the estimation of ODI and fiber directions is not robust.

As a reference, whole-brain tractography was performed from the direction of the first eigenvector estimated by DTI in each voxel, with an FA lower threshold of 0.20.

All the reconstructions were performed with the Interpolated Streamline algorithm for deterministic tractography in Diffusion Toolkit [Wang 2007], with an angle threshold of 35°.

Using Trackvis [www.trackvis.org], inclusive and exclusive ROIs were drawn in order to extract the CC and the CST, and they were applied to reconstruct these two tracts from the NODDIT obtained with each ODI threshold and from the reference DTT. The number of streamlines passing through each voxel was calculated for the CC, for the CST and for the whole-brain tractographies, considering only the streamlines longer than 2 cm.

As a global index of the similarity between NODDIT and DTT, the correlation between the number of streamlines reconstructed by NODDIT with each ODI threshold and by DTT in each voxel of the healthy WM was calculated; the healthy WM was defined as the set of voxels in the hemisphere contralateral to the lesion with at least 95% probability to belong to WM according to the segmentation algorithm implemented in SPM 8 [Ashburner 2005].

To evaluate the behavior of the two techniques in the reconstruction of specific tracts, the reconstructed CC and CST were compared. Specifically, the overlap between the volumes of the tracts obtained by NODDIT with each ODI threshold and by DTT was quantified by the Dice index [Dice 1945] between the sets of voxels with at least 5 streamlines.

The dependence of each of the 3 calculated indices (correlation, Dice index on the CC and Dice index on the CST) on the ODI threshold was evaluated and an optimal value was chosen, providing the results most similar to those obtained with DTI in the healthy WM.

4.2.4. Comparison between DTT and NODDIT in the tumor areas

The main stage of this study aimed to evaluate the results obtained by NODDIT in pathological areas of patients with brain tumors. On T patients, with GBM tumors and surrounding areas of vasogenic edema, the tractography results obtained in healthy and affected regions by DTT and optimized NODDIT were compared.

Whole-brain tractography was performed with Diffusion Toolkit from DTI directions with FA > 0.2, and from NODDI directions with f_{ISO} < 0.8 and with the optimized ODI threshold. As in the calibration stage, the number of streamlines longer than 2 cm passing through each voxel was considered.

On each patient's b = 0 image, 4 ROIs were drawn: in the lesion core, in the peritumoral edema, in the contralateral white matter and in the ventricles. The streamline density index, which is the mean number of streamlines passing in each included voxel, was evaluated in each ROI.

In order to investigate the dependence of the results in pathological areas on these thresholds, the analysis was repeated with additional FA and ODI thresholds (FA = 0.00, 0.05, 0.10, 0.15, 0.20; ODI = 0.20, 0.30, 0.40, 0.45, 0.46, 0.47, 0.48, 0.49, 0.50, 0.60, 0.70)

4.3. Results

4.3.1. ODI threshold calibration

The correlation between the number of streamlines reconstructed by NODDIT (with increasing ODI thresholds) and by DTT (FA > 0.2) (figure 4.2) increased in all the patients until an ODI value between 0.45 and 0.5, and then decreased slightly. The ODI value corresponding to the maximum correlation, averaged among the 10 patients, was 0.490 ± 0.018.
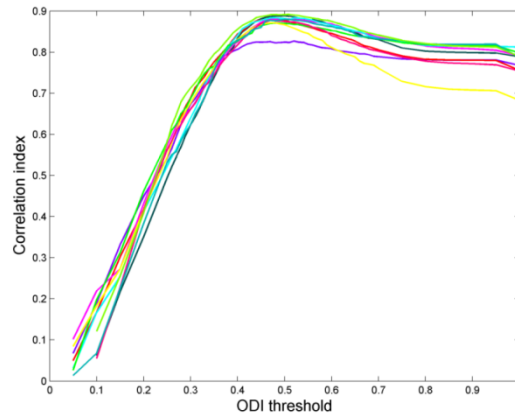
Figure 4.2. Correlation index calculated between NODDIT and DTT streamlines in each voxel of the healthy WM with different ODI thresholds used as termination criteria for NODDIT. The different colors correspond to the different subjects.

A second analysis was focused on the overlap between the volumes occupied by the CC and CST reconstructed by NODDIT and DTT (figure 4.3). In all the subjects the Dice index increased with ODI for values lower than about 0.4 and then remained constant. Thus, every ODI threshold higher than about 0.4 is almost equivalent for the reconstruction of specific tracts by NODDIT.
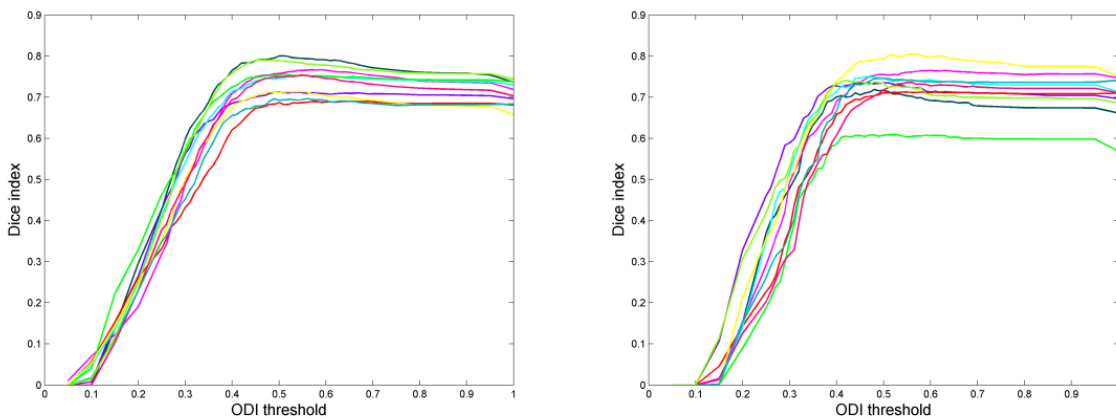
Figure 4.3. Dice index between the volume of the CC (left) and CST (right) reconstructed by DTT and by NODDIT using different ODI thresholds as termination criteria. The different colors correspond to the different subjects.

Figure 4.4 shows some representative examples of the CST reconstructed by DTT and by NODDIT with different ODI thresholds. Note that a significant increase of streamlines is observed passing from ODI < 0.3 to ODI < 0.5, while the reconstructions with ODI < 0.5 and ODI a 0.8 look very similar.
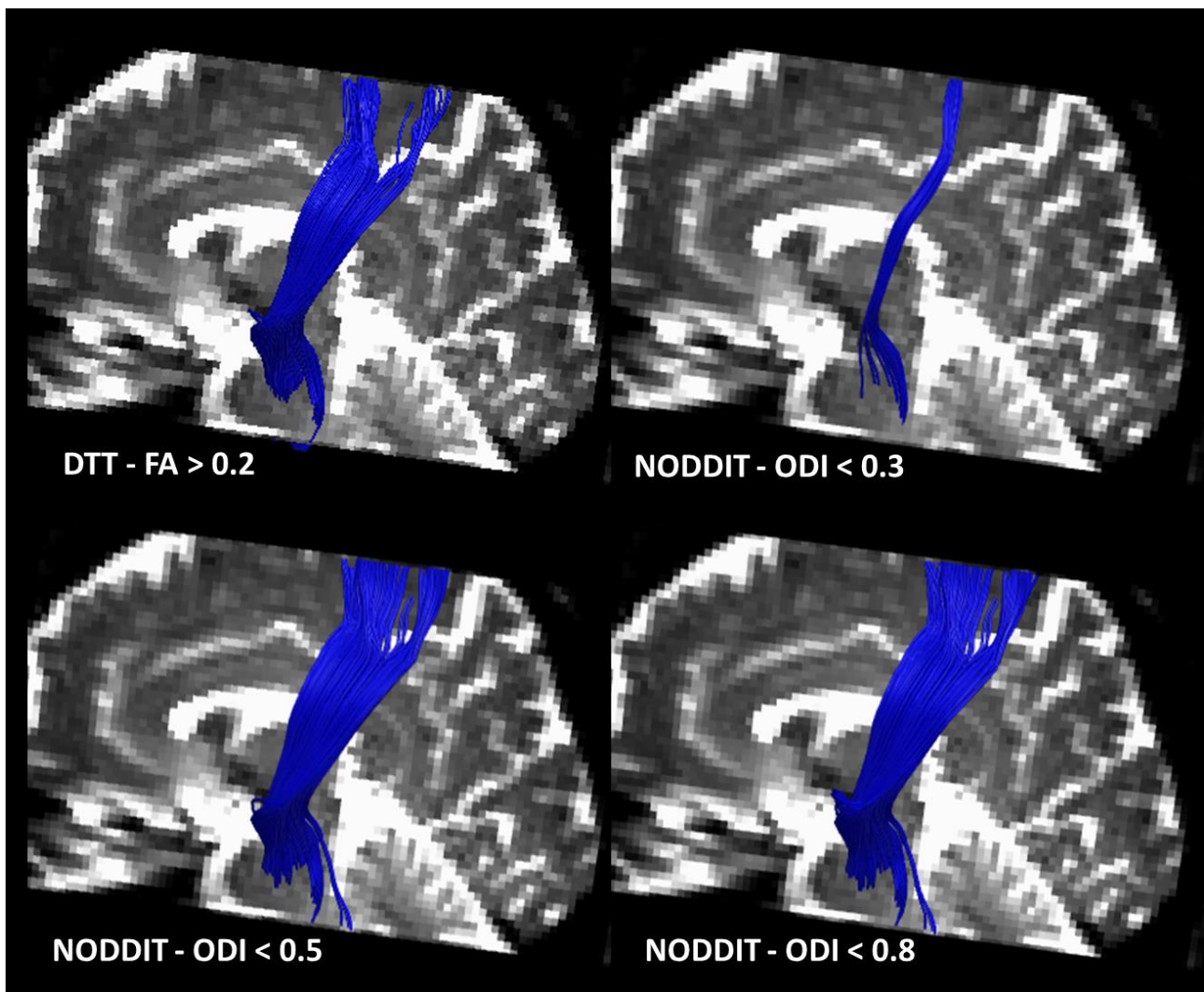
Figure 4.4. Examples of tractographic reconstruction of the CST by DTT and by NODDIT with different ODI thresholds in the same subject.

To better understand the behavior reported in figures 4.2, 4.3 and 4.4, the distribution of FA and ODI values was evaluated in the voxels occupied by the CST reconstructed by DTT and NODDIT, respectively, with no FA or ODI threshold (figure 4.5).While FA shows a relatively broad distribution between 0.2 and 0.8, ODI has a narrower distribution centered on about 0.2
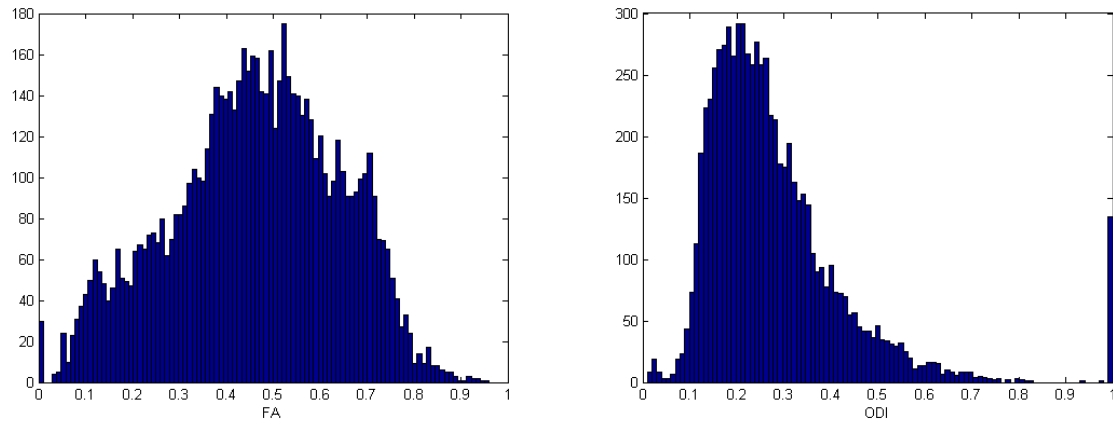
Figure 4.5. Histograms of FA (left) and ODI (right) values in the voxels occupied by the CST reconstructed by DTT and by NODDIT without FA or ODI thresholds, respectively.

Based on these results, an optimal ODI of 0.49 was chosen for the following comparisons. To further validate the agreement between DTT and NODDIT with this ODI threshold in the healthy tissue, we examined the scatter plot and the Bland-Altman plot (showing the mean of two measures on the horizontal axis and their difference on the vertical axis) for the number of streamlines found by DTT and NODDIT in all the voxels of the healthy WM of all the C subjects (figure 4.7).
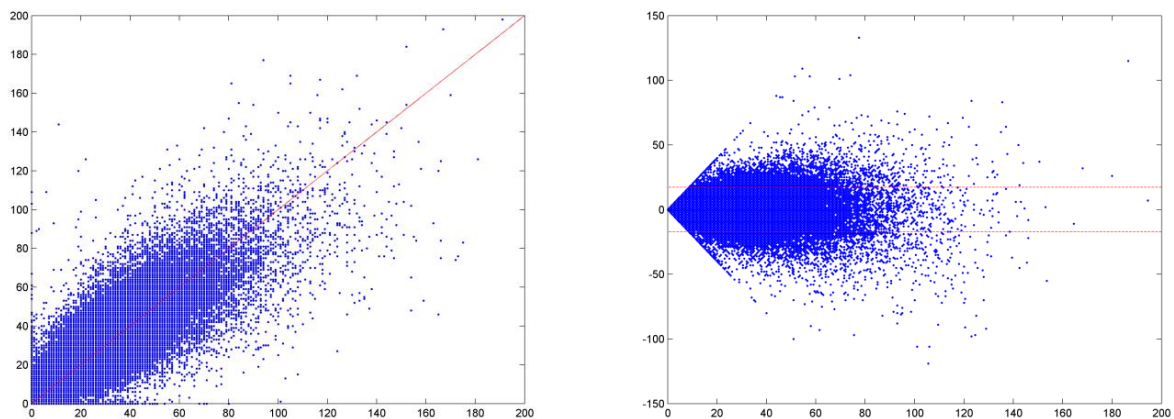
Figure 4.6. Scatter plot (left) and Bland-Altman plot (right) of the streamline density found in each voxel by DTT with FA > 0.2 and by NODDIT with ODI < 0.49. In the scatter plot, the red line is the identity line. In the Bland-Altman plot the mean between NODDIT and DTT streamline density is reported on the x axis, while the difference between NODDIT and DTT streamline density is on the y axis, The red dashed lines are ±1.96 times the standard deviation of the difference (95% confidence interval)

In the scatter plot the values are centered on the identity line and have a relatively low dispersion. In the Bland-Altman plot the differences are centered on 0 for all the mean values and have a relatively low dispersion. Thus it can be concluded that with the estimated optimal ODI threshold the number of streamlines estimated by NODDIT and DTT are in good agreement: the two techniques provide similar values, with no evident bias.

4.3.2. Comparison between DTT and NODDIT in the tumor areas

The mean streamline densities provided by NODDIT (with the optimized ODI threshold) and by DTT in the healthy WM, tumor core and vasogenic edema, averaged among the 10 T subjects, are shown in figure 4.7 as bar graphs.
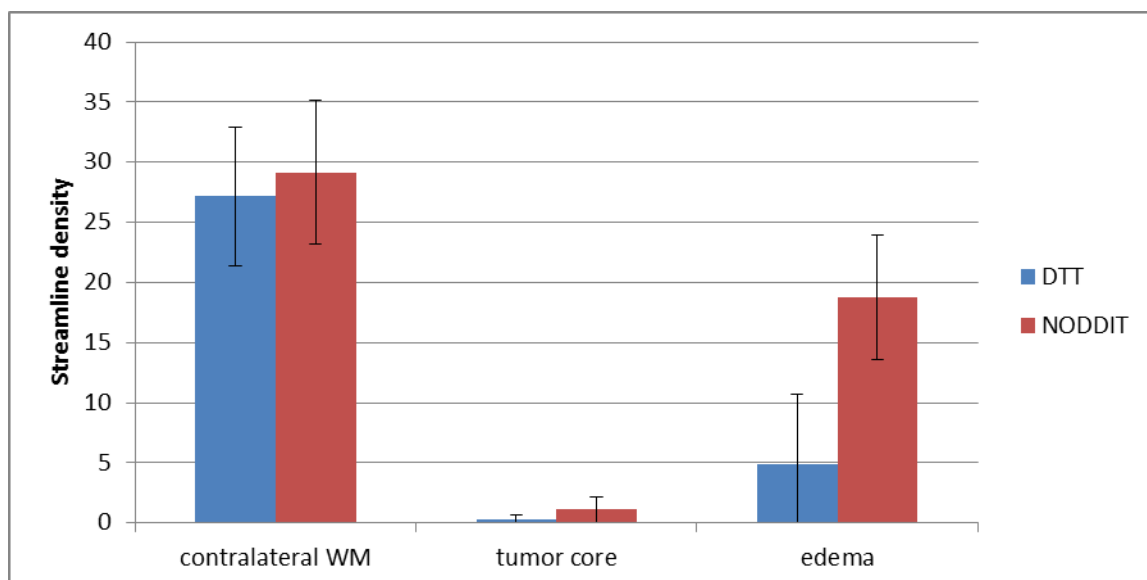
Figure 4.7. Mean streamline density found by DTT and NODDIT in contralateral healthy WM, tumor core and vasogenic edema.

In the contralateral WM both techniques provide high streamline densities (between 25 and 30 streamlines per voxel on average) with no important difference between DTT and NODDIT. In the tumor core both tractography methods provide very low streamline densities, as expected since no residual tracts are assumed to be present in the tumor core of GBM.

On the contrary, in vasogenic edema the mean streamline density estimated by NODDIT is significantly higher than that estimated by DTT. For both techniques the results in vasogenic edema are intermediate between those in the tumor core and those in healthy WM, but NODDIT streamline densities are about 67% than in healthy WM on average, while DTT streamline densities are only about 19% than in healthy WM on average.

The same results are shown in figure 4.8 as a Bland-Altman plot. In both the normal appearing WM and the tumor core the difference between NODDIT and DTT streamline density is very low, while in vasogenic edemas the differences are much higher (note that a positive difference means that NODDIT streamline density is higher than DTT streamline density).
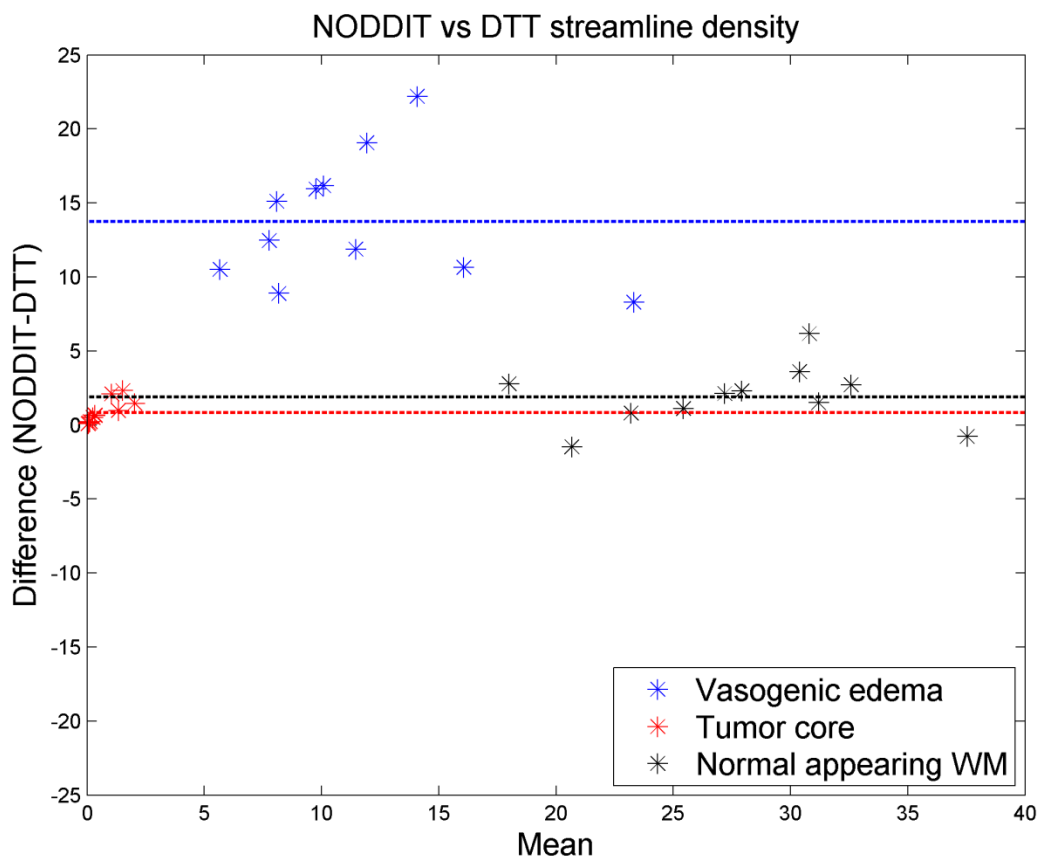
Figure 4.8. Bland-Altman plot for the streamline density found by DTT and NODDIT in areas of vasogenic edema, tumor core and contralateral WM in each patient. The dashed lines represent the mean difference between NODDIT and DTT streamline density in each region

Some additional remarks can be made examining the individual streamline densities obtained for each patient (table 4.1).

As already observed, in the healthy WM, the streamline densities from DTT and optimized NODDIT were always comparable and high (between 16 and 36 streamlines per voxel). In the tumor cores, very low values of streamline density were obtained from DTT (less than 0.02 streamlines per voxel in 7 cases out of 10, with a maximum of 1.3 streamlines per voxel in the remaining ones). Considering NODDIT, higher densities were obtained in all the cases, however they were lower than 1 streamline per voxel in 6 cases out of 10, and lower than 3 streamlines per voxel in the remaining ones.

In the edemas, DTT streamline density was lower than 6 streamlines per voxel in 8 cases out of 10, while NODDIT streamline density was higher than 10 streamlines per voxel in all the cases (table 1). Only in two cases the number of streamlines reconstructed by DTT was almost comparable to that reconstructed by NODDIT. Moreover, these were the only cases in which DTI-based streamline density in the edema was of the same order of magnitude than in the contralateral WM. By contrast, with NODDI the streamline density in the edema was always of the same order of magnitude than in the contralateral normal appearing WM, even though slightly lower.

Table 4.1. Streamline density obtained with DTT (FA > 0.20) and NODDIT (ODI < 0.49) in the different ROIs for each patient.

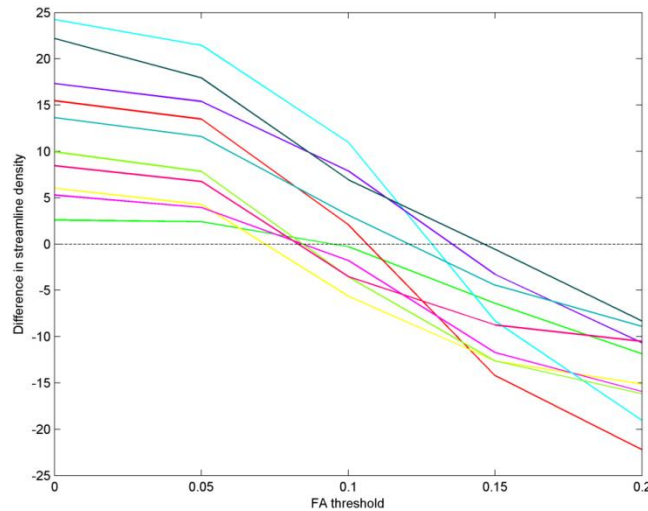| Patient code	Streamline density					
	contralateral WM		tumor core		edema	
	DTI	NODDI	DTI	NODDI	DTI	NODDI
01	26.13	28.25	0.01	0.23	5.52	17.39
02	30.45	31.95	0.00	0.15	2.98	25.18
03	16.60	19.39	0.00	0.09	0.53	15.65
04	21.42	19.93	0.01	0.15	1.79	17.73
05	37.92	37.14	0.02	0.67	2.40	21.46
06	26.77	29.07	0.85	1.82	10.74	21.39
07	24.87	25.98	1.30	2.76	19.16	27.46
08	28.58	32.19	0.36	2.68	1.99	18.16
09	27.71	33.88	0.00	2.09	3.74	12.63
10	31.22	33.94	0.00	0.50	0.41	10.92

The analysis in the edema was repeated using different ODI thresholds for NODDIT. The difference between NODDIT and DTT streamline density at each ODI threshold is shown in figure 4.9. From these experiments it arises that NODDIT streamline density in the edemas is higher than DTT for all the thresholds above 0.30 in 8 patients out of 10, and for all the thresholds above 0.40 in the other two patients. Thus the enhanced sensitivity of NODDIT in reconstructing streamlines in the edema is robust against the error caused by a possible overestimation of the optimal ODI threshold.
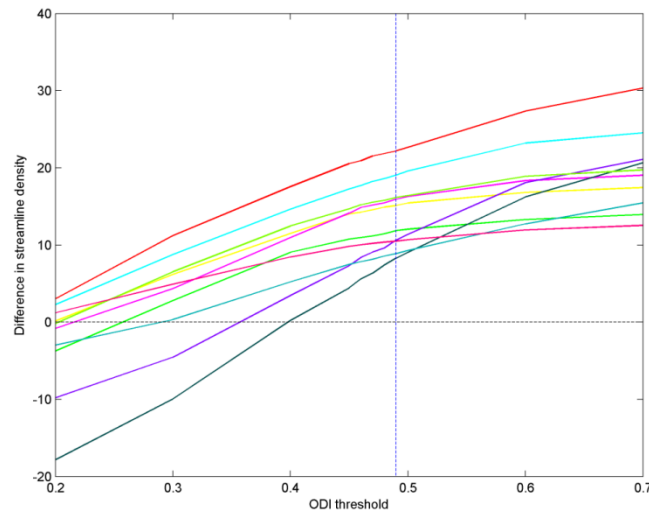
Figure 4.9. Difference between the streamline density obtained by NODDIT with different ODI thresholds and that obtained by DTT in the edema. The different colors correspond to different patients. The horizontal black dashed line represents null difference, while the vertical blue dashed line corresponds to the optimal ODI threshold used in this study.

Repeating the same analysis with different FA thresholds, the streamline density in the edemas increased at lower thresholds, reaching values similar to those obtained by optimized NODDI at a threshold of about FA = 0.10 (figure 4.10).

Figure 4.10. Difference between the streamline density obtained by DTT with different FA thresholds and that obtained by NODDIT in the edema. The different colors correspond to different patients. The horizontal black dashed line represents null difference.

To evaluate the significance of the previous finding, the streamline density comparison was focused on the ventricles, where no fibers at all should be reconstructed.

NODDIT streamline density in the ventricles was virtually null: lower than 0.05 streamlines per voxel in all the patients, with a mean value of 0.02 streamline per voxel.

DTT streamline density was higher than NODDIT in 9 out of 10 patients at FA = 0.20 (mean density 0.32 streamlines per voxel), and increased with lower FA thresholds, reaching an average value of about 1.6 streamlines per voxel at FA = 0.10 and more than 8 streamlines per voxel at FA = 0 (figure 4.11). It has to be remarked that a length threshold was set to reckon only the tracts longer than 2 cm in the evaluation of the streamline density; without this filter, the number of streamlines found by DTT in the CSF would have been even much higher with low FA thresholds.

So DTT can achieve similar results as NODDIT in the edemas by reducing the FA threshold, but it produces a larger amount of false positives in regions with high CSF content.
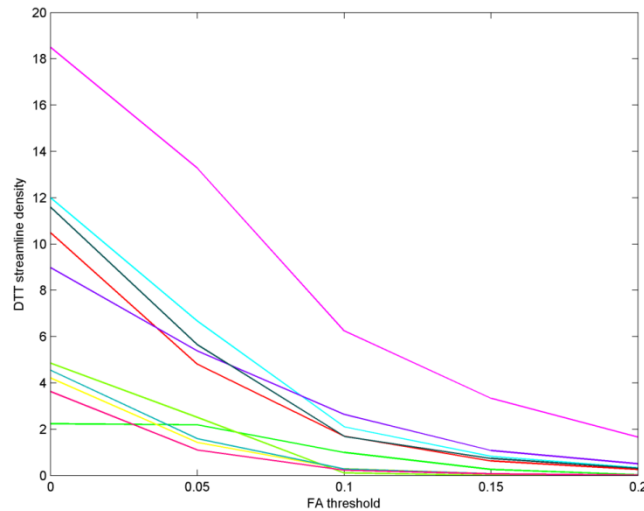
Figure 4.11. Difference between the streamline density obtained by DTT with different FA thresholds and that obtained by NODDIT in the edema. The different colors correspond to different patients. The horizontal black dashed line represents null difference.

Figure 4.12 shows two examples of the reconstruction of specific tracts passing through edematous areas. In particular, inclusive and exclusive ROIs were manually delineated to segment the IFOF and CST in T patients number 02 and 03 respectively. The same ROIs were applied both to DTT and NODDIT.

In the first case (T patient number 02) the IFOF was reconstructed by both the techniques, but NODDIT (figure 4.12, A) showed a higher streamline density than DTT (figure 4.12, B) on the side of the edema. Note the area of low FA (streamlines colored in yellow) in the edematous region around the lesion.

In the second case (T patient number 03), DTT reconstructed the CST only on the healthy side (figure 4.12, C). NODDIT provided streamlines on both sides, with a realistic trajectory of the tract on the affected side (figure 4.12, D).

Also in this case, the streamlines reconstructed by NODDIT in the edema have low FA values, which probably prevents the reconstruction by DTT.
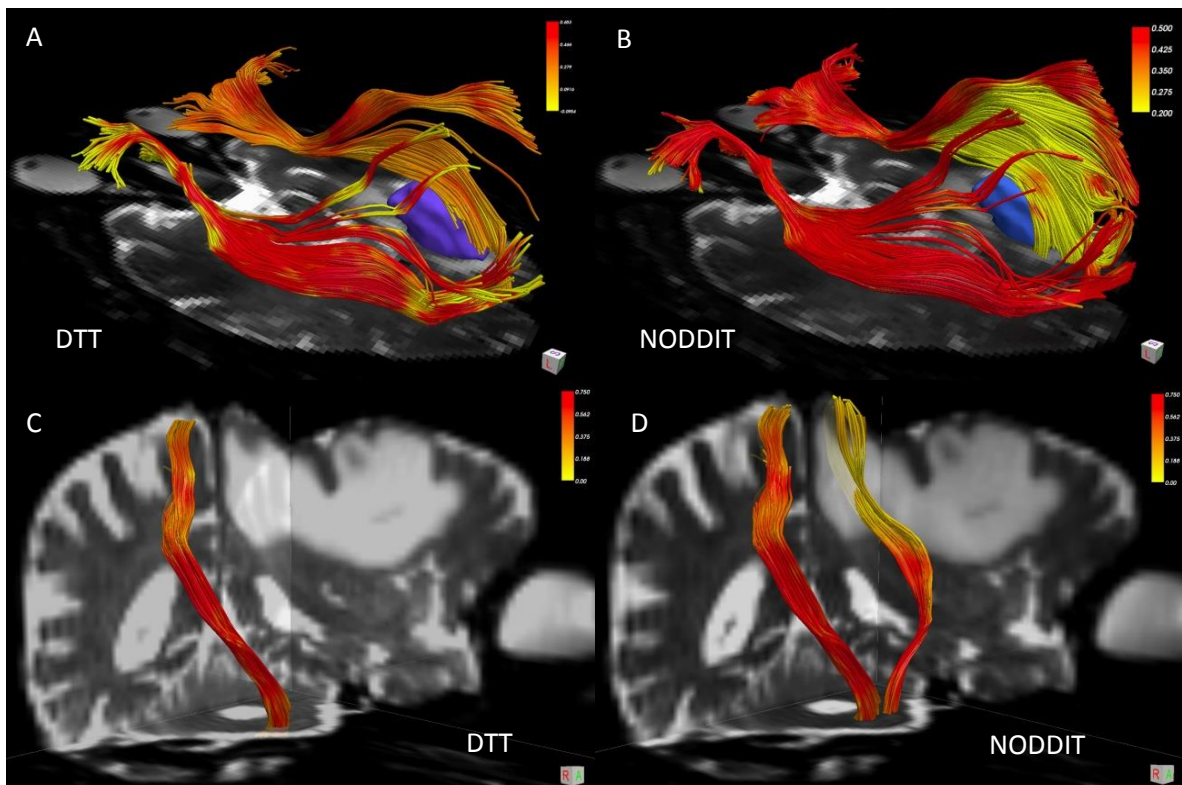
Figure 4.12. Examples of tractographic reconstruction in two representative GBM patients.
First row: the IFOF was reconstructed from the same ROIs with DTT (A) and NODDIT (B). A manual segmentation of the tumor mass is represented in blue. Note the higher streamline density in the edema from NODDIT with respect to DTT.
Second row: the CST was reconstructed from the same ROIs with DTT (C) and NODDIT (D). DTT did not allow the reconstruction of any streamline on the side of the edema, while NODDIT provided a realistic reconstruction of the CST.
In all the panels the streamlines are color-encoded according to FA.

4.4. Discussion

In this work a procedure to perform tractography based on NODDI parameters was developed and applied it in the analysis of brain tumor patients to investigate its potential benefits in areas of vasogenic edema, where standard DTT is usually not able to reliably reconstruct WM tracts.

The first result of this study is the optimization of an ODI threshold to have NODDIT reconstructions highly overlapping DTT ones at FA > 0.2 in healthy brain areas. The optimal ODI threshold was chosen considering two aspects: the voxel by voxel correlation

of the number of streamlines reconstructed by the two techniques, and the correspondence between the volumes of the reconstructed CC and CST, evaluated by the Dice index.

Interestingly, the correlation showed only a slight decrease for thresholds higher than the optimal one, and the Dice index showed a plateau for high ODI thresholds. This suggests the robustness of the NODDIT approach, because the dependence of the results on the threshold is low. This result was verified by visual inspection of the tracts reconstructed with different thresholds and by evaluating the distribution of FA and ODI values inside the tracts. The former demonstrated a gradual increase of the number of streamlines for increasing ODI thresholds until about 0.5 and only few changes above this value. The latter showed a narrower distribution of ODI with respect to FA, centered on a value of about ODI = 0.2; thus, it is quite obvious that increasing the ODI threshold beyond a certain limit has little effect on tractography.

It has to be noted that NODDIT involves an additional threshold on f_{ISO}, which has likely a role for this robust behavior at high thresholds. When f_{ISO} is high, the estimation of the orientation distribution is unreliable, so it is probable that some potential additional streamlines with high ODI are excluded from the reconstruction because they are also associated with high f_{ISO} values.

In the main part of this work NODDIT performance was investigated in brain tumor patients. The main result is a significantly higher streamline density in the areas of edema achieved by NODDIT (using the calibrated ODI threshold) with respect to DTT. This result is specific to edemas, since in this group of patients we verified that the two methods provide similar streamline densities in the healthy WM structures contralateral to the tumors. Moreover, the values of streamline density found in the edemas by NODDIT are almost comparable to those found in healthy WM, while for DTT they are much lower. The difference between the performance of NODDIT and DTT is very unlikely due to an error in the calibration step,

as could be expected by the robustness of NODDI described above; indeed, we investigated the dependence of the estimated streamline densities in the edemas on the ODI threshold and found that it is much smaller than the difference between NODDIT and DTT for a reasonable calibration error.

In the core of GBM tumors, where little structure is expected, both DTT and NODDIT found low streamline densities as expected. However, it should be noted that the densities found by NODDIT, though low, are higher than those found by DTT in all cases. Since no histological ground truth was available, it is not clear at this stage whether the additional streamlines consistently reconstructed by NODDI in the tumor cores are false positives or real structures (fibers or other sources of diffusion anisotropy) better detected by NODDIT than by DTT.

To address the specificity of the proposed method, ROIs were placed in the ventricles, where no fibers should be reconstructed at all. Virtually no streamlines were detected here by NODDIT. It is worth to remark that this basic specificity feature required a threshold of f_{ISO} < 0.8, while a pure ODI threshold didn't provide an acceptable performance (data not shown). On the contrary, DTT showed a non-negligible number of false positives in the CSF, especially with the lower FA thresholds necessary to achieve results similar to NODDIT in the edema.

In summary, NODDIT showed noteworthy accuracy: the appropriate settings of threshold on the two main NODDI parameters provided both high sensitivity in problematic areas as edema and good specificity in areas were few or no fibers were to be expected. The multicompartmental nature of NODDI is probably the key factor for the advantage of NODDIT over DTT: it allows a greater flexibility in the choice of exclusion and termination criteria.

The visual assessment of the reconstruction of specific tracts confirmed the quantitative results and verified that the streamlines found in areas of edema are compatible with

known neuroanatomy. In some cases NODDIT allowed the reconstruction of tracts completely missed by DTT, while in other cases the tracts of interest were identified by both techniques but NODDIT provided a higher number of streamlines.

The proposed technique could have important applications, especially in presurgical mapping. It may provide more reliable tractographic reconstructions in the areas of vasogenic edema that would convey crucial information for planning neurosurgery operations. The simple acquisition protocol and relatively short acquisition time make this method feasible in a clinical setting; the only issue is the long processing time needed for the estimation of NODDI parameters (about 10 hours for a typical dataset and a typical PC).

The main limitation of this study is the lack of a ground truth for the validation of the reconstructed tracts: we can not be completely sure that the streamlines reconstructed by the two methods correspond to real fibers, even though DTT has been validated in many cases [Leclercq 2010, Hansen 2011, Seehaus 2012] and the similarity between the main tracts obtained in healthy regions with NODDIT and DTT seems encouraging for the validity of NODDIT results also in pathological areas. So a major area of future work is the validation of the results of NODDIT with techniques as intraoperative electrical stimulation or with the detection of WM fibers in bioptic samples.

Moreover, NODDI is a single fiber model and thus is not advantageous over DTI in areas of fiber crossing. In further work, a modified version of NODDI including multiple intracellular compartments could be applied for tractography, even though this would further increase the post-processing time and would probably require a more complex acquisition protocol. Advanced dMRI methods aiming at an accurate estimate of the ODF (see paragraph 1.4), such as Spherical Deconvolution, can definitely solve the fiber crossing problem, but their performance in edematous areas has to be investigated; this is

an interesting topic for future studies, but was not considered in this work of thesis because it is focused on multi-compartment models.

Another possible extension of this work is the application of NODDIT to other brain lesions addressed by neurosurgery. In particular, low-grade gliomas may infiltrate WM bundles without disrupting them, and it would be very important to assess if the infiltrated fibers are still intact; this is not possible with DTI, but a multicompartmental model as NODDI may help to distinguish between the tumor and the infiltrated bundle.

Finally, in this work a standard tractographic algorithm was used and the principal direction estimated by NODDI was taken as the only possible fiber direction, considering the ODI only as a termination criterion and not accounting for the dispersion of orientations in the reconstruction of the pathways. Thus, a possible area of future work is the use of more sophisticated algorithms for tractography, possibly with a full exploitation of the information provided by NODDI about orientation dispersion.

In conclusion, this work proposed a feasible method for tractography based on the NODDI model and applied it for the study of patients with GBM. It showed that NODDIT allows tractography through areas of vasogenic edema in a much more reliable way than DTT, with great potential advantages in the field of presurgical mapping.

Bibliography

Ashburner J, Friston KJ. Unified segmentation. *Neuroimage*. 2005;26(3):839-851.

Basser PJ, Pajevic S, Pierpaoli C, Duda J, Aldroubi A. In vivo fiber tractography using DT-MRI data. *Magn Reson Med*. 2000;44(4):625-632.

Bello L, Gambini A, Castellano A, et al. Motor and language DTI Fiber Tracking combined with intraoperative subcortical mapping for surgical removal of gliomas. *Neuroimage*. 2008;39(1):369-382.

Berman JI, Berger MS, Mukherjee P, Henry RG. Diffusion-tensor imaging-guided tracking of fibers of the pyramidal tract combined with intraoperative cortical stimulation mapping in patients with gliomas. *J Neurosurg*. 2004;101(1):66-72.

Bizzi A. Presurgical mapping of verbal language in brain tumors with functional MR imaging and MR tractography. *Neuroimaging Clin N Am*. 2009;19(4):573-596.

Black PM, Ronner SF. Cortical mapping for defining the limits of tumor resection. *Neurosurgery*. 1987;20(6):914-919.

Dice LR. Measures of the amount of ecologic association between species. *Ecology*. 1945;26(3):297-302.

Dimou S, Battisti RA, Hermens DF, Lagopoulos J. A systematic review of functional magnetic resonance imaging and diffusion tensor imaging modalities used in presurgical planning of brain tumour resection. *Neurosurg Rev*. 2013;36(2):205-214.

Figini M, Baselli G, Riva M, Bello L, Zhang H, Bizzi A. NODDI performs better than DTI in brain tumors with vasogenic edema. In: *Proc Intl Soc Mag Reson Med*.; 2014:0271.

Figini M, Baselli G, Riva M, Bello L, Zhang H, Bizzi A. NODDI improves tractography in vasogenic edema of brain tumors. *(in preparation)*

Hansen B, Flint JJ, Heon-Lee C, et al. Diffusion tensor microscopy in human nervous tissue with quantitative correlation based on direct histological comparison. *Neuroimage*. 2011;57(4):1458-1465.

Jones DK. Challenges and limitations of quantifying brain connectivity in vivo with diffusion MRI. *Imaging Med*. 2010;2(3):341-355.

Kuroiwa T, Ueki M, Chen Q, Ichinose S, Okeda R. Is the Swelling in Brain Edema Isotropic or Anisotropic? In: Ito U, Baethmann A, Hossmann K-A, et al., eds. *Acta Neurochir Suppl (Wien)*.Vol 60. Acta Neurochirurgica. Springer Vienna; 1994:155-157.

Leclercq D, Duffau H, Delmaire C, et al. Comparison of diffusion tensor imaging tractography of language tracts and intraoperative subcortical stimulations. *J Neurosurg*. 2010;112(3):503-511.

Lu S, Ahn D, Johnson G, Cha S. Peritumoral Diffusion Tensor Imaging of High-Grade Gliomas and Metastatic Brain Tumors. *Am J Neuroradiol*. 2003;24:937-941.

Mori S, Crain BJ, Chacko VP, van Zijl PCM. Three-dimensional tracking of axonal projections in the brain by magnetic resonance imaging. *Ann Neurol*. 1999;45:265-269.

Ng WH, Mukhida K, Rutka JT. Image guidance and neuromonitoring in neurosurgery. *Childs Nerv Syst*. 2010;26(4):491-502.

Provenzale JM, Mcgraw P, Mhatre P, Guo AC, Delong D. Radiology Peritumoral Brain Regions in Gliomas and Meningiomas : Investigation with Isotropic Imaging and Diffusion-Tensor MR Imaging. *Radiology*. 2004;232(2):451-460.

Schiffbauer H, Ferrari P, Rowley HA, et al. Functional activity within brain tumors: A magnetic source imaging study. *Neurosurgery*. 2001;49(6):1313-1321.

Schonberg T, Pianka P, Hendler T, Pasternak O, Assaf Y. Characterization of displaced white matter by brain tumors using combined DTI and fMRI. *Neuroimage*. 2006;30(4):1100-1111.

Seehaus AK, Roebroeck A, Chiry O, et al. Histological validation of DW-MRI tractography in human postmortem tissue. *Cereb Cortex*. 2013;23(2):442-450.

Wang R, Benner T, Sorensen AG, J W V. Diffusion Toolkit : A Software Package for Diffusion Imaging Data Processing and Tractography. In: *Proc Intl Soc Mag Reson Med*; 2007:3720.

Wolbers JG. Novel strategies in glioblastoma surgery aim at safe, supra-maximum resection in conjunction with local therapies. *Chin J Cancer*. 2014;33(1):8-15.

Yamada K, Nakamura H, Yuen S, Kubota T, Tanaka O, Akada W. Brain Fiber Tracking with Clinically Feasible Imaging : Initial Experience. *Radiology*. 2003;227(1):295-301.

Zhang H, Schneider T, Wheeler-Kingshott CAM, Alexander DC. NODDI: practical in vivo neurite orientation dispersion and density imaging of the human brain. *Neuroimage*. 2012;61(4):1000-1016.

5. CONCLUSIONS

*Science never solves a problem
without creating ten more.*
George Bernard Shaw

Diffusion MRI (dMRI) is a powerful technique, employing water molecules as endogenous probes to study the microstructure of biological tissues.

DTI is the most widely used dMRI approach, since with a simple acquisition and processing protocol, it provides information about the average extent and directionality of the diffusive motions of water molecules, which are indirect indices of the presence of structures and of their orientations in the studied tissue. The popularity of DTI is also due to its sensitivity to pathological changes of tissue microstructure in many diseases. However, it is based on rather simplistic assumptions about water diffusion, which are not satisfied in many cases, and the estimated parameters are affected by many factors, making DTI results not very specific to complex physiological (e.g. fiber crossing) and pathological conditions.

Many advanced dMRI methods have been developed in recent years to overcome DTI limitations. In particular, methods based on mathematical models of combined free, hindered and/or restricted diffusion in environments with known geometry have gained interest because they can provide more specific information about microstructural features of tissues.

The aim of this work of thesis was to evaluate the feasibility and usefulness of model-based dMRI techniques in clinical studies on neurological diseases.

In particular, two neuropathies were studied: Creutzfeldt-Jakob Disease (CJD), investigated with specific models derived from neuropathological hypotheses on tissue alterations (chapter 2), and brain tumors, investigated with the Neurite Orientation Dispersion and Density Imaging (NODDI). The latter study had two aims: to differentiate and characterize different kinds of brain glioma (chapter 3) and to test the possibility to improve tractography in regions with vasogenic edema (chapter 4).

5.1. Model-based analysis of dMRI signal in CJD patients

In the study on CJD, dMRI data acquired with a wide range of T_2 and diffusion weightings and diffusion times were thoroughly examined with mathematical models based on two different hypotheses on the neuropathological origin of the typical dMRI hyperintensity detected in CJD patients: extracellular PrP^{Sc} deposition and spongiform degeneration with the formation of vacuoles restricting water molecules. By comparing the raw MRI data of patients and healthy subjects the dependence of the observed signal hyperintensity on the acquisition parameters was investigated and optimal MRI parameters that may further highlight such hyperintensities in future clinical studies were suggested. This study showed that a biexponential or a spherical restricted-diffusion model can fit the data better than the generally used mono-exponential model. According to the results of this work, in the affected ROIs the main contributions to dMRI signal hyperintensity come from an increase of T_2 and some form of reduction of the diffusive motions, which is explained as a reduction of diffusivities by the mono- and biexponential models and as an increase of the restricted compartment in the spherical restricted-diffusion model. Since the two bi-compartment models performed similarly, it was not possible to conclude whether prion PrP^{Sc} deposition or spongiform degeneration is a more likely cause of dMRI hyperintensities. Either both pathological changes do contribute to the signal abnormality,

or the degree of complexity of microstructural pathology is higher than anticipated by the two models investigated in this study. Future studies will have to test more sophisticated models, for example accounting for vacuole permeability. For the first time this study showed that it is feasible to estimate average vacuolar size with MRI. This work can represent an important step forward to a better characterization of MRI abnormalities in prionopathies and to foster the development of more sensitive sequences for early diagnosis and characterization of sCJD.

5.2. Microstructural features of brain tumors by NODDI

In the study on the microstructural characterization of brain gliomas with NODDI, dMRI data were acquired with a two-shell (i.e., low and high b-value) acquisition protocol from a population of patients with neuropathological diagnosis of brain glioma. The data were analyzed with NODDI, DTI and, for a subset of patients, with a multi-compartment isotropic diffusion model designed to understand NODDI performance in the case of isotropic restricted diffusion.

The comparison between NODDI and the isotropic model showed that NODDI can be useful also in regions with isotropic diffusion restriction, even though the values of the estimated volume fractions have to be considered carefully in this case.

The subsequent ROI-based analysis in the full population of patients pointed out the possibility to characterize the different tumor types and the different components of each lesion with NODDI parameters. In particular, in grade II gliomas regions with high extracellular water content were usually identified, while in grade III gliomas additional regions with high cellularity were detected and in grade IV gliomas regions with several different features were generally found: necrotic areas, areas of enhancement with increased extracellular and free water, highly cellular areas and peritumoral edemas.

On the contrary, DTI parameters were not very useful for the characterization of the different types of lesions: similar high MD and low FA values were found in most of the lesions, with the only exception of the areas with highest cellularity.

When compared between groups of patients with different tumor grades, NODDI volume fractions allowed differentiating grade IV from grade II and grade III gliomas.

If these preliminary results will be validated with a more in-depth correlation with neuropathological measures, NODDI could establish itself as a valuable tool for non-invasive tumor grading and characterization. This would have an important impact on the presurgical evaluation of brain tumor patients, which is fundamental to define the strategy for chemotherapy, radiotherapy and/or surgery

5.3. NODDI-based tractography in peritumoral edema

In the study on tractography in brain tumor patients, an algorithm was developed to perform tractography using NODDI parameters. NODDI-based tractography (NODDIT) has one main advantage on DTI-based tractography (DTT): it can set termination criteria based on more than one parameter to detect the presence of brain tissue (f_{ISO} threshold) and to stop the reconstruction when the tract direction is unreliable (ODI threshold), while in DTT both these conditions are tested upon the sole FA threshold.

In a preliminary step, the ODI threshold used as a termination criterion for NODDIT was calibrated in order to have results as similar as possible to DTT in the healthy brain tissue.

Then the optimized NODDIT algorithm was applied in patients with GBM lesions surrounded by areas of vasogenic edema.

The main result of this study is a higher streamline density estimated by NODDIT with respect to DTT in the areas of edema in all the considered cases; conversely, in the contralateral normal appearing WM and in the tumor core the two techniques showed

similar results. The visual inspection of the reconstructed tracts confirmed the quantitative results: NODDIT could reconstruct plausible streamlines through areas of edemas, where DTT found less streamlines or even failed to reconstruct tracts at all.

These preliminary results are very encouraging. NODDIT could be used to obtain more reliable tractography reconstructions than possible with DTT in brain regions with partial volume from pathological tissue, such as in the case of peritumoral edema.

NODDIT could hence find important applications in neuro-oncology and especially in presurgical mapping, to understand if structurally preserved WM tracts pass through the edematous regions and what is their spatial relationship with the tumor.

5.4. Final considerations

In this work of thesis, model-based dMRI methods have been applied in different applications to study the microstructural alterations caused by neuropathies involving GM and WM.

In all the proposed applications, the use of multi-compartment models was advantageous over traditional methods and provided more specific parameters of the underlying tissue microstructure or of the microstructural changes induced by pathology.

The translational approach followed by the present work was to choose or develop suitable models for specific applications, fit it to the data, thus bringing advanced methodologies and protocols to end applications. In general, this aim represents a challenge as to the validation and interpretation of methods and results, since the necessary compromise between model complexity and connection to the biological ground-truth, and the often incomplete knowledge of the latter, render this process neither straightforward nor trivial. Furthermore, the hardware features available on clinical scanners (especially the maximum gradient amplitude) may limit the accuracy and precision of parameters

estimation, thus challenging their interpretation. However, if this limitation is taken into account and the results are considered to obtain a contrast between different conditions rather than precise numeric values of microstructural features, this issue does not impair the clinical application of multi-compartment dMRI methods.

This procedure is definitely more demanding than that required for a traditional DTI analysis, but it is presently the only available way to obtain as unambiguous microstructural information as possible on the examined biological tissues.

ACKNOWLEDGMENTS

I am sincerely grateful to all the people who supported me during these years and who contributed to this work of thesis, directly or (perhaps most important) indirectly.

First of all I have to thank my supervisor, Prof. Baselli, for giving me the opportunity of this PhD course, for his continuous support, his patience and his helpful suggestions.

I thank Dr. Bizzi for allowing me to work in a great and very interesting project, for his medical competence and experience and for putting me into contact with the most important diffusion MRI groups in the world.

I'm really thankful to Prof. Danny Alexander, Dr. Gary Zhang and all the Microstructure Imaging Group at UCL: Uran, Maira, Andrada, Tingting, Matt, Laura, Gemma, Torben, Simon, Alessandro, Mark, Bernard, Ivana (in random order, and sorry if I forgot someone). They showed me what real science is. My stay in London was a fantastic opportunity to work in a stimulating environment, where everyone knows what to do and why, where the group leaders are always available and happy to discuss. And it was an opportunity to visit a fantastic city.

Ringrazio la grande famiglia del Besta, primi fra tutti i miei "fratelli" Alfonso e Ando. Grazie ad Alfonso per l'amicizia, l'attenzione e la disponibilità, e per avermi sempre ascoltato: è una delle persone che conoscono meglio il contenuto di questa tesi, suo malgrado. Grazie ad Ando per la sensibilità e la profondità che dimostra quando si ricorda del mondo, per il coraggio, l'allegria e l'imprevedibilità. Grazie ad entrambi per aver condiviso giornate fatte di discussioni più o meno impegnate, cibo e anche un po' di lavoro. E grazie a Mari e Sally che hanno dato loro una ragione per sopportare tutto questo.